Fall 2013

Micro solar thermal energy development and use for MEMS power applications

Emmanuel Ogbonnaya
Louisiana Tech University

MICRO SOLAR THERMAL ENERGY DEVELOPMENT AND USE FOR MEMS POWER APPLICATIONS

by

Emmanuel Ogbonnaya, B.Eng., M.S.

A Dissertation Presented in Partial Fulfillment
of the Requirements for the Degree of
Doctor of Philosophy

COLLEGE OF ENGINEERING AND SCIENCE
LOUISIANA TECH UNIVERSITY

November 2013

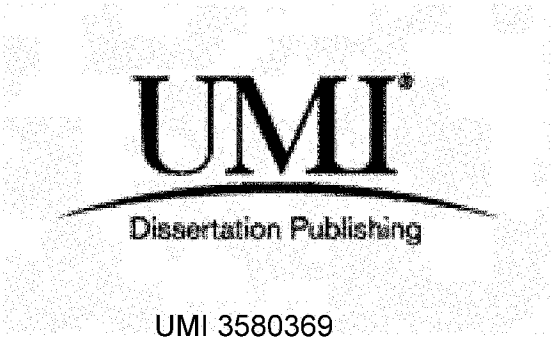

ProQuest LLC
789 East Eisenhower Parkway
P.O. Box 1346
Ann Arbor, MI 48106-1346

LOUISIANA TECH UNIVERSITY

THE GRADUATE SCHOOL

August 5, 2013

Date

We hereby recommend that the dissertation prepared under our supervision by Emmanuel Ogbonnaya, B.Eng., M.S.

entitled

Micro Solar Thermal Energy Development And Use For MEMS Power Applications

be accepted in partial fulfillment of the requirements for the Degree of Doctor of Philosophy in Engineering

Supervisor of Dissertation Research

Head of Department

Micro/Nanoscale Systems Engineering

Department

Recommendation concurred in:

Advisory Committee

Approved:

Director of Graduate Studies

Approved:

Dean of the Graduate School

Dean of the College

GS Form 13a
(6/07)

ABSTRACT

Increasing focus on alternative energy sources has produced significant progress across a wide variety of research areas. One particular area of interest has been solar energy. The sun represents sustainable and renewable energy source capable of meeting present energy needs without compromising the ability of future generations to meet theirs. Energy from the sun can be utilized in multiple ways. Direct use in modern power generation typically involves either photovoltaic systems or large-scale solar thermal energy installations. While large-scale solar thermal energy generation is well advanced, there has been comparatively little research on smaller scale thermal energy collection and application. This work presents investigations into micro solar thermal energy development and use for MEMS-based power applications. This approach is divergent from traditional micro solar photovoltaic devices, relying on transforming incoming solar energy to heat for use by devices like thermoelectric generators (TEG) and other heat engines. The ability to maximize temperature gain from the sun's heat energy while minimizing heat losses is critical for a system that relies on solar energy for useful mechanical or electrical work output. The use of a nanometer-scale solar selective absorber coating to enhance the performance of a TEG module in solar thermal energy harvesting is presented. The thin film coating is fabricated by electrochemical deposition of a bimetallic layer of tin and nickel on copper substrate. Further, the use of vacuum packaging to limit heat losses from the collector plate is

examined. Limiting heat losses is shown to improve the overall efficiency of these devices. Also, a thermal scavenging technique that relies on phase change within the working fluid in a micro capillary channel heat exchanger is presented. These devices have the potential to provide autonomous power for micro electronics, and represent sustainable alternatives to battery-powered MEMS-based devices.

APPROVAL FOR SCHOLARLY DISSEMINATION

The author grants to the Prescott Memorial Library of Louisiana Tech University the right to reproduce, by appropriate methods, upon request, any or all portions of this Dissertation. It is understood that "proper request" consists of the agreement, on the part of the requesting party, that said reproduction is for his personal use and that subsequent reproduction will not occur without written approval of the author of this Dissertation. Further, any portions of the Dissertation used in books, papers, and other works must be appropriately referenced to this Dissertation.

Finally, the author of this Dissertation reserves the right to publish freely, in the literature, at any time, any or all portions of this Dissertation.

Author _____

Date 10-03-2013

DEDICATION

To my late father, Mazi Ogbonnaya Akaose, who was a lover of education. He encouraged and supported many people in the community to pursue their academic goals.

TABLE OF CONTENTS

LIST OF TABLES

LIST OF FIGURES

ACKNOWLEDGMENTS

In the journey of this dissertation research, I have had the pleasure to interact with many people that assisted in some measure towards achieving this end result. I am indeed very grateful to everyone of them and hope I can mention all the names here.

First, I would like to thank God, who is the source of all things and for whom we have life. Without Him, I would not have had the wisdom or the strength to finish this work. Thank you Lord.

I would like to most sincerely thank Dr. Leland Weiss for the privilege to work under his supervision. The research (and indeed other life) experiences gained during the course of this work would not have been possible without his support, guidance and encouragement. Thank you for all the insights.

I am grateful to Dr. Hisham Hegab, Dr. Heath Tims, Dr. Long Que and Dr. Erica Murray for being a part of my dissertation committee. I appreciate all the personal encouragements, motivation and positive comments. Thank you for allowing me to draw from your diverse and wealth of experiences.

I am also grateful to several other people that rendered technical help during this work. Thanks Ms. Debbie Wood for all the help in the machine shop and other equipment setup. I appreciate Mr. Donald (Dee) Tatum for helping with the E-beam evaporation machine. Mr. Ji Fang, thank you for the photolithography training.

Dr. Alfred Gunasekaran, thank you for your assistance with the scanning electron microscope. I am also grateful to Dr. Tom Hanson. (Hanson Collaborative, Napa CA), for his great help with the vacuum chamber.

Special thanks to the other members of Dr. Weiss' research group (past and present) that assisted in this work- Sunil Maharjan, Samuel Chukwu, Christopher Champagne and Suvhashis Thapa. Thank you for the time and knowledge (oh! and lab space) that we shared.

I would also like to acknowledge the support and prayers of friends and family. On several occasions that I felt like giving up on this work, I knew I couldn't disappoint you and your prayers kept me going. To my mum, brothers and sisters, thank you for the encouragement and support. You all let me be away from you these few years so I could pursue my goal. Thank you. Special thank you to Terwase for standing by me through this journey. Your support and encouragement has been and will continue to be tremendous. Thank you Idika Uzo, Israel Dare Popoola and Jonah Ukpai for your friendship and encouragement over the years. I would like to also show my appreciation to Engr. Ishaya Akai, Engr. John Alabi and Mr. Ademola Adeyemi for encouraging me to pursue my dreams.

Finally, I would like to gratefully acknowledge the support of this work by the National Science Foundation (NSF) via Grant No. *ECCS-1053729*, and the State of Louisiana Board of Regents (*LEQSF(2009-12)-RD-A-13*).

NOMENCLATURE

PV	Photovoltaic
A	Area
Q	energy
$\dot{Q}$	energy per unit time (Power)
E	quantum energy
h	Planck's constant ($6.626068 \times 10^{-34}\ \frac{m^2.kg}{s}$)
v	thermal radiation frequency
ρ	reflectivity
α	absorptivity
τ	transmissivity
q	energy per unit area per unit time
$\bar{U}$	overall heat-transfer coefficient
T	absolute temperature
ϵ	infrared emissivity
σ	Stefan-Boltzmann constant ($5.670373 \times 10^{-8}\frac{W}{m^2.K^4}$)
U	Overall heat transfer coefficient
h	convective heat transfer coefficient

R	Resistance
STC	Solar Thermal Collector
TEG	Thermoelectric Generator
$MEMS$	Micro-Electo-Mechanical Systems
P	Pressure
η	Efficiency
λ	Mean free path
K	Boltzmann constant 1.38×10^{-23} JK^{-1}
Kn	Knudsen number
N	Number of glass cover plates
β	Plate tilt angle
NU	Nusselt number
Ra	Rayleigh number
Gr	Grashof number
Pr	Prandtl number
TC	Thermocouple
MHE	Micro Heat Exchanger
$\dot{m}$	mass transfer rate
h_{fg}	Heat of vaporization

Subscripts

u	useful
c	collector
s	solar
e	absorber element of collector
a	ambient
d	diffuse
g	glass
p	plate
c_{p-g}	convection transfer from plate to glass
r_{p-g}	radiation transfer from plate to glass
c_a	convection transfer in ambient
r_{g-a}	radiation from glass to ambient
H	Hot
C	Cold
max	Maximum
pa	in Pascals
$Torr$	in Torr

Superscript

$-$	average

CHAPTER 1

INTRODUCTION

As the world energy demand continues to rise due to population growth and industrialization, there is a need to examine alternate energy sources to augment traditional fossil fuels for energy generation. More so, the forecasts of depletion as well as environmental impact of fossil fuel have led to more research on renewable and sustainable energy sources. Renewable energy sources are naturally and continually replenished sources. This includes sources such as wind, tides, geothermal heat, sunlight and rain. On the other hand, sustainable energy is the ability to meet the present energy needs without compromising the ability of future generations to meet their needs. Hence, naturally and continually (renewable) replenished energy sources will guaranty energy sustainability.

Solar energy is a renewable and sustainable energy source that is presently underutilized. It has been estimated that 30 min of solar radiation falling on the earth is equal to the world energy demand for one year [1]. Solar radiation intensity outside the atmosphere is $\sim$1,360 $\frac{W}{m^2}$. A portion of this intensity is however absorbed or scattered, before reaching the earth's surface, as the radiation travels through the atmosphere. Overall, the amount of incident solar radiation reaching the ground surface depends on the location's latitude, atmospheric conditions, and time of the day.

A peak insolation intensity value of 1,000 $\frac{W}{m^2}$ (or 1 sun) is often considered acceptable general estimate.

Energy from the sun can be utilized in two broad ways, namely direct and indirect solar energy. In direct solar power, there is only one step or change from the energy of the sun to usable energy. Direct solar energy harvesting in modern power generation typically involves either photovoltaic systems or large-scale solar thermal energy installations. On the other hand, indirect solar power goes through more than one step or change to become usable energy. Fossil fuels, bio-fuels, wind and hydroelectric are forms of indirect solar power as they are all influenced by sun light.

The next sections will present a closer look at direct solar energy technologies; namely, photovoltaics and solar thermal.

1.1 Photovoltaics

Photovoltaic (PV) systems rely on the direct conversion of light energy from the sun into electrical energy using solar cells. A solar cell is a semiconductor device that uses a p-n junction to convert solar energy directly into electricity [2]. PV modules absorb light from a source and converts some of it into electrical power and the rest of the incident radiation is converted to heat or re-emitted to the surrounding environment. PV technology is probably the most popular direct solar energy technology.

Solar cells are mostly made of silicon (monocrystalline, polycrystalline or amorphous). Other materials include Gallium arsenide (GaAs), Indium phosphide (InP), Cadmium telluride (CdTe) and copper indium galliium selenide/sulfide (CIGS).

Since PV relies on solid-state electronic process, it has the advantage of no moving parts. This makes PV a preferred technology from the standpoint of operation and maintenance considerations.

The first discovery of the photoelectric effect was in 1839 by Edmund Becquerel, a French physicist, when he found that certain materials would produce small amounts of electric current when exposed to light. Initial work on PV was focused on selenium until the 1950s when scientists at the Bell Laboratories, by accident created a silicon PV cell. The silicon PV cells they invented were 50 times more efficient at generating electricity than the selenium cells had been 20 years earlier.

One of the biggest challenges in the expansion of PV for large-scale power application is the high cost of solar cell module. However, with active research and development over the years, the price has continued to come down. From a price of more than \$30/Wp (peak watts) in 1974 [3], the price of PV module in 2010 was put at \$2.40/Wp [4]. It was also very interesting to see that the price of Chinese solar panels had dropped to \$0.60/Wp by December 2012 for crystalline modules [5]. Similarly, the average installed price of PV in the US fell from from \$7.90/W to \$6.20/W between 2005 and 2010 [4]. The price decrease of PV over the years has led to a significant increase in the total installed capacity. Global installed capacity had increased to more than 68 GW at the end of 2011 (an increase of 70% from 2010 data) [6]. This currently makes PV the third highest (after hydro and wind power) globally installed energy source.

Another significant challenge so far with the PV technology is the low efficiency of the system. The efficiency of PV systems are generally ≤ 20 %. A more detailed

review of PV efficiency for different materials or classifications is found in Ref [7]. On the other hand, although PVs are not very efficient, they are very scalable. Therefore, they are widely utilized both in macro and micro power generation.

1.2 Solar Thermal

The second direct solar power technique is the solar thermal process. Solar thermal technology harvests the heat energy of the sun. This heat is utilized to drive other mechanical or electrical systems for power production. Large scale solar thermal application is well established with thermal efficiencies greater than 80 % [8]. Though large-scale solar thermal energy generation is well advanced, literature on micro solar thermal energy is not readily available. Various heat engines and thermodynamic cycles are available for solar thermal applications. The work presented in this dissertation is focused on solar thermal technology for micro scale applications and subsequent chapters of this dissertation will highlight some of the heat engines and processes.

1.3 Objective and Thesis Structure

This work is focused on the integration of microfabrication processes and solar thermal technology to generate power for micro-scale applications. Microfabrication techniques allow for decrease in cost as multiple devices may be manufactured from each processing steps. Further, solar thermal energy is a cheap, renewable and sustainable energy source that is presently underutilized. This work proposes the use of sunlight as heat source for power generation utilizing micro-scale heat engines. The

use of a thermoelectric generator as a heat engine is proposed. Further, a thermal scavenging technique that relies on phase change within the working fluid in a micro capillary channel boiler plate is also proposed.

A more detailed review of solar energy, with particular attention on solar thermal processes is presented in Chapter 2. A review of the applications of solar thermal technology in micro scale power applications is also presented.

The integration of a thin film selective absorber coating and thermoelectric generator for micro scale solar energy harvesting is presented in Chapter 3. This demonstrates the use of solar thermal process in micro power application.

Chapter 4 presents performance analysis of a solar thermal collector in low thermal conductivity environment. The effect of thermal radiation on a body is shown and the steady-state temperature of a solar thermal thermal collector under different operation conditions are examined.

A study of a MEMS-based boiler for thermal scavenging applications is presented in Chapter 5. This device relied on low-grade heat source such as solar thermal energy for useful power output based on working fluid phase change. Chapter 6 presents an alternative, low cost method for the fabrication of a heat exchanger utilizing metal-based microchannels using the LiGA technique.

Finally, Chapter 7 presents a general conclusion of the study and offers recommendations for future work.

CHAPTER 2

REVIEW OF SOLAR THERMAL ENERGY PROCESSES

2.1 Introduction

Many research groups are actively exploring alternatives to battery-powered MEMS-based devices. One dominant technique is the harvesting of energy from the ambient. The most abundant source of energy for MEMS power applications is the ambient environment of application. Energy in the surrounding environment occur in the form of light, heat, vibration or radio frequency (RF) radiation. There are various transduction mechanisms that are available for harvesting these energies from the environment. The more established mechanisms for vibration-based energy harvesting include electrostatic, piezoelectric and electromagnetic transducers. In electrostatic transduction technique, a voltage change across a capacitor is created by the change in distance of two electrodes initiated by the vibration of the one movable electrode. Likewise in electromagnetic transducers, the vibration of a magnetic mass attached to a coil generates AC voltage from the resulting change in magnetic flux. On the other hand, piezoelectric transducers would generate a surface charge when subjected to mechanical stress.

The presence of temperature differences in nature and various devices, as well as the availability and interaction of light and radio frequency could also be utilized

to generate autonomous power for micro devices. Vullers et al [9] summarized the power output achievable from environmental sources when using optimized devices. More detailed review of energy harvesting techniques can be seen in Refs [10, 11, 12, 13, 14, 15, 16]. Miniaturized fuel cells have also been suggested as a possible replacement for battery-powered micro devices [17, 18]. In this work, thermal energy harvesting techniques for micro scale applications is examined. This chapter specifically reviews techniques and processes that rely on solar thermal energy as input for useful micro-scale power generation.

The sun is a sphere of intensely hot gaseous matter. The gaseous reactions within the interior of the sun produces large amounts of energy. This energy is transferred to the surface through conduction and convection processes, and then radiated into space. The temperature at the center of the sun is estimated at 8×10^6 - 40×10^6 K [8]. The emitted radiation carries with it energy and spreads in discreet quanta. The earth surface receives approximately 1.8×10^{11} MW of power annually from the sun [19]. This is much higher than all the other energy sources combined. Moreover, it is also free and available in most parts of the world.

Energy from the sun could be utilized directly either in the form of photovoltaic or solar thermal. The energy usually is first collected in the form of light for photovoltaic or heat for the solar thermal system. Hence, the collector remains a critical component of the solar energy system. This work focuses on the solar thermal systems.

2.2 Solar Thermal Energy

The solar thermal system could be grouped into two broad categories- concentrating and non-concentrating systems. The basic difference is that the non-concentrating collectors utilize the incoming solar radiation as is, whereas the concentrating collector systems utilize optical devices to increase the solar energy incident on the device. The optical devices, usually in the form of mirrors, in concentrating collectors lead to much higher temperatures in the absorber element. The non-concentrating type is usually used for low temperature applications while the concentrating type is applied in high temperature applications. Tracking devices are often used to follow and focus the sun's radiation on the absorber element in concentrating systems. The draw back of the concentrated solar power (CSP) system however is the high cost of the system itself and the solar tracking devices.

Based on the shape of the absorber element, the collector can be grouped into flat, tubular and point collectors. The flat type include flat-plate collector (FPC), evacuated tube collector (ETC), and the evacuated flat-plate collector (EFPC). The tubular collectors (with concentration) include the compound parabolic collector (CPC), linear Fresnel reflector (LFR), cylindrical trough collector (CTC) and the parabolic trough collector (PTC). Point collectors (with concentration) include parabolic dish reflector (PDR) and the heliostat field collector (HFC). More detailed descriptions of the various collector types are found in Refs [1, 8].

The traditional flat plate collector is made of four basic components- glazing, absorber, fluid tubes/fins and thermal insulation. The glazing is a clear plastic or glass sheet, highly transmissive to incident radiation but opaque to outgoing longwave

radiation from the absorber surface. The glazing is also useful for minimizing convection losses and for protecting the absorber surface from other adverse weather conditions. The absorber element converts incident radiation into heat energy, and then transfers the heat energy to the fluid tubes. The tubes/fins serve as heat exchangers for the absorber plate. Thermal insulators are used to eliminate heat leakages from the sides and bottom of the assembled collector box. Figure 2.1 shows the basic design of a traditional flat plate collector.

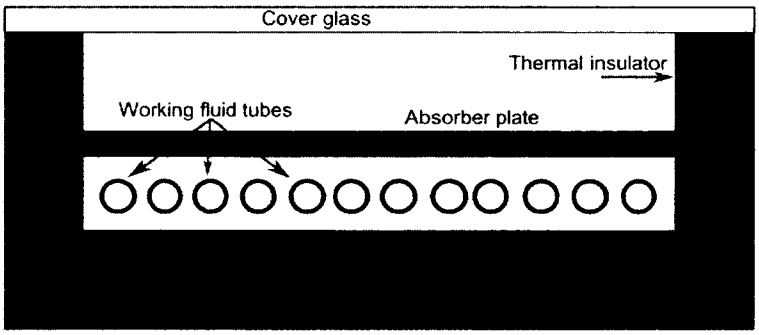

Figure 2.1: Traditional Flat Plate Collector

2.2.1 Traditional Absorber

The traditional solar thermal collector operates by absorbing heat on a surface and transferring the heat to a working fluid. The amount of heat absorbed is therefore limited by the surface area of the collector. Also the overall efficiency of the system is affected by how well heat energy absorbed can be transferred to the working fluid.

Absorber plates are generally made of high thermally conductive materials. The absorber plate is the most important component of the solar thermal system. It is the component that transforms incident radiation into heat energy. The surface of the collector is generally coated with black paint or a selective absorber to increase thermal

absorption. However, black paint, or surfaces that are perfect absorbers (in the solar radiation range, $0.3 - 2.5\ \mu m$), also have high emissive values in the infra-red range ($> 2.5\ \mu m$). By contrast, so-called "selective" absorber surfaces maximize absorption of incident radiation but show reduced emittance in the infra-red region.

Advanced absorber substrates are typically covered with a coating that strongly absorbs in the solar radiation wavelength range in order to obtain high values of absorptivity, while yielding reduced emittance in the infrared region [8]. A perfect absorber, also known as a *blackbody*, will absorb all the incident radiation that falls on it. However, a blackbody is also a perfect emitter, and will therefore emit long wavelength radiation energy away from its surface. A desired absorber element will therefore maximize all incoming solar radiation and minimize heat losses that would otherwise occur through infrared emission from the collector surface. This quality describes the selectivity of a material. Selective surface is the characteristic of high absorptivity for incoming solar radiation and low emissivity for outgoing re-radiation. The concept of solar selective coating was first introduced by Tabor, and has been studied since 1950 [20]. A detailed review of selective absorber materials is presented in [21], in which the author grouped selective absorber coatings into six distinct types.

- Intrinsic: The selectivity is an intrinsic property of the material.
- Semiconductor-metal tandems: The semiconductor layer absorbs short-wavelength radiation while the metal layer reduces emittance.
- Multilayer absorber: Multiple layers of materials with different optical characteristics are arranged in such a way as to become efficient selective absorbers.

- Metal-dielectric composite coatings or absorber-reflector tandems utilize highly absorbing coating in the solar spectrum and transparent in the IR, on a highly IR-reflective metal substrate. It is made of fine metal particles embedded in a dielectric or ceramic matrix or a porous oxide impregnated with metal.
- Textured surface: Enhanced surface texture of a material can improve its absorption and emissivity values. The shape and size of the microstructures of the coating is adjusted to yield the desired spectral selectivity.
- Selectively solar-transmitting coating on a blackbody-like absorber: This is mostly a highly doped semiconductor over a long term durable absorber. This is mostly used for low-temperature application.

2.2.2 Direct Absorber Solar Collector (DASC)

In the DASC system, a highly thermal absorbent fluid flows in transparent channels, and the solar radiation is absorbed directly by the liquid without requiring an intermediate absorber plate. The "black" fluid serves as both the absorber and the working fluid, as illustrated in Figure 2.2. This eliminates the "black" metal absorber surface. The elimination of a metal component will reduce cost as well as eliminate corrosion issues. Further, this minimizes the heat transfer process and losses between the absorber and the working fluid, as heat is absorbed directly into the working fluid.

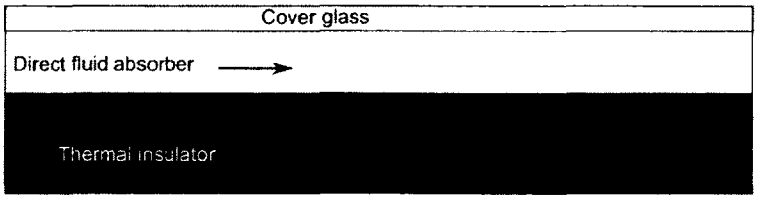

Figure 2.2: Direct Solar Absorber Collector Design

Addition of nanoparticles to conventional working fluids has the potential of improving the heat transfer and solar collection in solar thermal systems [22, 23, 24]. Volumetric absorption is achieved by suspending nanoparticles in base fluid so as to alter the optical properties of the base fluid. Some of the criteria in selecting a nanofluid for direct solar absorption include spectral absorptivity and emissivity, specific heat, boiling and freezing points, toxicity, flammability, chemical stability, cost, etc. The use of carbon-black and black antimony sulfide, Sb_2S_3, have been suggested [25]. Other nanoparticles may also be used.

The volume fraction of nanoparticles mixed with a base fluid is critical in a direct solar absorption system. A very high concentration of nanoparticles in the base fluid could lead to formation of a thin layer near the surface of the fluid and then most of the sunlight is absorbed within this thin layer rather than in the entire volume. On the other hand, a small concentration could mean that a great deal of the light is not absorbed in the fluid. Also, the size, shape and optical properties of the nanoparticles, as well as the base fluid are important parameters for efficient performance. More detailed review of DASC is found in Refs [26, 22, 23]. This work is focused on the traditional flat plat collector type. Next, an analysis of the effects of the collector components is presented.

2.2.3 Effects of Flat Plate Collector Parameters

2.2.3.1 Transmissivity-absorptivity product ($\tau\alpha$)

If it is assumed that there is no radiation absorption within the glass cover of a collector plate, then the reflected and transmitted radiation account for the radiation

incident on the cover glass. When the transmitted radiation strikes the absorber surface, a part of it is absorbed while the rest of it is reflected back to the glass cover. This assumes there is no radiation transmission through the absorber plate. As shown in Figure 2.3, when the reflected radiation from the absorber plate strikes the cover glass, a portion of it is transmitted to the ambient while the rest is reflected back to the absorber plate. This process goes on indefinitely.

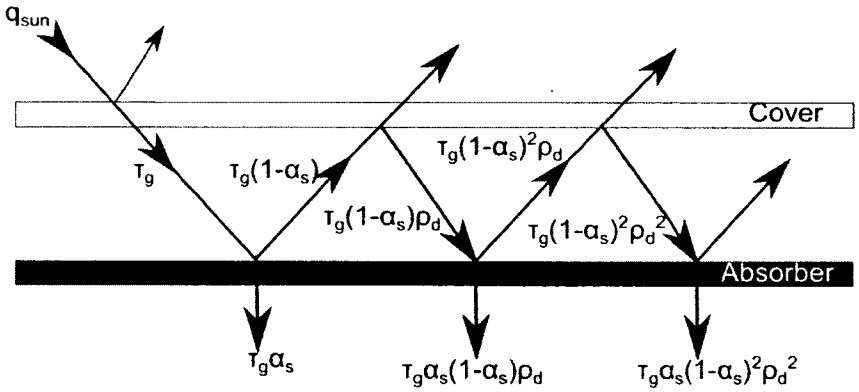

Figure 2.3: Effect of Thermal Radiation on a Surface

The net fraction absorbed $(\tau\alpha)$ is given by Equation 2.1, where ρ_d is the diffuse reflectivity from the glass cover piece [19].

$$(\tau\alpha) = (\tau_g\alpha_s)[1 + (1-\alpha_s)\rho_d + (1-\alpha_s)^2\rho_d^2 + ...]. \tag{2.1}$$

The higher order terms in the series approach zero. Hence, neglecting the higher order terms, the trasnmissivity-absorptivity product is given by Equation 2.2.

$$\begin{aligned}(\tau\alpha) &= (\tau_g\alpha_s)[1 + (1-\alpha_s)\rho_d] \\ &= \frac{\tau_g\alpha_s}{1-(1-\alpha_s)\rho_d}.\end{aligned} \tag{2.2}$$

As can be inferred from Equation 2.2, in order to achieve high values of $(\tau\alpha)$, the following conditions are critical.

- Highly transmissive (τ_g) glass material.
- High solar absorptive collective plate (α_s).
- Low reflective glass material (ρ_d).

2.2.3.2 Surface emissivity (ϵ)

The temperature of the absorber plate increases as it absorbs incident thermal radiation. This rise in temperature causes the absorber plate to in turn become a radiating surface. The plate surface absorbs incoming short wavelength radiation from the sun, and emits long wavelength radiation to the surrounding environment. The energy emitted from the surface of a body is directly proportional to the fourth power of the absolute temperature of the body and its surface area [27] as shown in Equation 2.3. The introduction of proportionality constant yields Equation 2.4.

$$Q \propto A_e(\bar{T_e}^4 - T_a^4). \tag{2.3}$$

$$Q = \epsilon\sigma A_e(\bar{T_e}^4 - T_a^4), \tag{2.4}$$

where ϵ is the surface emissivity and σ is the Stefan-Boltzmann constant (5.670373 $\times\ 10^{-8}\frac{W}{m^2.K^4}$). It is therefore apparent that in order to lower the energy emitted by the absorber surface, a low emissive value ϵ is required. Hence, advanced absorber substrates are typically coated with materials that strongly absorb incident solar irradiation thereby yielding high values of absorptivity, while also limiting emittance in the infrared region [8].

2.2.3.3 Thermal insulation

Heat losses from the collector plate lowers the collector's overall useful heat gain. The overall heat loss coefficient from the top, sides and bottom of the collector is represented by $\bar{U}$. Since the sides and bottom of the plates are usually insulated, the top losses account for and closely approximate the total energy loss. Convection and radiation losses between the parallel plates (collector and cover glass) account for the total heat loss from the top of the collector.

In a flat plate solar collector, the energy loss through the top of the plate is a combination of convection and radiation losses. For a unit area, the loss is equal to the convection (c) and radiation (r) heat transfer from the absorber plate (p) to the cover glass (g), as shown in Equation 2.5.

$$\begin{aligned} q_{loss,top} &= h_{c_{p-g}}(T_p - T_g) + \frac{\sigma(T_p^4 - T_g^4)}{\frac{1}{\epsilon_p} + \frac{1}{\epsilon_g} - 1} \\ q_{loss,top} &= h_{c_{p-g}}(T_p - T_g) + h_{r_{p-g}}(T_p - T_g) \\ q_{loss,top} &= (h_{c_{p-g}} + h_{r_{p-g}})(T_p - T_g). \end{aligned} \tag{2.5}$$

Similarly, the heat loss from the glass cover to the ambient (a) is the sum of the radiation and convection losses as shown in Equation 2.6. The sun is treated as a blackbody with solar emissivity ϵ_s equal to unity.

$$\begin{aligned} q_{loss,glass} &= h_{c_a}(T_g - T_a) + \frac{\sigma(T_g^4 - T_a^4)}{\frac{1}{\epsilon_g} + \frac{1}{\epsilon_s} - 1} \\ q_{loss,glass} &= h_{c_a}(T_g - T_a) + \epsilon_g \sigma(T_g^4 - T_a^4) \\ q_{loss,glass} &= (h_{c_a} + h_{r_{g-a}})(T_g - T_a). \end{aligned} \tag{2.6}$$

The thermal resistance R between two surfaces is defined as the resistance to the flow of heat and is given by the difference in temperature divided by the total heat flow between the surfaces as shown in Equation 2.7. Since this requires that all of the heat which flows through surface 1 also flows through surface 2, there is no net heat gain within the volume.

$$R = \frac{\Delta T}{q}. \tag{2.7}$$

From Equation 2.5, the thermal resistance between the absorber plate and the collector cover is given by Equation 2.8 while Equation 2.9 defines thermal resistance between the cover glass and the ambient.

$$R_{top} = \frac{1}{(h_{c_{p-g}} + h_{r_{p-g}})}. \tag{2.8}$$

$$R_{glass} = \frac{1}{(h_{c_a} + h_{r_{g-a}})}. \tag{2.9}$$

The total thermal resistance, R_{total}, to the surroundings is then given by the sum of the resistances as shown in Equation 2.10.

$$R_{total} = R_{top} + R_{glass} = \frac{1}{(h_{c_{p-g}} + h_{r_{p-g}})} + \frac{1}{(h_{c_a} + h_{r_{g-a}})}. \tag{2.10}$$

The overall heat transfer coefficient, $\bar{U}$, is the inverse of the total thermal resistances R_{total} to the flow of heat between the two surfaces. Hence, $\bar{U}$ is as shown in Equation 2.11.

$$\bar{U} = \frac{1}{R_{total}} = \frac{1}{R_{top} + R_{glass}} = \left(\frac{1}{(h_{c_{p-g}} + h_{r_{p-g}})} + \frac{1}{(h_{c_a} + h_{r_{g-a}})} \right)^{-1}. \tag{2.11}$$

From Equation 2.11, the overall heat transfer coefficient could be minimized by lowering or eliminating convection between the collector plate and glass cover. This may be achieved using transparent insulating materials, vacuum insulation technique or

by filling the volume with low thermal conductivity gases. Further, limiting radiation transfer from the collector plate and glass cover also reduces the overall heat transfer coefficient.

2.3 Micro Solar Thermal Applications

Solar thermal energy can be utilized in a number of ways. Typically, the thermal collector works by absorbing incoming solar radiation and converting same to heat which is thereafter transferred to a working fluid. The heated fluid is then used to generate electrical or mechanical work output. Alternatively, the absorbed heat could be utilized for many other applications. Generally, such applications include water heaters, solar cookers, driers, ponds, architecture, air-conditioning, chimneys, power plants, water purification and distillation [28].

On a micro scale, the use of thermoelectric generators to harvest solar thermal energy for useful power application has been demonstrated [29, 30, 31]. The TEGs utilize the heat from the absorber plates to generate power output. In addition to TEGs, solar thermal energy may also be used to drive a phase change in a working fluid when integrated with a heat exchanger. MEMs-based heat engines for power generation are being developed that rely on this phase change for useful power output [32, 33, 34, 35].

Another potential application of solar thermal energy on a micro scale is in heating a microreactor. Zimmerman et al [17, 36] have proposed and modeled the use of micro solar heater as input heat in microreactors for hydrogen production by methanol reforming. The ability to produce hydrogen on-site where it is needed

helps overcome transportation, storage and safety issues. The collector, bonded to a microfluidic channel, is expected to supply the energy needed to achieve the temperature required (250 – 300 °C) for methanol reforming within the microreactor. Hydrogen produced in this process serves as the fuel for a proton exchange membrane fuel cell (PEMFC).

A combined micro light and thermal energy harvesting cell has also been reported [37]. The energy cell consists of a carbon nanotube film (CNF) integrated with a lead zirconate titanate (PZT) cantilever, and converts light and thermal energies into electricity. This device is based on actuation of CNF upon illumination by light and thermal radiation. It was shown that as the CNF absorbs and converts photon energy into thermal and electrostatic energy, there is a rapid temperature rise of the CNF leading to its expansion and actuation. The light and/or thermal radiation would cause the CNTs to stretch, bend, and repel. These mechanisms of the CNF-PZT cantilever lead to a self reciprocation of a CNF-based cantilever upon exposure to light and thermal radiation.

2.4 Conclusion

Solar thermal energy harvesting techniques for micro scale power applications have been presented. These devices utilizing the heat from the sun as input have the potential to provide autonomous power for micro electronics. This chapter specifically reviewed techniques and processes that rely on solar thermal energy as input for useful power generation.

The efficiency of a solar thermal system is a measure of how much of the incoming solar thermal energy that can be transferred to the working fluid or other applicable heat engines. Improving heat absorption on the absorber plate by maximizing absorption while reducing emittance, as well as improving the heat transfer efficiency between the absorber element and the working fluid or heat engine will improve the overall collector efficiency. Also, limiting heat losses from the collector to the ambient enhances the overall system efficiency. Irrespective of the heat engine applied, one critical parameter in the operation of the device is the temperature gradient resulting between the heat source and sink. Higher temperature gradients typically lead to increased efficiency.

CHAPTER 3

MICRO SOLAR ENERGY HARVESTING USING THIN FILM SELECTIVE ABSORBER COATING AND THERMOELECTRIC GENERATORS[†]

3.1 Introduction

Solar energy is a clean and sustainable energy source that has a potential for present and future world energy needs. The earth surface receives approximately 1.8×10^{11} MW of power from the sun each year [19]. This is significantly higher than commercial energy sources currently available. It has been estimated that 30 min of solar radiation falling on the earth is equal to the world energy demand for one year [1]. Moreover, solar power represents free and available energy in many parts of the world. Energy from the sun can be utilized in multiple ways. Direct use in modern power generation typically involves either photovoltaic systems or large-scale solar thermal energy installations. While large-scale solar thermal energy generation is well advanced, there has been comparatively little research on smaller scale thermal energy collection and application. The work contained in this chapter examines the fabrication, characterization, and testing of a selective absorber coating for micro solar thermal energy harvesting.

[†]This material has been published as Ogbonnaya, E., Gunasekaran, A., and Weiss, L., 2013. "Micro solar energy harvesting using thin film selective absorber coating and thermoelectric generators". Microsystem Technologies, 19(7), pp. 995-1004 and is being reproduced with the kind permission of the publisher (Springer Science and Business Media) and co-authors.

Although widely available, there is a significant challenge to the utilization of solar energy for power production. This is because it represents a weak energy source on the earth's surface. Radiation flux, even in very hot regions of the world, rarely exceeds 1 $\frac{kW}{m^2}$ and the total radiation in a day is typically lower than 7 $\frac{kWh}{m^2}$ [19]. This means that large collection areas are required to produce significant output power. To assist in this collection, the use of concentrating devices can be applied to increase the amount of energy captured as is done in large, mega-Watt scale solar thermal applications.

On the smaller scale, solar energy harvesting has typically focused on the direct conversion of light to electrical energy through the use of solar cells [38, 39, 40, 41]. Solar thermal energy harvesting has been limited to macro scale devices. One method of utilizing solar thermal energy on a small scale is via thermoelectric generator, TEG. Other small scale thermal devices requiring heat as input energy are also available. TEGs have been shown to provide enough power output for practical applications based on temperature difference [31, 42, 43, 44]. In addition to TEGs, solar thermal energy may be used to drive a phase change in a working fluid when integrated with a heat exchanger. MEMs-based heat engines for power generation are being developed that rely on this phase change for useful power output [32, 33, 34, 35]. The work presented in this chapter specifically considers the fabrication and characterization of a small-scale Solar Thermal Collector (STC) with nanometer scale coating that can be applied to these various devices requiring thermal energy input. In this manner, autonomous power sources are developed, capable of transforming solar energy to useful power output.

In this work, the STC serves as a major component of the solar energy system. Solar radiation that is incident on the STC is absorbed and transformed into heat. Traditionally, solar thermal collectors have been fabricated using high thermal conductivity materials like copper or aluminum, though they can also be made of plastic for very low temperature applications like swimming pool heating [45]. In some cases, the surface may be coated with black paint or a selective absorber. Black paint or surfaces that are perfect absorbers (in the solar radiation range, 0.3 - 2.5 μm) also have high emissive values in the infrared range ($> 2.5\ \mu m$).

By contrast, selective absorber surfaces maximize absorption of incident radiation but show reduced emission in the infrared region. Hence, advanced absorber substrates are typically covered with a coating that strongly absorbs in the solar radiation wavelength range in order to obtain high values of absorptivity, while yielding reduced emittance in the infrared region [8]. Electrochemical deposition has been previously used for preparing these selective absorbers. This has been due to the cost effective nature of this technique and the relative simplicity of the technique itself [19]. Other techniques for preparing the selective absorber coating include sputtering, Chemical Vapor Deposition (CVD), chemical oxidation, sol gel, and painting [21]. Black chromium has been a predominant and successful material used to prepare selective absorbers [19]. However, due to the toxicity of the plating bath and high energy consumption of this process itself, other materials have been investigated [46]. Previous work has indicated black nickel-tin selective coating has promising potential as a highly effective selective absorber structure [46, 47]. The electrolyte used in

preparing the nickel-tin selective surface is less hazardous and operates at about a near-neutral pH.

In this present work, initial steps toward a complete, fabricated millimeter scale STC are investigated and reported for future inclusion with MEMS devices. In its final form, the STC will consist of both an advanced collector surface as well as a low thermal conductivity volume that seals this surface. Through the use of both an enhanced collector surface and sealed low conductivity volume, small wavelength solar energy is collected while long wavelength thermal energy, resulting from the heated collector surface, is restricted from transferring back to the surrounding environment. In final form the STC will provide the thermal power necessary to drive thermoelectric or other competitive power generation devices.

Figure 3.1 illustrates the basic concept of the design studied in this work. The basic components of the design include the absorber plate, upper transparent cover and the collector box. The upper cover is made of material that is highly transparent to incoming radiation and opaque to long wavelength radiation emitted by the absorber. Glass material that meets this requirement will be selected in final applications. The collector box serves to eliminate losses due to convection from the absorber plate. In the final design, the collector box is evacuated in order to eliminate convection losses as well as conduction losses that result from gas molecules within the collector box. The absorber plate is a critical component of this design and the subject of this investigation. It is the component that transforms the incident radiation into heat energy and delivers that energy for useful mechanical or electrical output work from an attached power generation device.

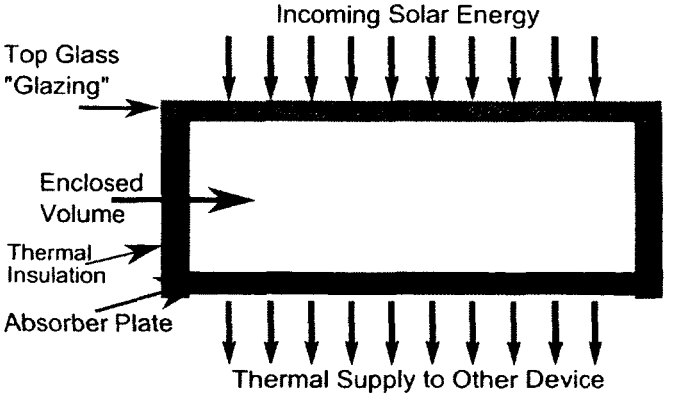

Figure 3.1: Solar Thermal Collector Design

This chapter focuses specifically on the fabrication and evaluation of several collector surfaces as a critical first step toward full STC fabrication and deployment in real-world application. Following this initial investigation, the fabricated collector surface is utilized to power a commercially available TEG. The ability of these collector surfaces to harvest solar thermal energy is examined based on simulated solar thermal input. Fabrication of the devices is based on techniques that include electrochemical deposition of nickel-tin coating on copper substrates. Characterization includes respective surface microscopy and spectroscopy of the coating and the final operating temperature as well as heat flux absorbed and transmitted through the devices themselves. Comparisons of the various devices are based on their respective heat flux absorption performances and final operating temperature.

3.2 Experimental Methods

3.2.1 Fabrication

Two types of flat plate solar collectors were studied as part of this work. The specifics of the design and fabrication of the collector plates are presented in this

section. Each collector plate had an overall surface area of 40 mm by 40 mm with total thickness on the order of 200 μm. This size was selected to allow for easy integration with off-the-shelf TEGs, which have similar surface area. In integration with MEMS devices like future commercially available TEGs, the presented STC can be easily downsized as necessary while maintaining its microscale thickness. Copper was used to form the substrate for each STC fabricated and characterized in these experiments. Copper was selected due to its excellent thermal conductivity. The high thermal conductivity ensured the absorbed heat could be readily conducted through the plate where it would be made available for power applications. Furthermore, the high resistance of copper to corrosion has previously been demonstrated to make it highly suitable in other solar thermal collector applications [48].

First, bare polished copper was used as a collector plate. This allowed for the characterization of baseline performance data. The thickness of the copper plate was 200 μm. The second type of collector plate was created using a thin film nickel-tin selective absorber coating formed atop a copper substrate. The creation of a collector plate with selective coating allowed for comparison of the heat flux absorptivity performance with that of the bare flat plate collector. Two fabrication steps were required to create the selective absorber coating. The first step involved the fabrication of a nickel under coat layer from a sulfate Watt-type warm bath [49]. This was followed by the fabrication of a thin layer of nickel-tin selective absorber coating from a near-neutral electrolyte at room temperature [47]. Electrochemical deposition technique was used for the fabrication of both layers.

The copper substrates were initially polished mechanically and then degreased in a solution of 5 % acetic acid and pinch of salt. They were next rinsed with DI water. This prepared the substrate for deposition of the various materials necessary for selective absorber generation. In a process similar to Shanmugam et al, an intermediate layer of nickel was initially electro-deposited to a thickness of 10 μm [47]. The electrochemical conditions for the nickel plating are shown in Table 3.1. All chemicals used were reagent grade from Sigma-Aldrich®.

Table 3.1: Electrodeposition Conditions for Nickel Layer

Component	**Concentration (g/l)**
Nickel Sulfate Hexahydrate	250
Nickel Chloride hexahydrate	45
Boric acid	30
Parameter	**Working Condition**
Temperature (C)	45
Current density $\frac{mA}{cm^2}$	50
pH	4.0

Electroplated nickel coatings for decorative applications are protective, mirror bright and smooth [50]. The mirror surface allowed the STC to be thermally "transparent" to incident radiation thereby allowing for optimum absorption of incident radiation. Previous research has also shown that a layer of Ni between the substrate and the selective absorber coating ensured better stability of the absorber plate at higher temperatures [51]. The deposition of the nickel layer readied the substrate for selective absorber coating. Figure 3.2 (a) shows an STC substrate with mirrored nickel surface finish.

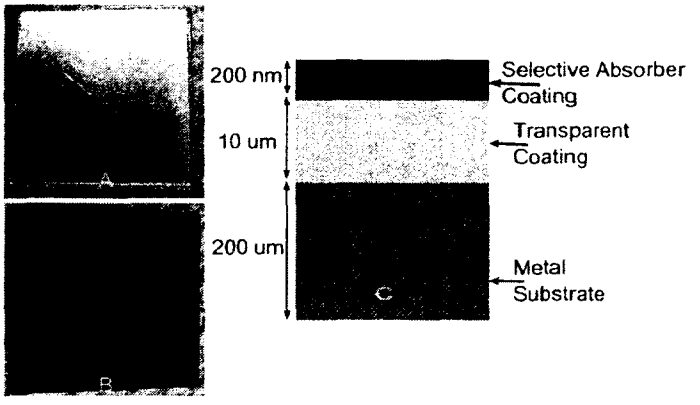

Figure 3.2: Nickel Coating (A), Black Nickel-Tin Surface (B), Coating Schematics (C)

Following the intermediate layer of nickel, a thin layer of nickel-tin selective absorber was deposited on the substrate. Previous work has indicated an effective black selective coating results from thicknesses in the range of 100 - 200 nm [47]. The electrodeposition condition of the bath used in this work is shown in Table 3.2. Diethanolamine was used both as a complexing agent and to raise the pH of the bath to a near-neutral level.

Table 3.2: Electrodeposition Conditions for Nickel-Tin Selective Absorber Layer

Component	**Concentration (g/l)**
Nickel Chloride	100
Stannous chloride	5
Ammonium bifluoride	25
Diethanolamine	
Parameter	**Working Condition**
Temperature (C)	25
Current density mA/cm^2	25
pH	6.5
Time (s)	20

The plating of the selective coating concluded the fabrication steps for the STC. It is important to note the environmental advantages to this plating technique.

Whereas most previous work has concentrated on the use of chrome as the absorber coating, the method employed in this work was less hazardous than the chrome bath. In addition, this process was performed at room temperature as a further benefit. The deposition of a thin layer of bimetallic nickel-tin coating produced a selective collector plate ready for testing. Figure 3.2 (b) shows the black selective nickel-tin coating. Following fabrication, the thermal collectors were characterized to determine the effect of the selective surface on the heat absorption capacity of the plate.

To arrive at the final coatings, different fabrication optimization processes were followed. These intermediate steps produced various forms of collector plate coatings. Some of the parameters that were varied before reaching the final fabrication procedure included current density, plating time, bath agitation, temperature and pH. First, current density was kept at values below 15 $\frac{mA}{cm^2}$ while other plating parameters were kept constant. Deposits were scarcely formed below current density of 15 $\frac{mA}{cm^2}$. This could be attributed to low throwing power at such low current densities. However, coating deposits were seen for current density in the range of 15 - 30 $\frac{mA}{cm^2}$. Beyond 35 $\frac{mA}{cm^2}$, coarse grains were formed instead of smooth or uniform black deposits. These larger deposits also displayed poor adhesion and were easily removed via accidental surface contact.

Another critical parameter in the fabrication process was the duration of the plating. Different plating time produced different coatings. It was interesting to observe the variety of coatings formed over time. For instance, 20 minutes of plating time produced very coarse coating grains. Similarly, one hour of plating further amplified the course granular structure. As the plating time reduced, the coating

grains became more uniform. Best results were obtained for deposition time of between 15 - 30 seconds where deposition was uniform. Below 15 seconds duration the coating did not completely cover the surface.

Bath agitation was also varied during the development of the final electroplating process. A mechanical stirrer was used to agitate the bath. Plated samples were studied as the rate of agitation was varied. Overall, the stirrer speed on a hot plate was varied from 0 - 1150 rpm. The deposits formed at lower stirrer rates were smooth and more uniform than at higher agitation rates. As the speed of agitation increased, the deposits became increasingly coarse. Overall, the best performance was observed during plating with no agitation as this showed uniform and smooth depositions. Hence, the final process that produced collector plates utilized in this work were produced without agitation during electroplating.

pH adjustment was also investigated where both ammonia and diethanolamine were varied. Though ammonia served well in adjusting the pH, diethanolamine had the added advantage of serving as a good complexing agent. Sn (−0.14 V) and Ni (−0.25 V) are close on the electrochemical series table and so can be codeposited readily. However, the high overvoltage of nickel deposition could cause only tin to be deposited from the bath. Metal potentials were brought closer by the use of complexing compounds which lower the activity of the more electropositive metal. Diethanolamine was used in this experiment as the complexing agent, and to raise the pH of the bath to a final value of 6.5.

It is also important to note that the bimetallic coating described in this work was different from a tin-nickel alloy. A traditional tin-nickel alloy is an intermetallic

compound of $\sim$ 65 % tin and $\sim$ 35 % nickel by weight. It has a faint rose-pinkish color and is resistant to tarnish [50]. Hence, work on this nickel-tin bimetallic solar selective absorber coating should not be confused with the traditional tin-nickel alloy.

3.2.2 Test Setup

Tests were conducted to evaluate the absorber and its potential for solar thermal energy scavenging. This section describes the testing and test setups for these experiments. As an initial step, the structure and elemental composition of the coating was examined. A Hitachi S4800 Field-Emission Scanning Electron Microscope (FESEM) was used for the analysis. The SEM micrographs revealed the structure of the coating and the size of the crystals. Similarly, an Energy Dispersive X-ray Spectroscopy (EDX) on the FESEM was used to analyze the elemental composition of the coatings.

The FESEM study was followed by analysis of thermal performance of the collector. Three types of experiments were conducted. The first measured the temperature of the collectors when exposed to simulated solar radiation. The second measured heat flux conduction from the collector to a steady state heat sink. In the third experiment, the collectors were coupled to the hot side of thermoelectric generators and the output power from the TEGs was measured. These represented key elements of the STC characterization effort. The ability of the collector to achieve high temperature is critical to power thermal-electrical conversion devices like thermoelectric generators. Similarly, a measure of the absorbed heat flux when compared to the incident flux is critical for effective power generation in a system reliant on thermal

energy as input power. Furthermore, the integration of the collectors with TEGs demonstrated a practical step in the use of this selective absorber coating to enhance thermal energy harvesting for useful power generation. Overall, the temperature profiles and heat flux conducted through the plates were characterized to determine the ability of the collector plates to transform solar radiation into useful heat input. The power output from the TEGs integrated with collectors was also characterized to validate the performance of each collector in providing input thermal energy for the TEGs. In all tests, the temperature of each collector, the heat flux reaching and passing through the collector and the output voltage from the TEG was monitored when exposed to simulated solar radiation until steady state conditions were reached. This produced results that were both reliable and repeatable.

In these investigations, a solar simulator was used for the experimental analysis. All tests were conducted by exposing the collector plate to incident radiation from the lamp. A halogen lamp was used to simulate solar radiation in this experiment. The simulator lamp used was the Sun System®SS-2 MH 400W lamp. Several methods were used to characterize and validate the use of this halogen bulb as a solar simulator. Like the sun, the intensity of the radiation from the lamp varied with distance. As the distance from the lamp increased, the intensity of output decreased. A Hukseflux®SR11 pyranometer was used to validate the intensity of the radiation at various distances from the simulator lamp. The pyranometer provided a measure of the broadband solar irradiance on a planar surface. Hence, the flux density of the solar irradiance at various heights from the lamp was characterized. This information was used to select an appropriate distance from the lamp which simulated flux density closely

approximating real world availability. A z-axis laboratory jack was used in adjusting the height of the test setup from the lamp.

A thin-film heat flux sensor was further used for simulator validation. The sensor was exposed to incident radiation from the solar simulator to verify the heat flux from the lamp. The sensor used was an Omega®thin-film flux sensor HFS-4. The sensor was placed at the same distance from the lamp as the pyranometer. The back side of the heat flux sensor was coupled to a heat sink to ensure incident radiation heat was readily pulled across the sensor into the heat sink. Thus, a good approximation of the incident flux was established and compared to the pyranometer measurement. A Custom-Thermoelectric®water block WBA-1.62-0.55-CU-01 was used as the constant temperature heat sink. Thermal grease was applied between the heat sink and the sensor to minimize thermal resistance. The thermal grease was OmegaTherm®201. A MityFlex®913 variable speed peristaltic pump was utilized to drive water through the heat exchanger block. The use of the heat sink ensured a constant and dependable cold-sink temperature for STC thermal testing. Figure 3.3 shows the basic setup for these validation experiments.

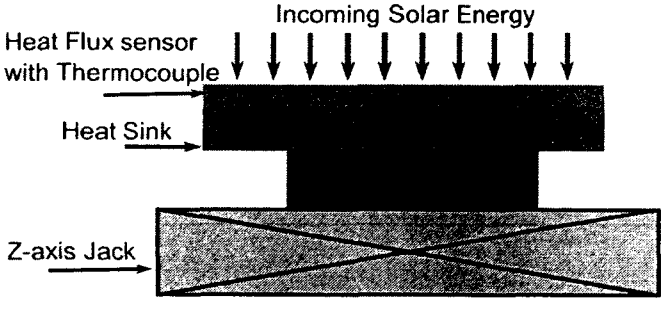

Figure 3.3: Basic Experimental Setup

As previously noted, the radiation flux in hot regions of the world rarely exceeds 1000 $\frac{W}{m^2}$. With this in mind, simulated solar radiation intensity was maintained below this incident value. An intensity of approximately 900 $\frac{W}{m^2}$ was selected. The pyranometer was used to determine the required distance from the simulator lamp and was verified by the flux sensor. 900 $\frac{W}{m^2}$ of heat flux was obtained 6 inches from the lamp. To minimize any convection losses during experimentation, the experiment was placed in an enclosed chamber. The chamber consisted of an acrylic canister with an air tight seal. Acrylic was selected due to its high transmissivity of incident irradiation. The transmissivity of the acrylic lid was verified by passing the simulated solar radiation through the lid and measuring its flux density via Pyranometer. The result showed that the acrylic had a transmissivity of 0.98. This amounted to a radiation intensity of approximately 880 $\frac{W}{m^2}$ reaching sample surfaces inside the acrylic canister, still well within typical solar radiation values.

Temperature profiles of the various collector plates that resulted from exposure to the solar simulator were monitored using thermocouples. Omega®PFT2NPT/2K and SA1-k-120 thermocouples were used. Thermocouple wires were passed through the bottom and side of the canister and sealed with epoxy to maintain the isolated environment. To verify recorded collector temperatures were due to direct absorption rather than re-heating via greenhouse effect in the chamber, the temperature of the chamber and the absorber was simultaneously monitored. The thermocouples were linked to a computer using a National Instruments®cDAQ-9174 data logger. Figure 3.4 shows the setup for the thermal analysis.

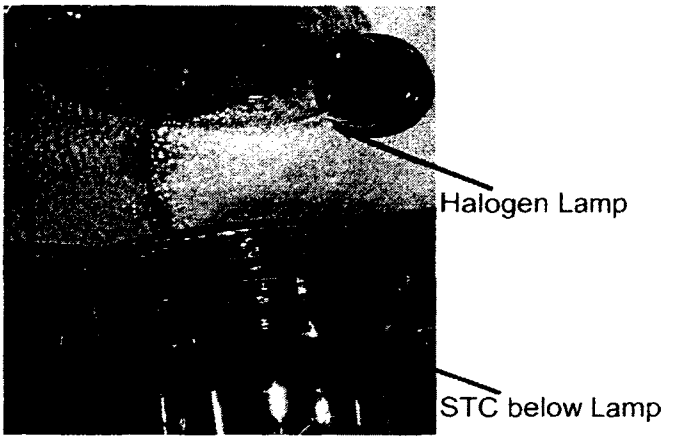

Figure 3.4: Solar Simulator Setup for Temperature Measurement

Actual heat transfer from the STC to the cold sink was monitored via heat flux sensor, similar to the sensor used in initial test setup validation and characterization. The sensor was placed between the collector plate and heat sink as noted in Figure 3.5. The sensor represented small thermal impedance to the overall heat transfer from collector to sink. This value was known and recorded as 0.004 °C per $\frac{W}{m^2}$ from the manufacturer. Analysis indicated this added insulative layer, on the order of 180 μm, was not a significant barrier to heat transfer.

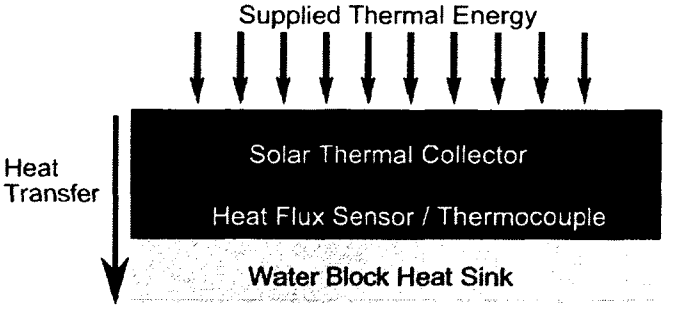

Figure 3.5: Schematics of Heat Flux Measurement Setup

Initial tests were conducted using a plain copper plate as the STC. This provided a baseline for all future comparisons. Both temperature of the STC and surrounding chamber were monitored until steady state was achieved. Following the baseline analysis, plates with selective absorber coating were utilized and compared to these baseline runs. Following the temperature analysis, the heat sink was coupled to the STC and flux measurements were performed. Similar to the temperature measurements, first a baseline copper plate was studied followed by the advanced selective absorber. Like temperature characterization, the heat flux analysis demonstrated the effectiveness of the STC in harnessing incident solar thermal energy.

Finally, as a practical step in solar thermal energy harvesting, the absorber plate was coupled to the hot side of a TEG for useful energy generation. A TEG operates on the Seebeck effect, which is a phenomenon in which a temperature difference between two dissimilar electrical conductors or semiconductors produces a voltage difference between the two materials. A commercially available power generation module from Custom-Thermoelectric®(1261G-7L31-04CQ) was used as the TEG. The overall size of the TEG was 40 mm in length by 40 mm in width. This TEG size helped determine the particular surface area of the actual collector plates studied. The back (cold) side of the TEG was coupled to the heat sink to ensure continuous cooling of the cold side, as this ensured heat could be readily rejected by the TEG cold side. The heat sink used was the same as those utilized in previous characterization runs. Thermal grease was applied between the heat sink and the TEG, as well as between the TEG and the absorber plate to minimize thermal resistance between the various components. To further ensure that the device was well clamped together, an acrylic frame was

fabricated and used to clamp the device together using screws. Figure 3.6 shows the device assembly. The schematics of the STC, TEG and heat sink assembly is previously shown in Figure 3.5. Unlike direct collector plate testing, TEG integration testing was conducted in the open environment and not within the acrylic chamber.

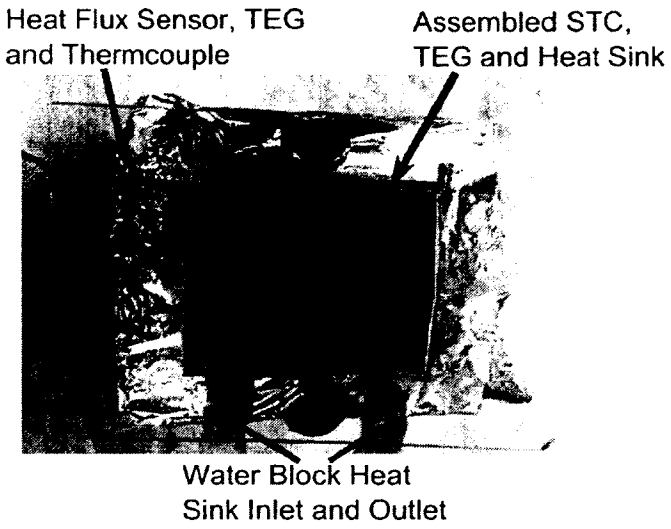

Figure 3.6: Assembled Solar Collector, TEG and Heat Sink

The height of the z-axis laboratory jack was re-adjusted during the TEG test setup. The incident flux was re-validated to verify incident flux at this new height. The radiation flux, Q, to each TEG device was 700 $\frac{W}{m^2}$ of simulated solar radiation over a cross sectional area, A of 0.0016 m^2 (0.04 m $\times$ 0.04 m). Hence, the power, P available as useful input to the device is given by Equation 3.1.

$$P = Q \times A = 700\frac{W}{m^2} \times 0.0016m^2 = 1.12W. \tag{3.1}$$

With the input power set at this value (1.12 W); the performance of the device was evaluated in harnessing this available power. Thermoelectric generators generally operate at very low efficiencies particularly in lower temperatures ranges. First, the

maximum efficiency, η_{max}, expected from the TEG, based on the given material properties and the operating temperature of the device was evaluated. The maximum efficiency expected would be governed by Equation 3.2.

$$\eta_{max} = \frac{T_H - T_C}{T_H} \times \frac{\sqrt{1+ZT}-1}{\sqrt{1+ZT}+\frac{T_H}{T_C}}. \tag{3.2}$$

Where Z is the figure of merit and is given by Equation 3.3.

$$Z = \frac{\sigma \times s^2}{k}. \tag{3.3}$$

Electrical conductivity σ is the inverse of resistivity ρ. For an average temperature T of 300 K (27 °C), typical BiTe material properties indicate Seebeck coefficient, s = 2.01 $\times 10^{-4} \frac{V}{K}$, $\sigma = \frac{1}{\rho} = 1000 \frac{S}{cm}$ and thermal conductivity k = 1.5 $\times 10^{-2} \frac{W}{cmK}$. This resulted in an expected ZT value of 0.808 based on Equation 3.3. Initial experimental observations showed the hot side temperature T_H was 32 °C as the cold sink temperature, T_C, was maintained at 25 °C. Hence, the maximum efficiency expected from Equation 3.2 is given by

$$\eta_{max} = \frac{T_H - T_C}{T_H} \times \frac{\sqrt{1+ZT}-1}{\sqrt{1+ZT}+\frac{T_H}{T_C}} = 0.02872 = 2.87\%. \tag{3.4}$$

Thus, it is expected that the maximum power output from this device given the above mentioned parameters is,

$$P_{max} = 1.12W \times 0.02872 = 32.17mW. \tag{3.5}$$

These expected output values help establish the true operation and capabilities of the solar thermal collectors.

Similar to the initial temperature and flux tests, first a bare polished copper plate was coupled to the TEG and characterized. This provided a baseline data for the TEG test. Voltage output from the TEG was monitored until steady state was achieved. Following the baseline analysis, the device with the thin film selective absorber coating coupled with a TEG was also analyzed. This followed the same procedure as the baseline copper substrate. Each test was carried out several times in order to produce results that were both reliable and repeatable. The TEG module resistance value given in the manufacturer's data sheet was utilized with the measured voltage to calculate the power output.

3.2.3 Experimental Error

The uncertainty associated with the measured and calculated values was determined for this work. Table 3.3 shows the compiled uncertainties. Temperature, heat flux, collector area and voltage were measured parameters and their uncertainties depended on the sensors used. Power input and output were calculated parameters and their uncertainties depended on the measured parameters.

Table 3.3: Measurement and Calculation Uncertainties

Measurement	Error	% of Typical Value
Temperature	± .50 °C	± .515
Heat Flux	± 5.26 $\frac{W}{m^2}$	± .751
Collector Area	± .28 mm^2	± .018
Input Power	± 8.40 mW	± .750
TEG Output Voltage	± .50 mV	± .387
TEG Resistance	± 1.00 mΩ	± .055
TEG Output Power	± .07 mW	± .780

3.3 Results and Discussion

In this section, results of both material and thermal collector characterization are presented. These results represent those of the final black selective absorber coating utilized in these experiment. To fully characterize and document the collectors fabricated in this work, initial tests were conducted to establish coating types and compositions as described in Section 3.2.2. The SEM images of the selective absorber coating, shown in Figure 3.7, indicated that the coating has a dendrite structure. As the structure grows outwards from the substrate, it forms multiple branching dendrites. The average diameter of the small dendrite crystals was observed to be about 100 nm while that of the bigger crystals formed by agglomeration of the smaller crystals measured about 750 nm. EDX analysis was also carried out to determine the atomic composition of the selective coating. This is as shown in Figure 3.8. The result showed that the coating contained on the order of 27 at. % Sn and 73 at. % Ni.

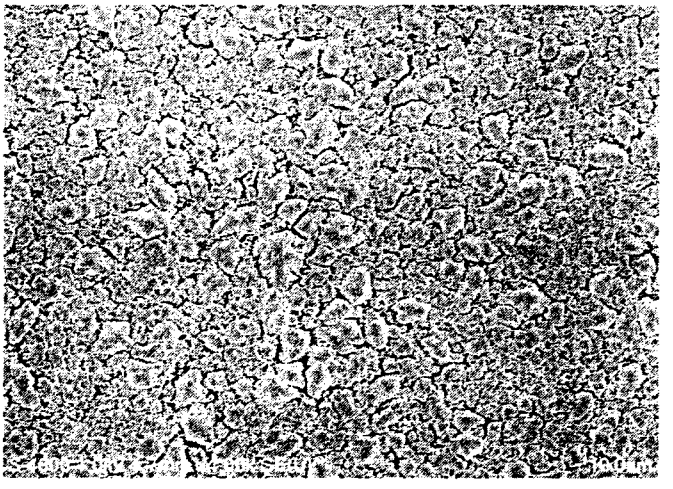

Figure 3.7: SEM Image of Ni-Sn Selective Absorber at 4000X

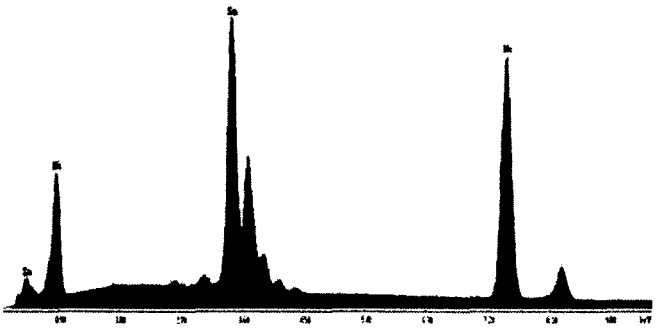

Figure 3.8: EDX Analysis of Ni-Sn Selective Coating

Following the investigation of STC composition, the device was characterized to determine the thermal effectiveness of the coating on the substrate. The heating effect was characterized by temperature as well as heat flux density harvested by each collector. First the baseline copper substrate was tested without heat sink while temperature of the acrylic chamber was also monitored. This established that collector heating resulted from direct radiation heating rather than greenhouse effect within the chamber. Figure 3.9 confirms this mode of operation as demonstrated by the significant difference between the temperature profile of the collector plates and that of the chamber. The temperature profile showed that the copper plate had a stagnation temperature of 87 °C while the chamber temperature stagnated at 62 °C. Following the baseline characterization, the selective surface was tested to characterize the effect of the coating on the thermal absorption of the substrate. The results showed an increased slope of the temperature profile. The stagnation temperature of the Ni-Sn selective absorber was 97 °C, representing an increase of 10 °C. Although

the temperature was increased, more significant results were achieved via heat flux measurement.

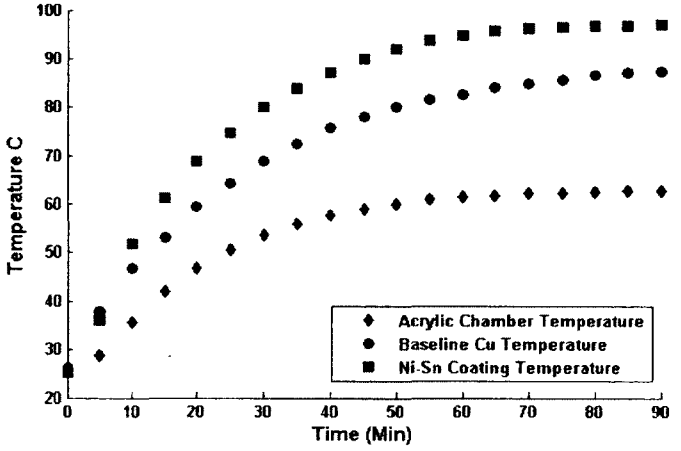

Figure 3.9: Temperature Profiles of Collector Plates and Setup Container

The heat flux density absorbed and conducted through the collector plates to the constant temperature heat sink is presented in Figure 3.10. The useful heat flux output demonstrated the full ability of the collector in harvesting incident radiation. The ratio of the incident flux, representing energy input, and the output flux from the collector characterized the efficiency of the STC. As noted in Section 3.2.2, 880 $\frac{W}{m^2}$ of heat flux reached the collector plates. However, only 580 $\frac{W}{m^2}$ (65.91 %) of this heat flux was absorbed and conducted through the bare copper collector. These values represented baseline data. By contrast, the flux absorbed and conducted through the selective absorber plate showed an average of 800 $\frac{W}{m^2}$, representing 90.90 % of the incident flux. This was about 25 % improvement over the baseline collector. Hence, the use of selective absorber coating significantly improved the ability of the solar collector substrate to harness the heat of the incoming radiation.

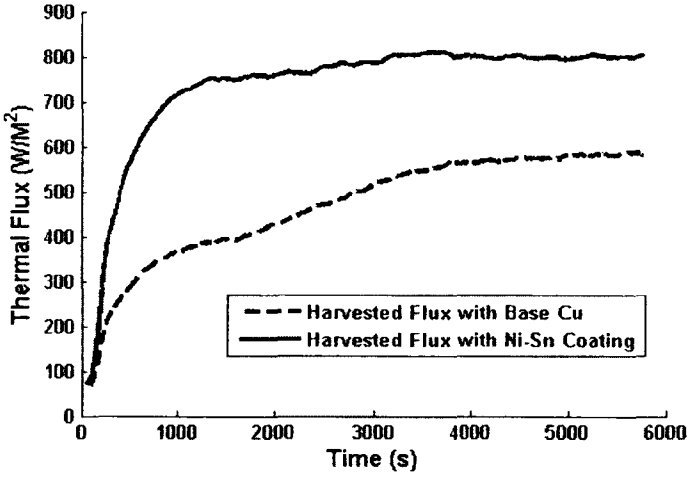

Figure 3.10: Heat Flux Harvested by Different Collectors

Finally, the collector was integrated with a commercially available TEG as a demonstration of harvesting ability. The collectors utilized in these tests had no top cover. Because of this, convection losses from the collector plate itself reduced the total output from the system. In addition, tests conducted with the large heat sink coupled to the TEG reduced the overall operating temperature. The cold side temperature, T_C, of the TEG was maintained at 25 °C while the maximum temperature obtained at the hot side, T_H, was 32 °C. The significant drop in hot side temperature resulted from convection losses from the collector plate as well as the large thermal flux pulled across the device by the heat sink.

The voltage output from the TEG assembly was monitored over time until steady state was reached. The result showed the output voltage from the bare copper collector assembly stagnated at 0.06 volt. Following the baseline characterization, the device with a selective surface collector was tested. The result revealed a faster rise in

the slope of the voltage profile signifying increased heat absorption and heating of the TEG. The output voltage stagnated at 0.129 volt. This was significantly higher than baseline values and showed the potential of the selective coating in use. The results are shown in Figure 3.11.

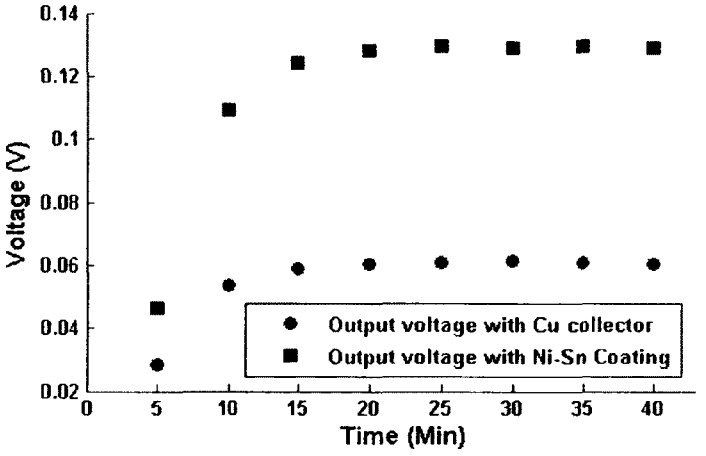

Figure 3.11: Voltage Output from TEG Assembly with Different Solar Collector Plates

To verify the output power of the device, the TEG resistance value was interpolated from the manufacturer data sheet. At an average temperature of 28.5 °C, the resistance, R, was 1.833 ohms. The output power was calculated as $P = \frac{V^2}{R}$. The graph of the power output over time is shown in Figure 3.12. The output from the TEG using the tin-nickel collector plate was 9.1 mW versus only 2 mW when operated with the bare copper baseline setup. These results indicated an increase in power output of 4.5 times through the use of the collector with a selective absorber coating.

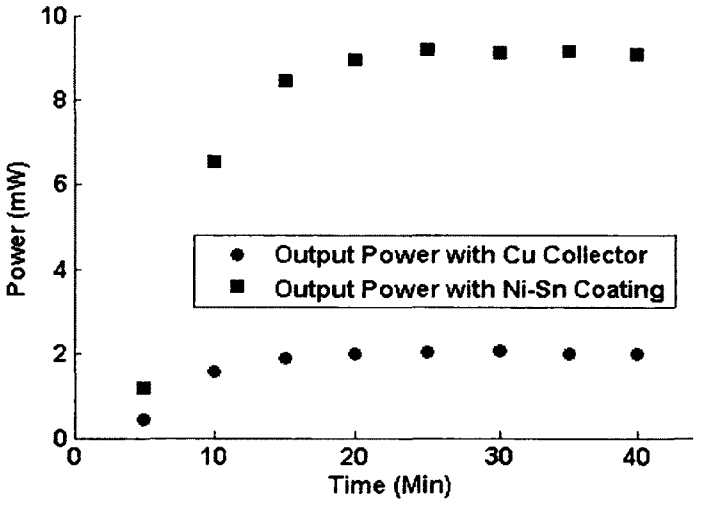

Figure 3.12: Power Output from TEG Assembly with Different Solar Collector Plates

Further, the useful power output demonstrated the ability of the collectors in harvesting solar radiation. The maximum theoretical power expected from the TEG (32.17 mW) was compared to the experimental results. The ratio of the expected power and the actual output power characterized the efficiency of the device, operating from solar thermal energy as input. For the baseline collector plate, the output power was 2.01 mW, representing efficiency of 6.24 %. By contrast, the device with selective absorber plate showed an average of 9.15 mW of harvested power, representing 28.44 % of theoretical maximum.

3.4 Conclusion

Initial fabrication and characterization steps performed in this study showed the potential and capability of a thin film Ni-Sn selective absorber coating for small-scale solar thermal energy harvesting. In final application this device will provide needed thermal energy to MEMS-based devices like thermoelectric generators, micro

steam engines, and other systems requiring thermal input for operation. This thermal collector was fabricated on copper substrate by the chemical electrodeposition technique of a black nickel-tin layer. Characterization of the coating indicated that it was comprised of dendrite crystal structure with average crystal size of 100 nm. The coating contained approximately 27 at. % Sn and 73 at. % Ni.

Thermal and heat flux absorption testing indicated that the coating significantly improved the ability of the collector to transform incident solar radiation into thermal energy. The solar collector utilizing the selective coating achieved a final temperature 10 °C higher than the copper baseline device. In addition, the use of nickel-tin selective absorber coating demonstrated the ability to collect and transmit over 90 % of the available heat flux.

The integration of this small scale solar thermal collector with a TEG for useful power generation has also been demonstrated. In this experiment, the calculated maximum theoretical power expected from the TEG was compared to the experimental results. The ratio of the expected power and the actual output power characterized the efficiency of this device. Given a collector plate without selective coating, the output power was 6.24 % of theoretical maximum. By contrast, the device utilized with selective absorber achieved 28.44 % of theoretical maximum. The use of selective absorber coating significantly improved the ability of the solar collector substrate to harness the heat of the incoming radiation. This demonstrated the ability of the collector plate to provide thermal energy to devices like TEGs for deployment in real-world applications.

Further work is underway to enhance the operating temperature of the device by reducing convection losses from the collector plate through the use of cover glass. Given higher operating temperature, the power output from the device will be increased. Continuing work is also underway to scale up the design for use with larger collector surface areas. In this manner, more solar radiation can be harnessed and utilized in generating useful power output. This will dramatically increase output from attached devices.

CHAPTER 4

PERFORMANCE OF FLAT PLATE COLLECTORS IN LOW THERMAL CONDUCTIVITY ENVIRONMENT

4.1 Introduction

Thermal losses from heat engines limit the system overall efficiency. In solar thermal systems, maximizing absorption while limiting losses due to convection and radiation losses is critical in achieving high temperature values. While selective absorber coating is used to enhance absorption and limit re-radiation losses, thermal insulation helps to reduce convection and conduction losses from the collector plate. This chapter examines thermal insulation in solar thermal applications.

Many types of insulation are available in the market. The basic consideration in selecting any particular insulation material is to reduce the flow of heat from one point to the other. Specific parameters such as thermal conductivity, operating temperature, combustibility, chemical stability, mechanical strength and durability, and cost are also considered in the material selection process.

The thermal conductivity of traditional thermal insulation materials like mineral wool, expanded polystyrene (EPS) and extruded polystyrene (XPS) is in the range of 0.033 $\frac{W}{m.K}$ to 0.040 $\frac{W}{m.K}$, while polyurethane (PUR) have thermal conductivity ranging from 0.020 $\frac{W}{m.K}$ to 0.030 $\frac{W}{m.K}$ [52, 53, 54]. To achieve very low thermal transmittance,

U-value, (rate of heat transfer, in watts, across one square meter area divided by the temperature gradient across the surface), high insulation thickness in the range of 40 cm to 50 cm is required [54]. Hence, space and weight constraints limit the application of these materials. More so, these materials are not transparent to solar radiation and therefore do not readily find application in solar thermal collectors.

Another growing insulation material is aerogel. One advantage of this material is its light weight (about 90 % porosity). Further, silica aerogel granulate nanostructured material has been reported to have high solar transmittance and low thermal conductivity, and are commercially available with thermal conductivity as low as 0.012 $\frac{W}{m.K}$ and thickness in the mm range [55, 56, 57]. For a required thermal performance, aerogel exhibits a reduced thickness compared to traditional insulation. Hence, silica aerogel has a promising potential in solar thermal applications. However, the cost of aerogel insulation at this time is still relatively high.

Other techniques being actively explored for flat plate solar thermal applications include vacuum insulation panels [58] and gas-filled panels [59]. In vacuum insulation, the volume between the absorber plate and the cover glass is evacuated thereby limiting convection and conduction losses. The concept of vacuum insulation was invented in 1892 by Sir James Dewar. The Dewar flask consisted of two flasks, one placed within the other and joined at the neck, with the gap between the two flasks partially evacuated of air. Conduction and convection heat transfer is eliminated by the near-vacuum environment. In reality, a perfect vacuum is never achieved. However, low pressure environment positively influences gas conductivity. This technique is also used in glass window panels. The work contained in this chapter seeks to integrate

vacuum insulation technology with flat plate solar thermal collector so as to reduce energy losses from the plate to a minimum.

In the absence of sufficient vacuum capabilities, the volume between the collector and the cover glass may also be filled a low thermal conductivity gas such as argon (Ar), krypton (Kr), and Xenon (Xe). This way the gas-filled panel enhances insulation qualities as gas conductivity is lowered. In both vacuum insulation and gas-filled panel, hermetic sealing is critical. For micro scale applications, there are many established vacuum packaging/encapsulation techniques with airtight seals [60]. The effect of low pressure environment on the thermal performance of a solar thermal collector plate is presented in this chapter.

4.2 Experimental and Numerical Methods

This section describes numerical and experimental investigations conducted to thermally characterize the performance of solar collector plates in low thermally conductive environments. The fabrication and testing of a solar selective absorber coating in atmospheric pressure conditions have previously been reported in Chapter 3. Fabrication of the collectors tested as part of this current effort followed the same procedure as that described in Section 3.2.1.

4.2.1 Theoretical Model and Numerical Analysis

4.2.1.1 Temperature variation in evacuated spaces

In an enclosed volume, such as flat plate collectors, the pressure (density) of the gas between the plate and cover glass may be sufficiently lowered so that free-convection flow velocities are very small. This way, the only form of heat transfer

between the gas molecules is by conduction. The kinetic theory of gases describes a gas as molecules in continuous random motion, colliding with one another and with the walls of the container. The collisions result in exchange of energy and momentum. That is, when a molecule moves from a high-temperature region to a lower temperature region, it carries with it kinetic energy to the lower-temperature region. The kinetic energy is exchanged with the lower energy molecules through collision. The average distance a molecule travels between collisions is described by the mean free path λ, and can be calculated using Equation 4.1 [61].

$$\lambda = \frac{1}{n\sqrt{2}\pi d^2}. \tag{4.1}$$

Where n is the gas number density and d is the average diameter (in meters) of the gas molecules.

From kinetic theory of gases, the pressure (in Pascals) and number density of a gas molecule are related as shown in Equation 4.2 [61].

$$P = nkT. \tag{4.2}$$

Where K is the Boltzmann constant (1.38×10^{-23} JK^{-1}) and T is the gas temperature in Kelvin (K). Applying Equation 4.2 into Equation 4.1, the mean free path can be obtained by Equation 4.3

$$\lambda = \frac{KT}{P\sqrt{2}\pi d^2}. \tag{4.3}$$

The average diameter, d, of air (3.16×10^{-10} m) is obtained by a weighted average (79:21) of the molecular diameters of nitrogen (3.2×10^{-10} m) and oxygen (3.0×10^{-10} m). An approximate mean free path Equation for the air molecules is therefore

given by Equations 4.4 and 4.5. When gases other than air are utilized, the diameter of the gas molecule is used accordingly to determine the mean free path. In all cases however, the mean free path increases (and hence less energy transfer) as the pressure is lowered, assuming steady state temperature conditions.

$$\lambda(\mathrm{m}) = 3.11 \times 10^{-5} \frac{T}{P_{Pa}} \tag{4.4}$$

$$= 2.33 \times 10^{-7} \frac{T}{P_{Torr}}. \tag{4.5}$$

With an increase in λ, resulting from lowering the pressure of the system, the average distance required for energy exchange between the high-temperature and lower-temperature regions increases. In a flat plate collector, when λ is large, the hot collector plate and the gas molecules in contact or in the immediate neighborhood of the plate will have different temperature values. In this case, the temperature distribution is governed by the molecular activities.

Heat transfer by molecular flow is different from boundary-layer (continuum flow) regime where the temperature of the hot plate and the gas in contact with it is assumed to have same temperature values. In the continuum regime, the pressure is near atmospheric and so the mean free path is very small. Hence, heat energy is more easily transferred by collision of molecules. The Nusselt number is usually used in correlating heat transfer in the boundary layer regime [62, 63].

A transition regime exits in which heat transfer is not exactly governed by molecular flow nor by continuum flow. This intermediate regime is further classified into slip and transition regimes [64, 65]. Knudsen number (Kn), a ratio of the mean free path of the gas molecules to the characteristic length L of the device, describes the

various regimes. Kn is calculated using Equation 4.6 [27]. The characteristic length of the collector plate L, is defined here as the ratio of plate area to its perimeter. This and the average temperature T_e of the plate was used to verify the flow regimes and pressure ranges based on the Knudsen number. This is as shown in Table 4.1.

$$Kn = \frac{\lambda}{L}. \tag{4.6}$$

Table 4.1: Flow Regimes Versus Knudsen Number

Knudsen number	**Pressure (Torr)**	**Flow regime**
Kn <0.001	P>9	Continuum flow
0.001 < Kn < 0.1	0.09<P<9	Slip flow
0.1 < Kn < 10	0.0009<P<0.09	Transitional flow
10 < Kn	P<0.0009	Molecular flow

As the pressure is lowered, natural convection within the enclosure is also lowered. The main source of heat transfer therefore becomes conduction (by gas molecules) and radiation. At a sufficiently low pressure (the molecular flow regime), natural convection is completely eliminated.

The thermal conductivity of gas varies with temperature and pressure. Kaminski [66] presented a correlation for the pressure (Pa) and temperature (K) dependence of thermal conductivity as shown in Equation 4.7

$$k_e = \frac{k_o}{1 + 7.657 \times 10^{-5} \frac{T}{Pd}}. \tag{4.7}$$

Where k_o and k_e are thermal conductivities of air at atmospheric and reduced pressure conditions respectively. d is the distance between the plates. Overall, k_e decreases with decrease in pressure until the heat conduction is completely eliminated irrespective of

operation temperature. The pressure dependence of air thermal conductivity is shown in Figure 4.1 for different temperatures.

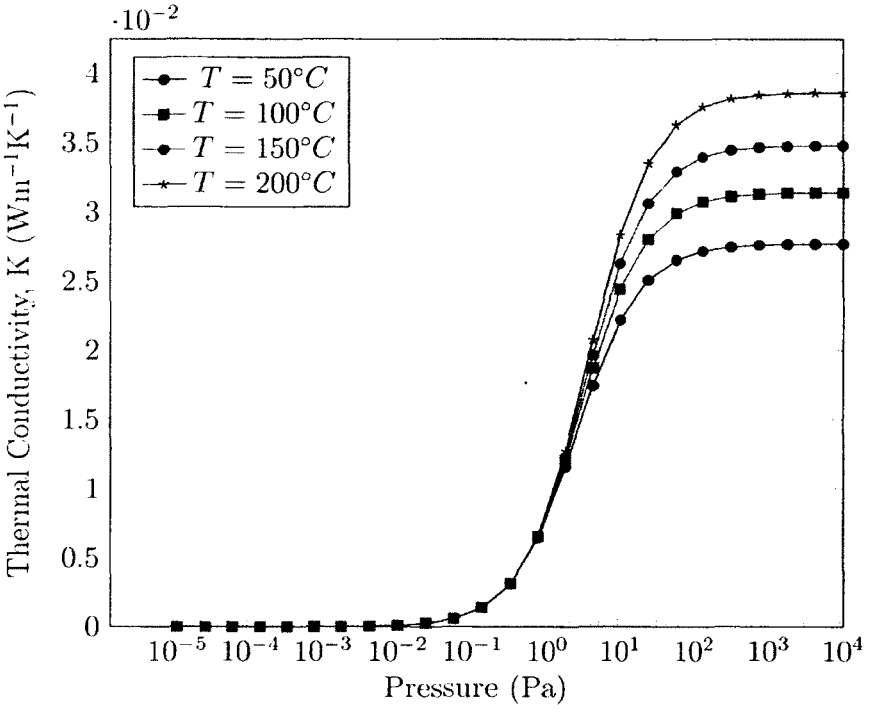

Figure 4.1: Pressure Versus Thermal Conductivity of air at Different Temperatures

4.2.1.2 Collector plate energy balance

The useful energy harvested by a solar collector is determined by the ability of the surface to absorb incident radiation as well as the capacity of the body to limit long wavelength radiation from the surface. Further, the convection losses from the collector plate to the ambient air limits the overall useful energy gain. Equation 4.8 shows the available useful energy, $\dot{Q}_u$ harvested by a solar thermal collector plate [67].

$$\dot{Q}_u = q_u A_c = (\tau\alpha) q_s A_c - \bar{U} A_e (\bar{T}_e - T_a) - \epsilon\sigma A_e (\bar{T}_e{}^4 - T_a^4). \qquad (4.8)$$

[useful energy harvested] = [energy absorbed]-[convection losses]-[radiation losses].

As can be seen from Equation 4.8, the energy absorbed depends on the transmissivity-absorptivity product ($\tau\alpha$), the area of the collector A_c and the incident solar radiation intensity q_s. The radiation loss from the surface of the collector plate is directly proportional to the emissivity ϵ of the surface. Further, since the sides of the collector as well as the top and bottom surfaces are subject to convection and conduction losses, the overall heat transfer coefficient $\bar{U}$ is critical in the amount of losses from the plate. These critical parameters are analyzed next.

4.2.1.3 Steady-state temperature

The temperature of the absorber element rises as radiation is absorbed. Hence, the temperature varies with time. However, to simplify this analysis, a steady-state (thermal equilibrium) condition is assumed. Hence, this section presents the steady-state temperature conditions for a solar collector element.

At thermal equilibrium, the energy absorbed by the collector is equal to that lost from the surface such that there is no net energy gain as shown in Equation 4.9. If the cover glass is highly transmissive such that $\tau_g \sim 1$, then the absorbed energy is dependent on the solar absorptivity α_s of the surface while the amount of losses from the collector is related to the emittance ϵ and the heat loss coefficient $\bar{U}$ [67].

$$0 = \alpha_s q_s A_c - \bar{U} A_c(\bar{T}_e - T_a) - \epsilon\sigma A_e(\bar{T}_e^{\,4} - T_a^4). \tag{4.9}$$

$$\alpha_s q_s A_c = \bar{U} A_c(\bar{T}_e - T_a) + \epsilon\sigma A_e(\bar{T}_e^{\,4} - T_a^4). \tag{4.10}$$

The ability to achieve high temperature values is critical for a system that relies on thermal energy as input. The goal here is to design a system that maximizes temperature gain from the sun's heat energy. Typically, in a flat plate solar collector

there are no optical concentrating devices. The area of the collector A_c is equal to the area of the absorber element of the collector A_e. This reduces Equation 4.10 to Equation 4.11.

$$\alpha_s q_s = \bar{U}(\bar{T}_e - T_a) + \epsilon\sigma(\bar{T}_e^{\,4} - T_a^4). \tag{4.11}$$

4.2.1.4 Negligible heat loss coefficient

If the collector's overall heat loss coefficient is negligible (that is $\bar{U}$ =0) such that there are no convection or conduction losses from the plate, then the stagnation temperature of the collector (from Equation 4.11) can be re-written as Equation 4.12. It has been demonstrated that vacuum packaging at a pressure of 10 mtorr (~1.3 Pa) or below is sufficient to completely eliminate conductive and convective heat losses [68].

$$\bar{T}_e = \sqrt[4]{T_a^4 + \frac{\alpha_s q_s}{\epsilon\sigma}}. \tag{4.12}$$

Figure 4.2 shows the achievable temperatures under different α_s and ϵ values. It can be seen that a flat plate collector will achieve a stagnation temperature above 300 °C if the infrared emissivity is kept below 0.132 and there are no conduction and convection losses from the plate. Lower values of infrared emissivity will be required depending on the value of the collector absorptivity. A detailed review of absorber coating materials yielding varying absorptivity and emissivity values is given in Ref [21]. Many of these coating materials are also commercially available.

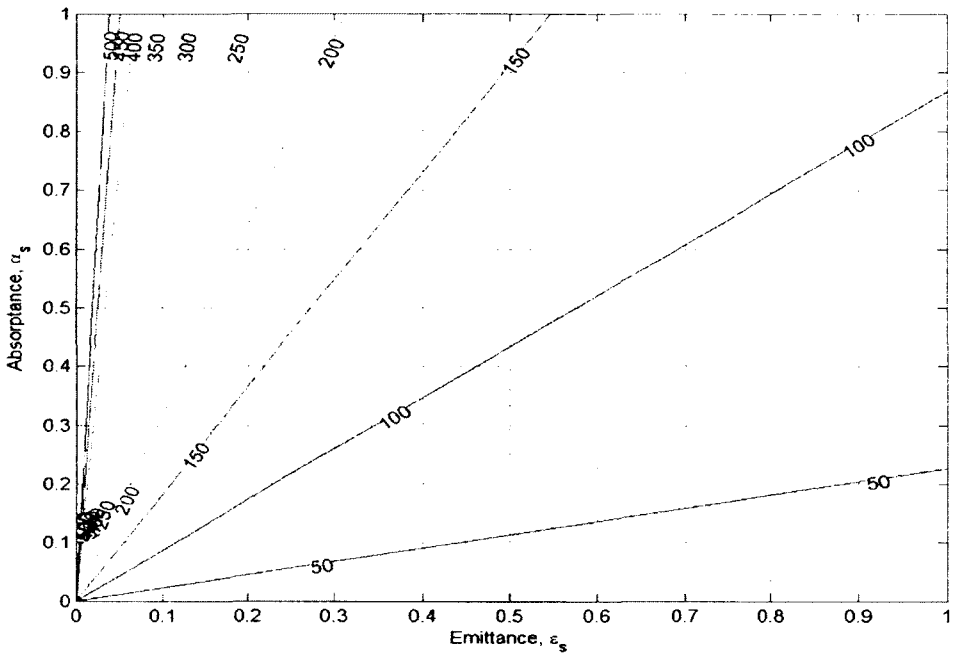

Figure 4.2: Steady-state temperature contour plot of a surface exposed to 750 $\frac{W}{m^2}$ and ambient temperature T_a of 25 °C, based on absorptivity and emissivity of the surface

In this work, nickel-tin (Ni-Sn) coating has been selected as the collector absorber material. Previous work has indicated black Ni-Sn selective coating has promising potential as a highly effective selective absorber structure with absorptivity α_s of 0.98 and emissivity ϵ of 0.10 [46].

4.2.1.5 Heat loss coefficient effect

In real world applications however, the amount of heat absorbed by the collector is lowered by thermal losses from the collector. Again, if steady state condition is assumed, the net useful heat gain absorbed by the collector is zero. Equation 4.11 is used to evaluate the effect of heat loss coefficient $\bar{U}$ on the steady state temperature

of the absorber element T_e. This assumes known values of incident radiation, solar absorptivity α_s, emissivity ϵ, and ambient temperature T_a.

The overall heat loss coefficient $\bar{U}$ is a function of various parameters. These include the temperature of the absorber plate, glass cover and ambient temperature, emissivity of absorber (ϵ_e) and glass cover (ϵ_g), number of glass cover plates (N), air gap distance, plate tilt angle ,β, thermal conductivity of insulation material (k) and its thickness (x), convective heat transfer coefficient (h_a), etc. The total heat loss coefficient $\bar{U}$ from the absorber surface to the ambient is the sum of the top loss coefficient $\bar{U}_{top}$, edge loss coefficient $\bar{U}_{edge}$ and the back loss coefficient $\bar{U}_{back}$, as shown in Equation 4.13.

$$\bar{U} = \bar{U}_{top} + \bar{U}_{back} + \bar{U}_{edge}. \tag{4.13}$$

An equation for $\bar{U}_{top}$, developed by Klein [69] and modified by Duffie and Beckman [8] is presented in Equation 4.14. This is used to approximate the thermal loss coefficient to the ambient environment. The ambient wind loss coefficient h_a, and the temperature gradient between the glass cover and the ambient influences the top loss heat transfer coefficient.

$$\bar{U}_{top} = \left[\frac{N}{\frac{C}{T_e}\left[\frac{T_e - T_a}{N+f}\right]^e} + \frac{1}{h_a}\right]^{-1} + \left[\frac{\sigma(T_e + T_a)(T_e^2 + T_a^2)}{(\epsilon_e + 0.00591Nh_a)^{-1} + \frac{2N+f-1+0.13\epsilon_e}{\epsilon_g} - N}\right] \tag{4.14}$$

where

$$C = 520(1 - 0.000051,\beta^2)$$

$$f = (1 + 0.089h_a - 0.1166h_a\epsilon_e)(1 + 0.07866N)$$

$$e = 0.43(1 - \frac{100}{T_e}).$$

Further, the back-loss and edge-loss coefficients can be solved using Equations 4.15 and 4.16 [19].

$$\bar{U}_{back} = \frac{k_b}{x_b}. \tag{4.15}$$

$$\bar{U}_{edge} = \frac{k_e}{x_e}\left(\frac{(L+W)H}{LW}\right). \tag{4.16}$$

where L x W is the area of the absorber and H is the height of the collector casing.

Buchberg et al [70] have suggested the following correlation for solving the natural convection heat transfer coefficient in the enclosed space between the absorber plate and glass cover.

$$h = \frac{Nu.k}{L}. \tag{4.17}$$

where Nu is the Nusselt number, k is the thermal conductivity of air and L is the air gap. Nu may be calculated using Equation 4.18 [71].

$$Nu = 1 + 1.44\left[1 - \frac{1708}{\cos\beta.Ra}\right]\left[1 - \frac{\sin(1.8\beta)^{1.6}.1708}{\cos\beta.Ra}\right] + \left[\left(\frac{\cos\beta.Ra}{5830}\right)^{1/3} - 1\right] \tag{4.18}$$

where Ra is the Rayleigh number (a product of the Grashof and Prandtl numbers) given by Equation 4.19.

$$Ra = Gr \times Pr = \frac{g\beta(\Delta T)d^3}{\nu^2} \times Pr. \tag{4.19}$$

4.2.2 Test Setup and Procedure

This section describes tests conducted to thermally characterize the performance of these collector plates in low thermally conductive environment. Two tests were conducted. The first was conducted under atmospheric conditions similar to that reported in Chapter 3 and formed the baseline data for this work. The second test was

conducted under an evacuated environmental condition. Lower pressure conditions as shown in Section 4.2.1.1 limits heat losses. The effect of pressure variation on temperature was experimentally studied. Both tests were conducted with the collector plate set up in an enclosed chamber. This further helped to limit convection losses from the ambient.

A halogen lamp was used to simulate solar radiation in this experiment. The simulator lamp used was the Sun System®SS-2 MH 400W lamp. All tests were conducted by exposing the collector plate to incident radiation from the lamp. Like the sun, the intensity of the radiation from the lamp varied with distance. As the distance from the lamp increased, the intensity of output decreased. A Hukseflux®SR11 pyranometer was used to validate the intensity of the radiation at various distances from the simulator lamp. This information was used to select an appropriate distance from the lamp which simulated flux density closely approximating real world availability. A z-axis laboratory jack was used in adjusting the height of the test setup from the lamp.

An intensity of approximately 796 $\frac{W}{m^2}$ was selected. The pyranometer was used to determine the required distance from the simulator lamp. The experiment was placed in a vacuum chamber to minimize heat losses during experimentation. The vacuum chamber was made of aluminum 6061 tube and borosilicate glass window. More detailed construction diagrams for the chamber is included in appendix A. The transmissivity of the chamber glass cover was verified by passing the simulated solar radiation through the lid and measuring its flux density via Pyranometer. The result

showed that the glass had a transmissivity of 0.98. This amounted to a radiation intensity of approximately 780 $\frac{W}{m^2}$ reaching sample surfaces inside the chamber.

A fiberglass material (Garolite G-7 from McMaster-Carr®) was used as a frame to support the collector plate at the center of the chamber. The frame was suspended as shown in Figure 4.3 using 36 SWG (standard wire gauge) nichrome wires. Garolite G-7 was selected due to its very low thermal conductivity (on the order of 0.3 $\frac{W}{m.K}$) and high mechanical strength. The low thermal conductivity helped to limit thermal conduction from the collector during operation while the mechanical strength ensured stable support for the collector plate. The nichrome wires were epoxied to the chamber wall. This created a suspended base for the collectors. Each collector was placed on the fiberglass base such that the collectors did not extend to the nichrome wires. This way, heat loss through conduction from the collector plate was only through the fiberglass.

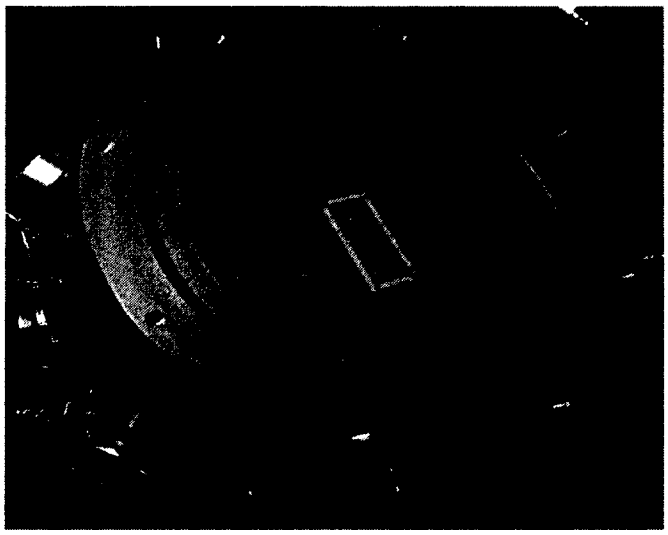

Figure 4.3: Vacuum Chamber with Suspended Fiberglass Frame for Collector Plate Mounting

The temperature of the collector plate and chamber environment when exposed to incident radiation were monitored using thermocouples, TCs (SA1-k-120 from Omega®Engineering). The first TC was placed on the back side of the collector plate. This monitored the plate temperature during operation. The second TC was suspended within the chamber to directly monitor the temperature within the chamber. A thermocouple feedthrough (TFT3KY00008B from Lesker®, USA) was used to fit the TCs through the chamber wall. This was useful in maintaining the isolated environment. National Instruments LabVIEW®(using cDAQ-9174 data logger) was used to record all TCs data to a computer for analysis. Figure 4.4 shows the vacuum chamber setup with mounted collector plate ready for testing.

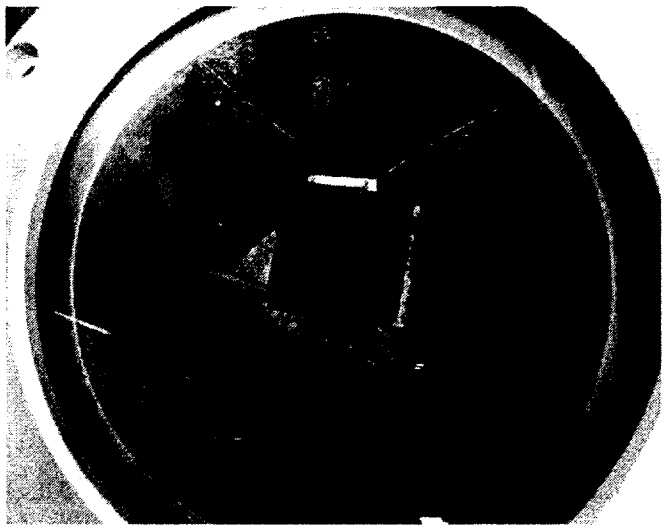

Figure 4.4: Collector Plate Mounted in a Vacuum Chamber Ready for Testing

A vacuum pump (Alcatel®SD 1015) was used to evacuate the chamber for the low pressure tests. The pressure of the chamber was monitored using a convection

pressure gauge (KJL275807 from Lesker®, USA). In all the tests, temperatures were monitored until steady state conditions were reached.

4.3 Results and Discussion

4.3.1 Numerical Results

First, results from the numerical analysis is presented. It has been noted that the overall heat loss coefficient lowers the average collector plate temperature. Figure 4.5 shows this relationship between $\bar{U}$ and T_e. Actual absorptivity α_s determined from Chapter 3 was used for this analysis. This plot assumes an incident radiation of 750 $\frac{W}{m^2}$, absorptivity α 0.91 and emissivity ϵ 0.1.

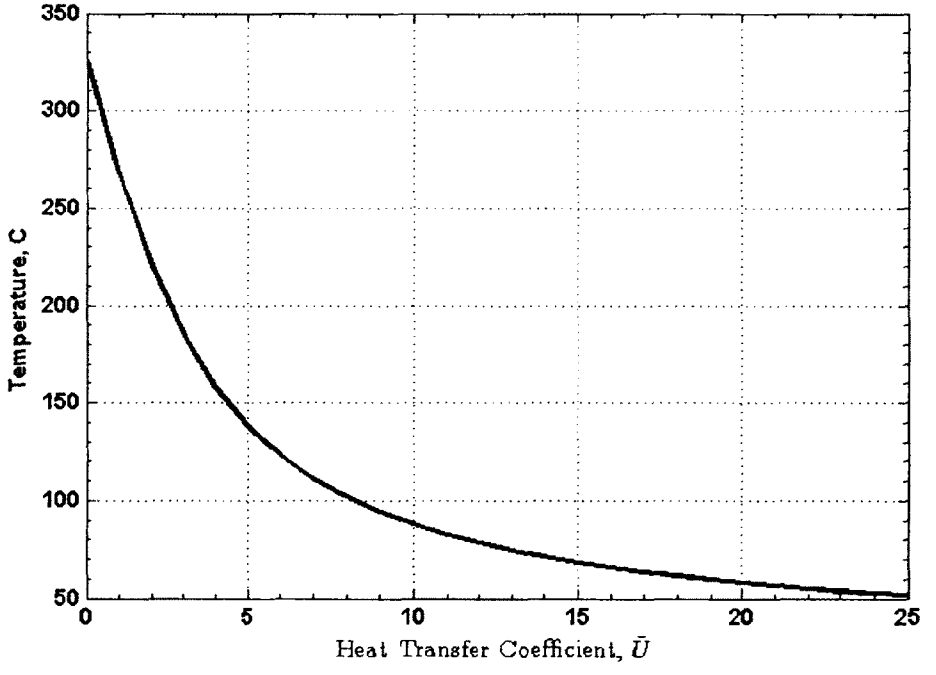

Figure 4.5: Effect of overall heat transfer coefficient $\bar{U}$ on the steady-state temperature of a surface exposed to 750 $\frac{W}{m^2}$ and T_a of 25 °C, based on $\alpha = 0.91$ and $\epsilon = 0.1$

It can be seen from Figure 4.5 that as the heat loss coefficient increases there is a significant decrease in the absorber plate temperature. Hence, adequate thermal insulation must be utilized to limit heat losses from the plate.

Further, the overall heat loss coefficient and other parameters were estimated based on the formulations of Section 4.2.1. The range of variables as determined are listed in Table 4.2. The values obtained were compared to results of experimental tests.

Table 4.2: Solar Collector Specification Variables

Variable	Range
Ambient temperature, T_a	298 K
Absorber plate temperature, T_c	363-388 K
Absorber plate emittance ϵ_c	0.1
Glass cover emittance, ϵ_g	0.90
Collector tilt angle, β	0 °
Collector length, L	0.04 m
Collector width, W	0.04 m
Number of cover, N	1
Insulation material	Vacuum
Wind heat transfer coefficient h_a	1-10 $W.m^{-2}K^{-1}$
Top loss coefficient U_{top}	1.68-4.40 $W.m^{-2}K^{-1}$
Total loss coefficient $\bar{U}$	3.10-7.86 $W.m^{-2}K^{-1}$

4.3.2 Experimental Results

This section presents results of experimental tests conducted to validate the numerical analysis. Temperature of the collector plates were monitored when exposed to radiation flux. Two tests were conducted. The first recorded the temperature of the plate under atmospheric conditions while the second test was conducted under an evacuated volume. In both cases, the temperature of the plates and the vacuum chamber were monitored until steady state conditions were achieved.

Figure 4.6 shows the collector temperature plot for the atmospheric and partial vacuum conditions. The temperature profile showed that the plate had a stagnation temperature of 96 °C under atmospheric conditions. This is similar to the result reported in Chapter 3. Following the atmospheric condition tests, the collector plate was also tested to characterize the effect of the low pressure condition on the thermal performance of the plate. The result showed an increased slope of the temperature profile. The stagnation temperature of the plate was 115 °C, representing an increase of 19 °C. For the evacuated tests, the pressure of the chamber was lowered to 715 mTorr (from 760 Torr) and held constant at this point throughout each test. The chamber interior temperature was also monitored in each test. In both cases, the chamber temperature stagnated at about 58 °C. This is much lower than the temperature of the plate for each test confirming that the plates were heated directly by thermal radiation and not by greenhouse effect within the chamber.

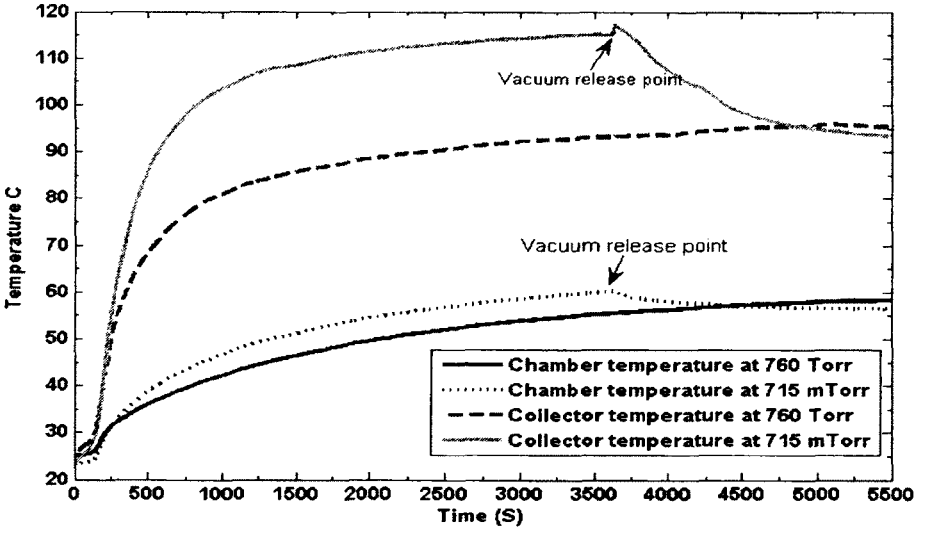

Figure 4.6: Collector Plates and Vacuum Chamber Temperatures

To further confirm the temperature gain recorded under partial vacuum condition was primarily due to the space evacuation. air molecules were re-introduced into the chamber after steady state conditions were reached. The vacuum release points are as shown in Figure 4.6. As the chamber pressure rose, the temperature of the plate reduced. Interestingly, as the chamber pressure increased back to 760 Torr, the temperature of the collector again matched the temperature obtained previously under atmospheric condition tests. Similar result was also noted for the chamber temperature. The reduction in collector temperature was caused by energy losses occasioned by the presence of air molecules within the chamber. These results agree with numerical results which predicted an increase in collector temperature with a decrease in chamber pressure.

4.4 Conclusions

The use of vacuum environment to limit the thermal losses from a collector plate has been presented. Tests were conducted to verify the operation temperature of collector plates when exposed to simulated solar radiation. Results showed an improvement in the stagnation temperature of the collector plate when operated in a partial vacuum environment (715 mTorr) compared to results obtained under atmospheric pressure (760 Torr). The temperature of the plate increased from 96 °C to 115 °C (an increase of 19 °C) by lowering the pressure of operation environment.

Further work will examine the temperature of the plate under higher vacuum conditions. Also, effort is underway to examine the effect of other operation environments with low thermal conductivity gases like argon, xenon and krypton.

This way, rather than maintaining a vacuum environment, other gases (with thermal conductivity lower than air) may be utilized to replace air molecules within the operation environment. It is anticipated that this would also limit thermal losses from the collector plate.

CHAPTER 5

MEMS-BASED BOILER FOR THERMAL SCAVENGING APPLICATIONS

5.1 Introduction

The growing need for efficient, sustainable energy is driving research to examine both new sources of energy as well as methods to increase the efficiency of devices and processes that are already in place. The U.S. Department of Energy (DoE) has predicted that the world's energy demand will increase 53 % by 2035 compared to 2008 levels of 505 quadrillion British thermal units (Btu) [72]. This makes advanced energy technologies particularly relevant. Traditional "clean" energy sources such as solar and wind power are rapidly being developed. Other non-traditional techniques aimed at harvesting thermal energy that is otherwise discarded to the environment as a part of a larger process are also being investigated.

In 2010, the United States consumed 98 quadrillion BTUs of energy [73]. The transportation sector alone consumed nearly one third of that total. The challenge however is that a typical Otto Cycle engine has an efficiency that is on the order of 35 % [74]. Hence, the vast majority of unused energy from an automobile engine is released to the environment as low-grade waste heat in the form of radiator heat fluxes or exhaust. These losses to the environment, similar to those of microelectronics as

well as solar thermal radiation, present an unique opportunity to develop solutions that scavenge and turn this "wasted" thermal energy into useful power output.

One method of harvesting thermal energy is through the use of thermoelectric generators (TEGs). These devices serve to convert thermal energy directly to electrical power via the Seebeck effect. Application of TEG in solar energy harvesting is presented in Chapter 3. In addition to TEGs, thermal energy may be used to drive a phase change in a working fluid when integrated with a heat exchanger. MEMs-based heat engines for power generation are being developed that rely on this phase change for useful power output [32, 33, 34, 35, 75].

In this chapter, research on a unique small scale heat exchanger is presented. The micro heat exchanger (MHE) is designed to pair with other devices like thermoelectric generator (TEG) and other traditional small scale heat engines for thermal management application. In TEG applications, energy dissipated from other devices and processes may be efficiently introduced and rejected from the TEG itself via the heat exchanger. This increases thermal cooling effect from such devices and processes, and enhances the performance of the TEG and overall effectiveness of the thermal scavenging. The MHE presented in this work may also be applied in solar thermal power applications where the heat from the solar collector is rejected into the exchanger. This way, absorbed heat from the collector plate may be utilized in the working fluid within the exchanger for useful power generation. In addition, this robust MHE is well suited to application in other MEMS fields. There are numerous applications that include use in micro steam systems as well as many others [76].

Cross-flow air heat exchangers were examined by Crane and Jackson that included a detailed modeling effort [77]. A TEG constructed with Bi_2Te_3 was sourced as the power conversion device in that work. As in larger scale exchanger work, the geometry and materials selection have been noted as critical elements to effective MHE development [78, 79, 80]. Due to space considerations, other research specifically examined the use of micro scale components in applications related to thermal scavenging from water flows [81]. Many of these approaches have consisted of single-phase exchangers. Waste and/or solar thermal energy may be used to drive a phase change in a working fluid when integrated with a heat exchanger. The use of phase change has been less common in the field of thermal scavenging. Nonetheless, the advantages of this approach have been manifested in applications like computer chip cooling [82, 83]. Micro-devices and micro channel design have been of particular interest [83]. Tuckerman and Pease first noted that miniaturizing cooling channel dimensions leads to increased heat transfer efficiency [84]. In CPU application there has also been research in capillary driven exchangers where working fluid phase change is again the primary means of heat transfer [85, 86, 87, 88, 89, 90]. Working fluids have varied, but have typically depended on the temperature ranges of the final applications.

The unique heat exchanger presented in this work relies on multiple rows of capillary channels to promote mass and heat transfer using working fluid with low-temperature boiling point. By design, it is intended for application to small-scale devices in thermal dissipation and energy scavenging work. Figure 5.1 illustrates the basic concept. Thermal energy dissipated as part of a larger process is applied to the

exchanger lower surface which is patterned with capillary channels. The rectangular capillary channels extend between two working fluid reservoirs and continually feed working fluid across the heated surface. This results in phase change of the working fluid and heat transfer away from the thermal source. Similar to waste heat applications, solar thermal energy may be applied to drive this phase change in the working fluid. The design as shown in Figure 5.1 may be inverted when used in solar thermal applications. This way, solar radiation serves as the heat supply to the exchanger.

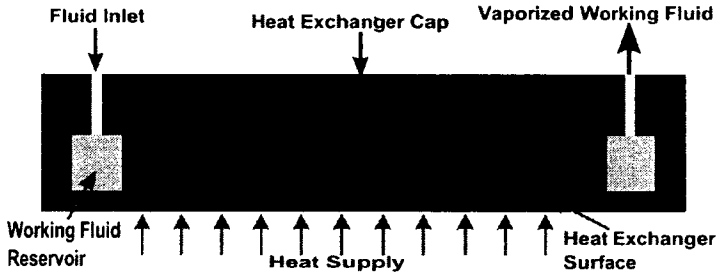

Figure 5.1: MEMS-Based Boiler Configuration

In order to characterize the performance of the device, the thermal energy transferred into the working fluid via the various microchannels is observed. The working fluid mass transfer rate is recorded and this provides an insight into the exchanger ability to harvest thermal energy through the multiple capillary channels. This metric of performance is normalized by the area of the exchanger plate to yield values in $\frac{kW}{m^2}$.

In this work, the working fluid was introduced into the reservoir region using a syringe pump and the vaporized fluid was collected and weighed after each experimental run. This way, the mass transfer rate was fully monitored during the experiments.

Effort was concentrated at direct study of the effect of capillary heights of the microchannel designs with respect to mass transfer and power consumption.

5.2 Experimental Methods

5.2.1 Fabrication

The MHEs described in this worked were produced via microfabrication techniques. The use of microfabrication techniques presents several advantages. First, batch fabrication allows the generation of many devices from singular processing steps [91]. Further, the small scale of the approach allows installations of small, single units as well as larger applications where many devices work from a larger thermal energy source.

Operation of exchangers fabricated with silicon capillary channels and those fabricated using SU-8 material for capillary channel walls have been documented in literature by our group [92, 75]. In these previously reported work, channel widths were maintained at 100 μm. The use of SU-8 allowed an increased range of channel aspect ratios compared to the basic silicon structures. Heat transfer was, however, impeded in the SU-8 channel walls as SU-8 is a non-conductive polymer material. In this present work, channel width was maintained at 300 μm for each exchanger studied. Channel heights were varied to allow study of capillary action and thermal mass on exchanger heat transfer capability. Exchanger heights varying from 110 μm to 200 μm were fabricated and characterized. In all cases, silicon served as the original substrate material. Each exchanger had an overall size of 13 mm in width by 38 mm in length. Overall channel lengths were 25.5 mm, centered on the exchanger between

the reservoirs as noted in Figure 5.1. Specific fabrication techniques and designs are discussed next.

5.2.1.1 Silicon channels

The exchanger device was fabricated based on silicon capillary channel construction techniques. The silicon exchanger fabrication began with a standard 400 μm thick, double-side polished <100> silicon wafer. First, a 150 nm thick layer of aluminum was deposited directly on one side of the silicon wafer. Electron beam deposition technique was used to deposit the metal layer using CHA®electron beam evaporator. The aluminum layer served as a mask for silicon etching. This mask layer thickness (and the subsequent photoresist layer) was sufficient to selectively etch the wafer to the depths studied in this work.

Following aluminum deposition, 1 μm thick layer of photoresist (Microposit S1813®from Shipley, USA) was spin-coated on the wafer using CEE®100 programmable resist spinner (Brewer Science, USA). The photoresist was used to pattern the wafer via Shipley recommended guidelines [93]. Electronic Visions EV420 optical mask aligner was used to align and expose the photoresist. The exposed resist layer was removed using Microposit MF-319®developer. Channels were patterned into the photoresist with individual widths of 300 μm. Next, the aluminum layer in the exposed region was etched out using aluminum etchant Type A (Transene, USA). This readied the wafer for deep reactive-ion etching (DRIE) of the required channel structures. The wafers were etched on one side via DRIE using the Bosch process [94] on an ALCATEL®, A601E Inductively Coupled Plasma (ICP) etcher. Exchangers

with channel depths of 110, 130 and 200 μm were created by varying the duration of the etching process. The different heights allowed comparison of channel height effectiveness on fluid mass and heat transfer. Following the etching process, any remaining photoresist and aluminum mask were removed via acetone and aluminum etchant respectively. The individual exchanger dies were then diced from the original wafer. This readied them for integration with the exchanger cover piece.

5.2.1.2 Exchanger top piece

To utilize the capillary channels for thermal scavenging applications, a top piece was added to each exchanger device. The bonded top-piece served to prevent fluid as well as heat leakages from the boiler surface. In this work, Polydimethylsiloxane (PDMS) has been used as the top-piece. The PDMS capping pieces were generated using the two-part Dow Corning®SYLGARD 184 silicone elastomer. The two parts, elastomer base and curing agent, were mixed in the ratio of 10:1 by weight. After thoroughly mixing the two parts, the mixture was degassed in a vacuum chamber for 30 minutes. Heraeus®VT 6060 programmable vacuum drying oven was used for the degassing process. Next, aluminum foil was wrapped around a silicon wafer to form a mold for casting the degassed mixture. This mold was used to cast the PDMS up to 3 mm thickness. After curing the cast PDMS in an oven at 75 °C for 1 hour, they were cut into pieces of size 40 mm by 16 mm. Working fluid inlet and exit holes were created by punching through the PDMS using a 1.5 mm diameter puncher. The PDMS were then bonded to the individual exchanger dies using low temperature plasma-enhanced bonding technique.

Plasma creates highly hydrophilic surfaces and therefore enhances bond strength. Further, the introduction of roughened surfaces and reactive chemical groups in addition to the cleaning of contaminants by oxygen plasma also improves bond quality [95]. Prior to the plasma treatment, the exchanger dies were cleaned using standard cleaning (SC) procedures. The first cleaning step (SC-1) consisted of soaking the exchanger dies for 15 minutes in a solution of 5 parts water, 1 part 27 % ammonium hydroxide and 1 part 30 % hydrogen peroxide (volume ratios) at 70 °C. This was followed by de-ionized water rinse. SC-1 step helped removed organic residues and films from the silicon surface. Next, the second cleaning step (SC-2) was used to remove thin oxide layer as well as ionic and metal atomic contaminants. Similar to SC-1 procedure, SC-2 consisted of soaking the exchanger dies for 10 minutes in a solution of 6 parts water, 1 part 27 % hydrogen chloride and 1 part 30 % hydrogen peroxide (volume ratios) at 70 °C. Again, following the SC-2 cleaning, the dies were rinsed with de-ionized water and dried with nitrogen gun. These two SC steps readied the dies for plasma activated bonding. Plasma treatment was achieved using Technics®Micro 800 table-top reactive ion etcher (RIE). The plasma power used was 40 W while the chamber pressure used was 200 mTorr. The plasma exposure was maintained for 30 s. After plasma treatment, the PDMS and Silicon sides exposed to plasma were immediately brought in contact and gentle pressed together. The Si/PDMS structure was placed on a hotplate at 75 °C for 5 minutes to increase the bond strength. Figure 5.2 shows the bonded Si/PDMS structure.

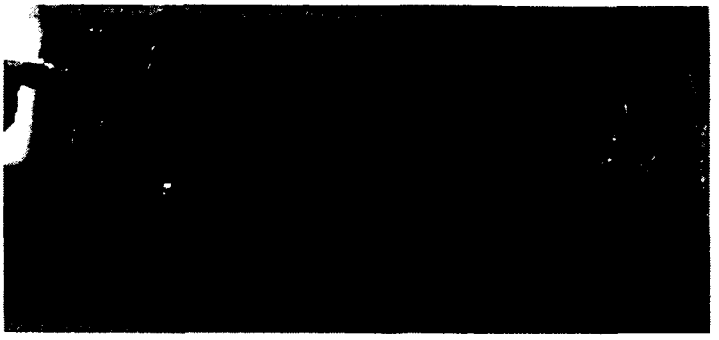

Figure 5.2: Silicon/PDMS Structure

Following the successful assembly of exchanger, fluid inlet and exit tubes were attached to the holes created in the PDMS cap. The inlet tube was a 0.0625" OD and 0.01" ID tube while the exit tube was a 0.0625" OD and 0.04" ID Tefzel®tubing sourced from IDEX Health & Science. Epoxy was applied around the tube ports to completely seal the holes. This was to prevent fluid leakage from the holes. The entire system was placed atop an acrylic carrier and held in place. The carrier allowed for easy handling of the devices as well as mount points for the various thermocouples (TC) used throughout testing. The next section describes the test setup.

5.2.2 Test Setup

Tests were conducted to characterize the ability of these devices to extract energy from the heat source into the working fluid. In this work, the energy transferred into the working fluid resulted in phase change of the fluid. Hence, characterization of these devices is based on their ability to wick working fluid from the reservoir out across the heated exchanger surface where it is evaporated. This section describes the testing procedure.

As a first step, a resistance heater was integrated with the assembled MHE device. The heater was placed directly below the exchanger surface. This heater served to simulate thermal energy source. Operation of the device relied on the ability to transform thermal energy from the heater into the internal energy of the working fluid. In real world application, the heat source could be solar radiation, waste heat, or any other thermal energy source. In this work, a resistance heater, KHLV-101/10-P, from Omega Engineering was used. A DC power source, BK Precision 1621A, was used to supply power to the heater.

Next, a thermocoulpe (TC) was mounted on the resistance heater to directly monitor the temperature of the heated exchanger portion of the device. The power supply to the heater was adjusted accordingly based on the temperature of the exchanger. This ensured the device was maintained at temperature values that closely approximate real world heat sources. Three additional TCs were also integrated to the device. The first was located below the working fluid inlet reservoir. This TC on the fluid inlet reservoir area served to monitor the fluid reservoir temperature, which was maintained below the boiling point of the working fluid, but above the original room temperature of the fluid supply. The reservoir was heated above ambient condition due to conduction heat transfer from the heat source. Hence, the temperature represented by the TC at this reservoir is the working fluid temperature just before entering the microchannel. Actual boiling, and hence vaporization only occurred within the microchannels where the temperature was maintained above the fluid boiling temperature. The next TC was suspended inside the fluid exit tube extending to a location just directly above the PDMS cap. Epoxy was used to seal the TC hole to

prevent fluid and heat leakages. This TC monitored the temperature of the vaporized fluid as it exited from the exit reservoir region. This temperature measurement was used to validate that only vapor actually exited the device. The fluid phase change implies energy transfer from the heat source. The final TC was placed above the PDMS cover to directly monitor the temperature of the device cap. As expected, thermal conduction and convection to the environment as well as the low thermal conductivity of PDMS resulted in a lower temperature at the top of the PDMS cap than surfaces closer to the thermal sources. All TCs used were k-type devices supplied by Omega Engineering. The raw data from the experimental runs were recorded into the computer for analysis using National Instruments *LabVIEW*®. The test rig is as shown in Figure 5.3.

Figure 5.3: Boiler Plate Setup

A KDS-100 syringe pump (KD Scientific, USA) was used to add working fluid to the exchanger inlet reservoir. The pump was set to maintain fluid within the reservoir

throughout testing. The fluid inlet flow rate was noted. At the exit line, a receiver in the form of a syringe was attached to the exit tube. Hence, the vaporized working fluid was allowed to exit the exchanger and re-condense in the receiver syringe. The receiver syringe containing re-condensed working fluid was weighed before and after each testing procedure. The difference in weight for each experimental run established the actual amount of working fluid vaporized. To ensure that only vaporized (or energized) fluid exited from the MHE, the assembled device was tilted at a angle of 18 °to the horizontal. This way the fluid in the inlet reservoir does not freely flow through the microchannel and out through the exit tube. Rather, only the working fluid pulled from the reservoir into the microchannels by capillary action that has received sufficient energy to vaporize climbs through the channels and exits the exchanger. The schematics of the setup is shown in Figure 5.4. In solar thermal applications, tilting the device has the added benefit of increasing the amount of solar energy captured. Generally, flat-plate solar collectors are tilted so as to capture the maximum radiation from the incident solar radiation [96].

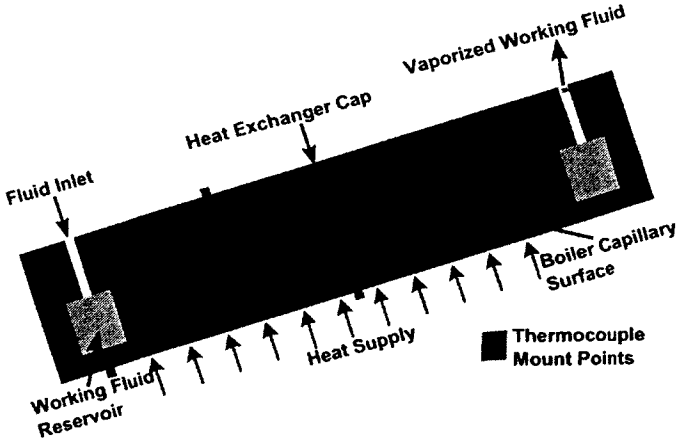

Figure 5.4: Schematics of Boiler Plate Setup

The 3M^{TM} NOVEC 7200 refrigerant was used as the working fluid in this work. This refrigerant was selected for several reasons including its boiling point of 76 °C, which is within the low temperature heat source range examined in this work. Other fluids may also be used depending on the application and operating temperatures. The device itself is not temperature or fluid specific, but could be tailored to a wide range of fluids and operating temperatures based on the heat source.

For effective comparison of the various MHE devices, the power supply to the resistance heater was kept at a constant value for all MHEs tested. A ceramic 10 ohm resistor was connected in parallel with the resistance heater and used to verify the input energy. Initial tests were conducted with different power input values to establish the steady state temperature of the exchanger with no working fluid present. This validation test with no working fluid represented a "dry" test. Based on the dry validation test, power supply of 2.58 W was selected for the actual "wet" MHE operation. This power input value yielded steady state dry operating temperature of about 102 °C. First, this temperature value was selected as it is above the boiling point of the working fluid and therefore ensured the operation of the device when working fluid was added. Second, this temperature value closely approximates flat plate solar collector temperature values as well as other available low grade waste thermal sources.

Working fluid was added to the inlet reservoir after the exchanger had fully heated to dry steady state conditions. With working fluid present in the device, the temperature of the exchanger was reduced. The new operating temperature was sufficient to cause working fluid vaporization, however. Working fluid was added as

needed through the syringe pump to avoid a return to the "dry" steady state conditions. Each test was conducted for several minutes. In real world waste heat scavenging applications, this heat transfer through the working fluid has the additional benefit of system cooling which in turn enhances the overall system efficiency. Further, the heat harvested from the thermal source may be utilized for other power applications.

The amount of fluid vaporized during operation characterized the overall exchanger performance. For each exchanger, multiple tests were conducted to ensure results were both repeatable and reliable. The average working fluid mass transfer rate was determined from the multiple experimental runs based on mass versus time readings. The re-condensed fluid was weighed after each testing to provide mass values while a stopwatch was used to monitor experimental time. Hence, the mass transfer rate $\dot{m} = \frac{mass}{time}$. As an additional metric of performance, the energy transfer from the heat source for each test was calculated based on the mass transfer rate and the known exchanger area.

The exchanger area was calculated based on channel length and width dimensions. By design, the channel width was equal to the separating wall width. Hence, the total channel area for each exchanger was half of the total heated exchanger area since the calculation did not consider the walls of the channels as part of the exchanger surface. The total exchanger channel area was 165.8 mm^2. This was half of the total heated exchanger area due to the presence of the channel walls where no working fluid could be present.

The working fluid, HFE 7200, had a heat of vaporization, h_{fg}, of 125 $\frac{kJ}{kg}$. Using the recorded mass transfer rates, the power required to drive this phase change was

determined via the heat of vaporization. This was compared to the exchanger area to determine a measure of power consumption per area in $\frac{kW}{m^2}$.

5.2.3 Experimental Error

The uncertainty associated with the measured and calculated values was determined for this work. Table 5.1 shows the compiled uncertainties. Temperature and fluid mass were measured parameters and their uncertainties depended on the sensors used. Power input, power density and flow rate were calculated parameters and their uncertainties depended on the measured parameters.

Table 5.1: Experimental Error

Measurement	Error	% of Typical Value
Temperature	± .50 °C	± .575
Power Input	± 15.59 mW	± .604
Mass of Working Fluid	± .0001 g	± .007
Time	± .001 sec	± .0002
Flow Rate of Working Fluid	± .0002 $\frac{mg}{s}$	± .007
Power Density	± .127 $\frac{W}{m^2}$	± .006

5.3 Results and Discussion

In this section, results of the MHE testing are presented. Tests were conducted to characterize the rate of mass transfer and power consumption of the MHE when working fluid and thermal energy were added to the devices.

Power supply to the exchanger was maintained at 2.58 W during testing. This power input resulted in operating temperatures near the working fluid boiling point as described in Section 5.2.2. Tests produced a temperature plot similar to that shown in Figure 5.5. There is a cooling effect due to addition of working fluid. This improves

overall system efficiency. Further, the extracted heat is used to drive phase change in the working fluid thereby leading to energy harvesting.

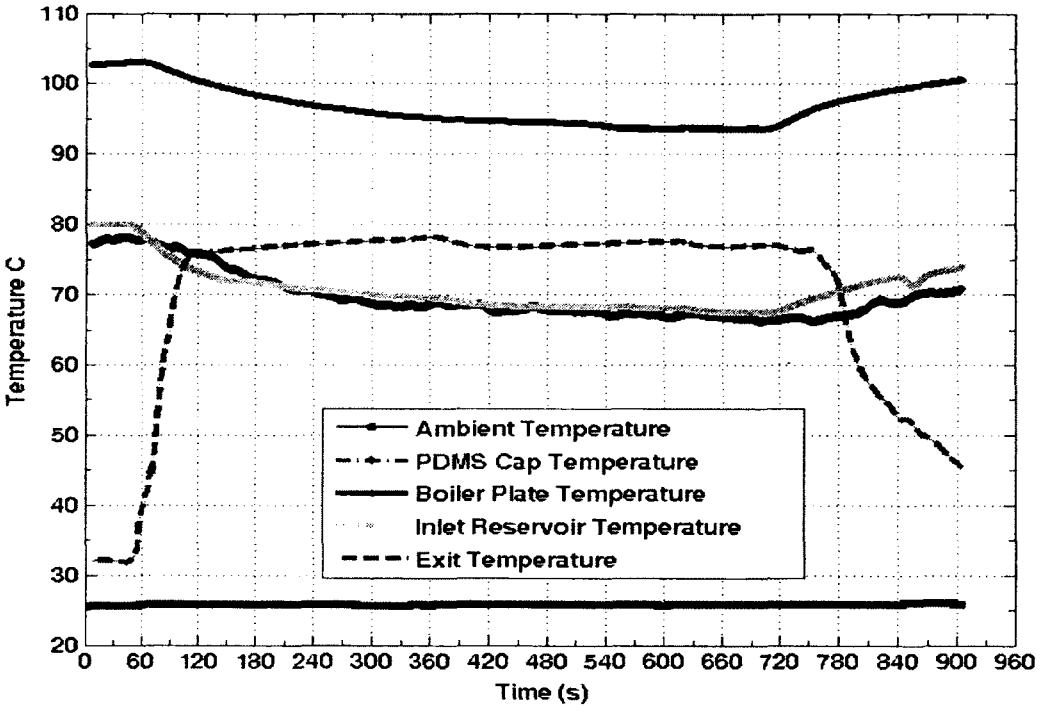

Figure 5.5: Typical Boiler Temperature Conditions

Irrespective of the mass transfer rate, the temperature of the vaporized fluid is noted. The TC suspended in the fluid exit tube recorded the vapor temperature as working fluid exited the exchanger. The boiling point of HFE 7200 is known to be 76 °C. The temperature of the evaporated fluid as noted in Figure 5.5 confirmed that the vapor was saturated. The inlet reservoir and PDMS cap temperatures were noted to be below the fluid boiling point during operation. Hence, fluid phase change took place primarily within the channel region, as intended.

Mass transfer rate and energy consumption were measured for each exchanger construction. These numerical results for each exchanger design are summarized in Table 5.2.

Table 5.2: Boiler Operation Results Given 2.58 W Input

Channel Depth (μm)	**Mass Transfer Rate (mg/s)**	**Energy Consumed (kW/m^2)**
110	3.47	2.63
130	3.57	2.70
200	3.95	2.99

First, the difference in channel height is worth noting. With increased channel height, there is more surface area and therefore increased capillary action. This trend can be seen with the increase in channel depth from 110 μm to 200 μm. Increased capillary action resulted in increased mass transfer and power consumption. This result agrees with work evidenced in literature that increasing open channel height increases capillary response [85, 75]. In this work, the mass transfer rate was increased by 13.8% as the channel depth increased from 110 μm to 200 μm. The mass flow rate versus exchanger channel depth as recorded is shown in Figure 5.6.

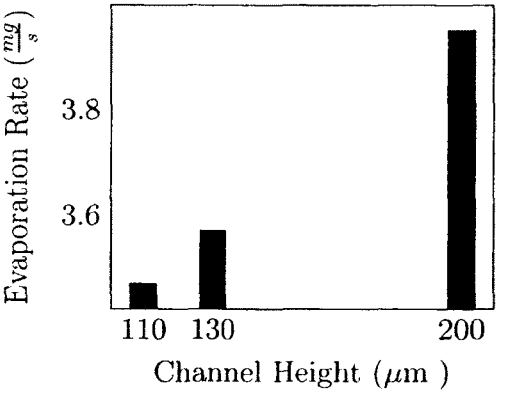

Figure 5.6: Mass Flow Rate Versus Channel Depth

Further the energy harnessed per unit time from the heat source via working fluid phase change was calculated based on the fluid mass transfer rate and heat of vaporization. Heat of vaporization of HFE 7200 is known to be 125 $\frac{kJ}{kg}$. Given an input power of 2.58 W to the boiler plate, the energy consumed by the 110 μm channel was 0.43 W while the 200 μm channels consumed 0.49 W, an increase of about 2.3 % given the increase in channel depth. These values represented power densities of 2.63 $\frac{kW}{m^2}$ and 2.99 $\frac{kW}{m^2}$ for the 110 μm and 200 μm channels respectively.

Overall, the micro boiler presented in this work may be utilized with other working fluids and operating temperatures. Applications include heat sources like microelectronics, solar radiation and many others. These current boiler plates operate well within the known solar heating values (700 $\frac{W}{m^2}$ [97]) and so are a natural fit for micro solar thermal applications. Also, by choosing an appropriate working fluid, the exchanger operations can be applied to a wide variety of different situations and temperature ranges. The device may also be easily scaled up for macro scale applications including automobile engines and industrial waste heat sources.

5.4 Conclusions

The investigation of a small-scale, MEMS-based heat exchanger has been reported. Exchanger operation was based on capillary channels ability to wick HFE 7200 working fluid across a heated surface to drive mass transfer and thermal energy consumption from a heat source. Fabrication of the channels was based on microfabrication techniques that produced channel widths of 300 μm with heights of 110 μm , 130 μm and 200 μm. Tests were conducted to compare the operation of

these devices' abilities to extract thermal energy from a heat source via phase change of the working fluid.

Given an input of 2.58 W to the boiler, tests showed an overall power consumption of 0.43 W, 0.45 W and 0.49 W for the 110 μm, 130 μm and 200 μm channels respectively. These values represent the power harvested by the working fluid from the heat source in addition to the cooling effect provided. These results represent power densities of 2.63 $\frac{kW}{m^2}$, 2.70 $\frac{kW}{m^2}$ and 2.99 $\frac{kW}{m^2}$ respectively. The total mass transfer of working fluid was shown to be 3.47 $\frac{mg}{s}$, 3.57 $\frac{mg}{s}$ and 3.95 $\frac{mg}{s}$ for the 110 μm, 130 μm and 200 μm channels respectively. It is anticipated that further increasing the capillary height of the MHEs tested will further increase the energy consumption of the devices.

CHAPTER 6

SIMPLE AND LOW COST METHOD FOR METAL-BASED MICRO-CAPILLARY CHANNELS FOR HEAT EXCHANGER USE[†]

6.1 Introduction

Micro-channel heat exchangers (MHEs) transfer heat through multiple flat fluid-filled tubes containing small channels. MHEs are important components in many devices that require compact thermal energy removal. It is crucial for the microchannel to effectively handle heat as well as have efficient manufacturing process.

Effective thermal flux management is critical for the operation of micro-electro-mechanical systems (MEMS). Temperature affects both the performance and reliability of microelectronics [98]. Further, the thermal flux dissipated by these devices represents energy losses when compared to the useful output from the system. Hence the ability to effectively harvest heat from a MEMS device would improve the overall efficiency of the device. Some cooling schemes include pool boiling, detachable heat sinks, channel flow boiling, microchannel and mini-channel heat sinks, jet-impingement, and sprays [99]. The use of a thermoelectric cooler to dissipate heat from a microchip has also been demonstrated [100]. These methods focus on the ability to effectively cool

[†]This material has been submitted for publication as Ogbonnaya, E., Champagne, C., and Weiss, L., 2013. "Simple and low cost method for metal-based micro-capillary channels for heat exchanger use."

MEMS devices. In this chapter, a cooling technique utilizing low cost micro capillary channels which may enable simultaneous energy scavenging with the dissipated heat is presented. This technique can also be integrated to large scale devices to harvest waste thermal energy that is cast off to the surroundings as a part of a larger process.

Traditional micro and nano fabrication has focused on the use of silicon as a substrate. Silicon-based MEMS currently dominate the world of micro and nano manufacturing. This is largely due to the well established fabrication procedures for Si-MEMS. However, the limitations in silicon and silicon processing have led to investigations of alternative materials capable of providing functionalities at cost points not achievable with silicon. High thermal conductivity and improved mechanical integrity make metal-based MEMS preferred over silicon [101]. The challenge however is the ability to efficiently fabricate these metal-based devices at an economically viable cost.

One important fabrication strategy for metal-based microscale structures is the LiGA technique [102]. LIGA is a German acronym for "lithography, molding and electroplating" [103]. Metal based structures can be fabricated by this technique using X-ray/UV lithography on polymeric resists followed by electrodeposition into developed resist structure. However, deep lithography is an expensive process.

Micro-machining is also employed in manufacturing MHEs. Machining has the advantage of processing a wide range of materials. However, as the cutting tool wears, there is a negative effect on the quality of machined parts [104]. Replication of metallic HARMS by compression molding has also been demonstrated [101]. Compression molding generally occurs at high temperatures. This creates near surface reaction

between the mold inserts and the molded metal at such high temperatures. Also the yield strength of the mold insert has to be high enough to withstand the stresses required for molding metal parts.

In this work, a low cost method for the fabrication of a heat exchanger with metal-based microchannels using the LiGA technique is presented. Lithography is used to pattern dry film negative photoresist on the substrate. The resist is laminated over the substrate and exposed with a UV source. The use of dry film resist allows for simple and inexpensive microchannel patterns without requiring advanced cleanroom equipment. Following the lithography process, electrodepostion of metals is used to fill the recesses patterned in the resist. After electroplating, the remaining resist is dissolved leaving behind free standing metal structures. The fabricated exchanger is then evaluated based on thermal absorption of simulated waste heat sources and capillary action of the metal channels themselves.

The MHE is designed to pair with other devices like Thermoelectric generators, TEGs, for thermal management application. In this manner, energy dissipated from other devices and processes may be efficiently introduced and rejected from the TEG itself via the heat exchanger. This increases thermal cooling effect from such devices and processes, and enhances the performance of the TEG and overall effectiveness of the thermal scavenging. There are numerous other applications that include use in micro steam systems as well as many others [76]. The use of microfabrication techniques presents several advantages. First, batch fabrication allows the generation of many devices from singular processing steps [91]. Further, the small scale of the

approach allows installations of small, single units as well as larger applications where many devices work from a larger thermal energy source.

The exchanger presented in this work relies on multiple rows of capillary channels to promote mass and heat transfer using working fluid with low-temperature boiling point. Figure 6.1 illustrates the basic concept. Thermal energy dissipated as heat is applied to the lower surface which is patterned with capillary channels. The rectangular capillary channels extend between two working fluid reservoirs and continually feed working fluid across the heated surface. This results in phase change of the working fluid and heat transfer away from the thermal source. The use of phase change has been less common in the field of thermal scavenging. Nonetheless, the advantages of this approach have been manifested in applications like computer chip cooling [82, 83]. Micro-devices and micro channel design have been of particular interest [83]. Tuckerman and Pease first noted that miniaturizing cooling channel dimensions leads to increased heat transfer efficiency [84]. Open rectangular capillary channels have been previously modeled and validated experimentally by Kim et al [85]. This foundational work served to provide many of the basic channel dimensions that were studied as part of this current experimental effort. In CPU application there has also been research in capillary driven exchangers where working fluid phase change is again the primary means of heat transfer [85, 86, 87, 88, 89, 90]. Working fluids have varied, but have typically depended on the temperature ranges of the final applications.

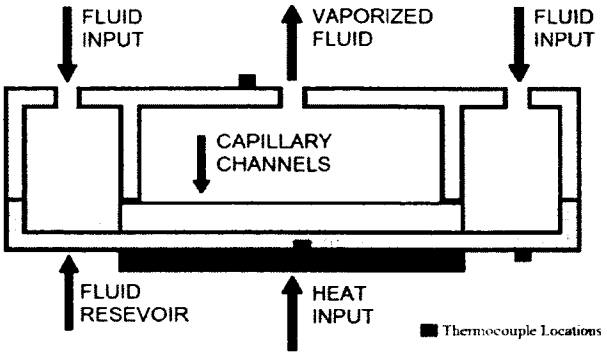

Figure 6.1: Micro Capillary Exchanger Design

As a measure of the device performance, the thermal energy consumption is provided as a direct insight into exchanger ability to extract thermal energy via the various capillary channels and drive working fluid mass transfer. The energy consumption per unit time characterizes the power consumption of the working fluid. This metric of performance is normalized by the area of the exchanger plate to yield values in $\frac{kW}{m^2}$. Through the use of phase change for increased heat transfer and microfabrication, the final device will be a condensed and scalable product suitable for widespread implementation. Further, an investigation of the working fluid wettability is presented, centered on working fluid contact angles and capillary action.

Previous MHE work by our group at Louisiana Tech University compared the operation of exchangers fabricated with silicon capillary channels to those fabricated using SU-8 material for capillary channel walls [92, 75]. The use of SU-8 allowed an increased range of channel heights compared to the basic silicon structures. Heat transfer was, however, impeded in the SU-8 channel walls as SU-8 is a non-conductive polymer material. Hence, new techniques have been employed to examine the use of

metal as a primary channel wall material. These steps required the use of SU-8 as a patterning agent. This represents an expensive and time consuming process. In this present work, the process presented replaces the SU-8 bounding structure by patterning a low cost and simple dry film on the substrate followed by electrodeposition process. Through this approach, a more cost effective metal-based micro capillary structures may be achieved. Further, this unique technique expands the use of potential substrates beyond silicon as the substrate is no longer required to be flat.

6.2 Experimental Methods

6.2.1 Fabrication

In this present work, we demonstrate a cost effective technique of fabricating metal-based micro capillary channels on various substrate types. Two types of substrates were considered in this work. These included silicon and copper substrates. This technique may be applied on a wide range of other substrates. The development of metallic microchannels was aimed at increasing thermal conductivity within the channel walls. Initial work has focused on nickel channel walls. Details of the processing and preparation steps are discussed in this section.

Overall dimensions of the exchangers were 16 mm in width by 38 mm in length. This included the reservoir sections that surrounded the channels as noted by Figure 6.1. Channel widths were maintained at 300 μm for both silicon and copper substrates. For the copper substrate devices, first, copper sheet of 500 μm thickness were cut into 22 mm by 40 mm area. The copper substrates were initially polished mechanically and then degreased in a solution of 5 % acetic acid and pinch of salt. They were next

rinsed with DI water. This prepared the substrate for lamination of the photoresist material. A layer of Ordyl P-50100 dry film (from ElgaEurope, Italy) was laminated on the substrate. Hot roll machines are generally used to laminate the resist over substrates. In this work, the film was carefully laid manually over the substrate. Heat and pressure were applied using a domestic iron in this lamination step to make the dry film conform to the substrate surface. A sheet of paper was used as a protective layer between the domestic iron and the photoresist to prevent the film from sticking to the iron.

Ordyl P-50100 has a film thickness of 100 μm. Hence, the final height of the capillary channels formed using the dry film resist were 100 μm for each device. The photoresist films may be stacked on each other if taller channel dimension is desired. The challenge is that with multiple stacks the channel walls lose vertical alignment. Following the lamination of the P-50100 resist, exposure was done using a UV light source. In this work, the photoresist was exposed using a fluorescent lamp. Optimization of the exposure time showed that 15 minutes was sufficient to expose the film under a 40-watt fluorescent lamp. The development of the exposed resist using 0.8 $\pm$ 0.2 % K_2CO_3 at 28 $\pm$ 2 °C as recommended by ElgaEurope produced the required mask for electroplating of nickel. Immersion developing technique was used with strong agitation for the development step. Next, the substrate was rinsed with DI water and dried with nitrogen gun. Electrodeposition was then used to form nickel channels within the bounding walls. However, for the electroplating step, the back side of the copper substrate was covered with silicone single-sided adhesive tape. This ensured that only the patterned area within the photoresist structure was filled by

the electroplating process. Three channel heights were fabricated. The constructed devices had channel heights of 60, 70 and 90 μm respectively. Following electroplating, the remaining P-50100 mask was lifted off the substrate using 3% KOH at 50 °C.

Fabrication on the silicon substrate began with a standard 400 μm thick, double-side polished <100> silicon wafer. A 5 nm thick layer of chrome was deposited directly on the top silicon surface followed by 75 nm of gold. This initial deposit of metal served as an adhesion layer for the SU-8. Both metal layers were deposited using electron beam physical vapor deposition technique. Next, a layer of Microchem 2100 SU-8 was spun onto the wafers and exposed using UV mask aligner. Following SU-8 development (via Microchem recommended practices), the wafers were ready for dicing. Further processing steps were required to produce the nickel capillary channels. Nickel was electrodeposited into the recesses defined by the lithography process. The gold layer beneath the SU-8 served as the electroplating electrode. Channel widths were maintained at 300 μm . The SU-8 structure served as the mask for the nickel deposition on the substrate. Hence, nickel capillary channels were grown from the conductive bottom between the SU-8 structures. Two channel heights were fabricated. The constructed devices had channel heights of 115 and 142 μm respectively. Following electroplating, the SU-8 mask was lifted off the substrate using Microchem PG remover and only the nickel capillary channels remained.

Electrodeposition in each case was accomplished using a Watt-type warm bath [49]. Nickel capillary channels were grown from the conductive bottom between the P-50100 and SU-8 structures. The electrochemical deposition conditions for the nickel

plating are shown in Table 6.1. All chemicals used were reagent grade from Sigma-Aldrich®. Final channel height was based on total elapsed time during electroplating. Figure 6.2 shows a completed nickel MHE base on silicon and copper substrates.

Table 6.1: Watts-type Nickel Plating Conditions

Electrolyte Composition (g/l)	**Working Condition**
Nickel Sulfate-6-Hydrate = 250	Temperature = 45 °C
Nickel Chloride-6-Hydrate = 45	Current Density = 50 $\frac{mA}{cm^2}$
Boric Acid = 30	pH = 4.0

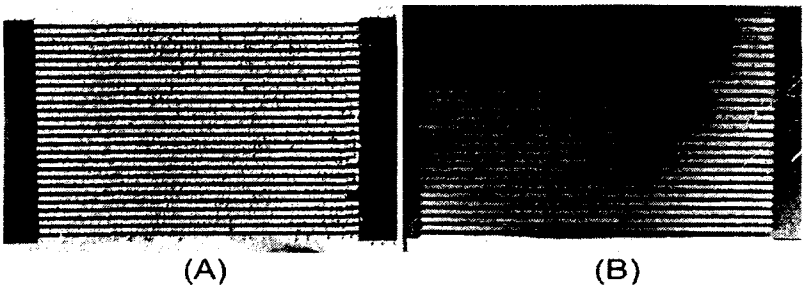

Figure 6.2: MHE Base with Nickel Capillary Channel Walls on (A) Silicon, (B) Copper

To utilize the metal-based capillary channels for thermal scavenging applications, a top piece was added to each exchanger device. The bonded top-piece served to prevent fluid leakage as well as provide volume for evaporated fluid. A cast high temperature resistant, rigid urethane has been used as the top-piece. Bonding techniques like eutectic bonding [105] may also be utilized to achieve metal-based top structures.

An initial top piece was fabricated from acrylic and used as a mold for each subsequent top fabricated as part of this work. The subsequent tops were produced using a two-part latex mixture which was poured around the original mold piece. Removal of the original piece from the dried mold compound allowed the generation of multiple top pieces of consistent dimension that were utilized in the fabrication of the

devices presented in this work. Because the original piece was fabricated to fit directly atop the exchanger surfaces each subsequent top piece produced from the mold shared those attributes. This acrylic top was sized to fit directly over the exchangers and included working fluid reservoirs. These reservoirs added volume for the working fluid utilized in these experiments. In addition, a dome was created above the capillary channels where vaporized working fluid was collected. This allowed monitoring of temperature on the acrylic surface as a result of evaporation and phase change. The schematics of the assembled exchanger and steam dome is shown in Figure 6.1. The overall size of the castings was 5 mm high by 43 mm in length by 22 mm in width. Each top was permanently epoxied over the exchanger base to achieve sealing and prevent working fluid from leaking between the top and exchanger components. Figure 6.3 shows an assembled exchanger and acrylic top. The integration of the exchanger plate and steam dome readied the device for testing.

Figure 6.3: Exchanger Plate Coupled With Steam Dome

6.2.2 Test Setup

The principle operation of these devices is based on their ability to wick working fluid from the reservoirs out across the heated exchanger surface where it is evaporated. The working fluid pumping effect therefore depends on the capillary channels. The

testing and characterization efforts in this work examined the ability to wick fluid across the heated exchanger surface. As part of this effort, the working fluid and surface interaction was also specifically investigated to determine the wettability of the nickel channels. This section describes the testing and test setups for these experiments.

A similar setup was used for all thermal tests. First, the assembled MHE as described in Section 6.2.1 (Figure 6.3) was integrated with a resistance heater and thermocouple. The resistance heater served to simulate the real-world energy source and the thermocouple, TC, was used to monitor temperature of the exchanger during operation. The resistance heater was an Omega Engineering KHLV-101/10-P, and was coupled to the lower side of the exchanger. A DC power source, BK Precision 1621A Digital DC supply, was used to power the heater. Three TCs were attached to the assembly. The first TC was integrated with the resistance heater to directly monitor the temperature of the heated exchanger portion of the device. The second TC was placed below one of the working fluid reservoirs while the third TC was located on the top surface of the MHE. The TC on the fluid reservoir area served to monitor the fluid reservoir temperature, which was maintained below the boiling point of the working fluid as intended. The temperature measured by the TC at the reservoir represented the working fluid temperature just before entering the microchannel. Since the two reservoirs are symmetrical, the temperatures at the two reservoirs are equivalent. Finally, as the fluid evaporated, the vapor caused a rise in temperature of the steam dome surface. After all fluid has been evaporated, the steam dome temperature started to drop due to the loss of energy transfer. The TC on the steam done was therefore

used as an additional check in monitoring availability of fluid within the channels. All TCs were k-type devices supplied by Omega Engineering. National Instruments Labview®was used to log all the temperature data into a computer for analysis.

The assembled system was placed atop an acrylic carrier and held in place. The carrier allowed for easy handling of the devices as well as mount points for the various TC used throughout testing. Figure 6.4 shows the fully assembled exchanger, steam dome, and carrier ready for testing.

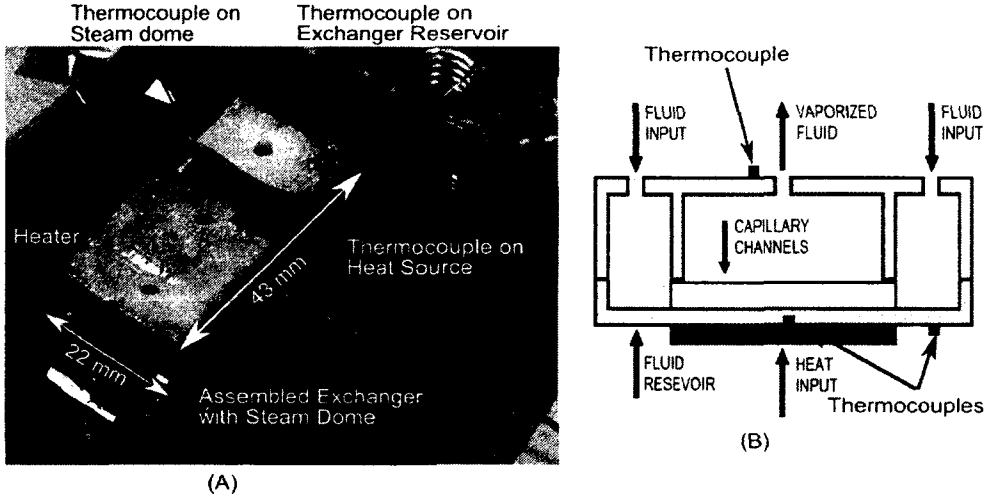

Figure 6.4: Assembled Heat Exchanger Setup on Carrier (A), and Schematics (B)

Fluid was added to the exchanger reservoirs through the access holes atop the reservoirs using a syringe. The weight of the syringe containing working fluid was measured prior and after each testing procedure. The amount of fluid consumed for each test was the difference in the measured weights. The working fluid was $3M^{TM}$ NOVEC 7200 refrigerant. This refrigerant was selected for several reasons including its boiling point of 76 °C. This temperature was suitable for many waste heat dissipation and scavenging applications, allowing for effective heat removal.

The power supply P, to the resistance heater was kept at a constant value for all MHEs tested. P = VI, where V is the voltage and I is the current across the resistance heater. The value of P was maintained at 2.57 W irrespective of exchanger design using a DC power source. The resistance heater measured 25.4 mm x 25.4 mm. Hence, the power flux density from the heater to the exchanger surface was 3.98 $\frac{kW}{m^2}$. Initial validation tests showed that power supply of 2.57 W was sufficient to obtain steady state temperature of about 96 °C on the MHEs when operated in a dry condition. In these initial "dry" tests, the temperature of the MHE was higher than the working fluid boiling temperature. This ensured operation of the device, when working fluid was added, at the boiling point itself. A ceramic 10 ohm resistor was connected in parallel with the resistance heater and used to verify the input energy.

After the exchanger reached "dry" steady temperatures, working fluid was added to the reservoirs which reduced exchanger temperatures. The new operating temperature with working fluid present represented the "wet" steady state operating point for these devices. After the initial cool down, the syringe was weighed and working fluid was added as needed to the device reservoir to maintain the operation of these exchangers at steady state conditions for several minutes. Temperatures were monitored using the various TCs throughout testing. Temperature rise indicated lack of working fluid within the device. Fluid was added to the heat exchanger if temperatures began to rise to maintain the steady-state operating condition. The addition of working fluid avoided a return to a dry operating condition. In MEMS applications, this will ensure effective heat removal from the heated system. Tests

produced a temperature plot similar to that shown in Figure 6.5 where the steady state testing section is noted.

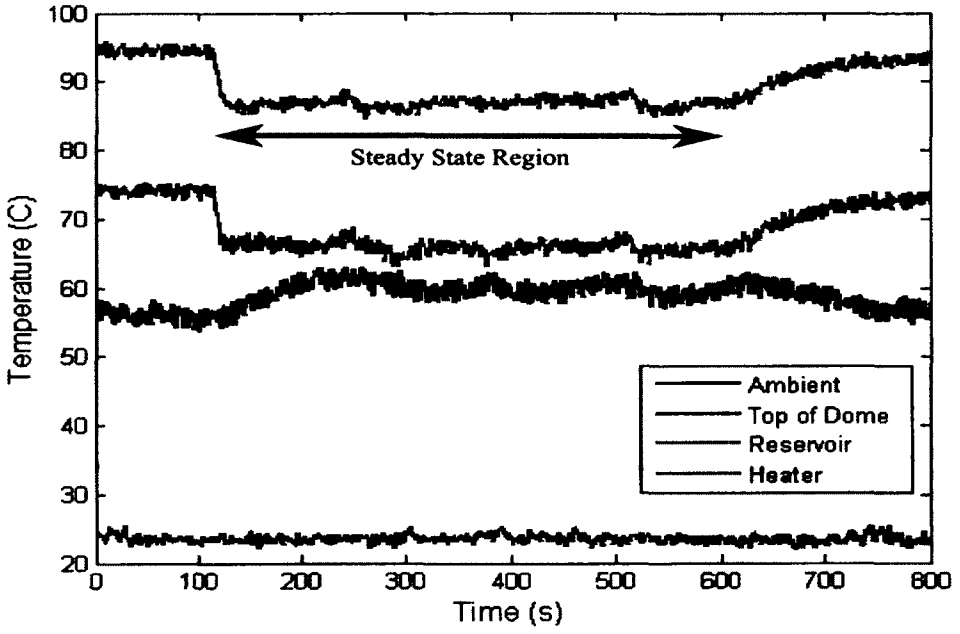

Figure 6.5: Standard Exchanger Temperature Profile

The exchanger performance was characterized by the total fluid consumed during testing. Hence, the mass flow rate $\dot{m} = \frac{mass}{time}$. The initial cool-down from dry steady state conditions was not counted as part of the working fluid consumption. The thermal energy consumption provided a direct insight into exchanger ability to extract thermal energy via the various capillary channels and drive working fluid mass transfer. The energy consumption per unit time characterized the power consumption of the working fluid. This metric of performance was normalized by the area of the exchanger plate to yield values in $\frac{kW}{m^2}$.

In this work, the evaporated working fluid was allowed to exit the acrylic top via a centrally located exit hole. In this respect, the exchangers represented an "open" system with working fluid free to exit. This allowed a direct study of the capillary channel designs with respect to mass transfer and power consumption. Future work will examine a true "closed" system where working fluid is condensed after evaporation and returned to the reservoirs.

In these tests, the reservoirs were heated above ambient condition due to conduction heat transfer from the heat source, which allowed some evaporation from the reservoir surfaces themselves. Comparison between exchanger types, however, represented the design and operation of the capillary channels directly as the device was constructed using same dimensions and operated at the same temperatures. This ensured similar reservoir evaporation behavior independent of channel design. Because of this behavior from the reservoirs, the thermal consumption metric represents the combination of both capillary-based mass transfer as well as that due to any incidental reservoir evaporation. As expected, thermal conduction and convection to the environment from the top surface resulted in a lower temperature at the top of the device than surfaces closer to the thermal sources. In the final, applied design where the heat exchanger is no longer an open thermodynamic system, evaporation from the reservoir area is less concerning. Thermal energy evaporated from any part of the lower surface serves to aid heat transfer.

Multiple tests were conducted for each exchanger. The average working fluid mass transfer rate was determined from the multiple experimental runs. Mass transfer rate was recorded via experimental mass versus time readings. Furthermore, the

mass transfer rate and the known exchanger area were employed to calculate energy consumed in each experiment. The energy consumed by each device is a further metric of performance.

The total channel area for each exchanger was calculated based on channel length and width dimensions. This method of calculation did not consider the walls of the channels as part of the exchanger surface. This produced a total exchanger channel area of 165.8 mm^2. This was half of the total heated exchanger area due to the presence of the channel walls.

The power needed to drive phase change in the working fluid was calculated based on the fluid's latent heat of vaporization and measured mass flow rate. The working fluid, HFE 7200, had a heat of vaporization, h_{fg}, of 125 $\frac{kJ}{kg}$. The power consumption was normalized by the area of the exchanger plate to obtain a measure of power consumption per area in $\frac{kW}{m^2}$. This metric is especially useful when considering thermal outputs of specific devices like TEGs or generic sources. The formulations used for analysis in this work are summarized in Equations 6.1, 6.2 and 6.3.

$$\text{Mass flow rate } \dot{m}\ (\frac{kg}{s}) = \frac{\text{total mass consumed, kg}}{\text{time, s}} \tag{6.1}$$

$$\text{Power to phase change (kW)} = \dot{m}(\frac{kg}{s}) \times h_{fg}(\frac{kJ}{Kg}) \tag{6.2}$$

$$\text{Working fluid heat flux } (\frac{kW}{m^2}) = \frac{\text{Power to phase change}}{\text{Heat Exchanger Area}} \tag{6.3}$$

Working fluid surface interaction characterization was based on photography of individual working fluid droplets atop electroplated nickel surfaces. These photographs were then investigated. Droplets were characterized based on angle of interaction with the surface and compared to known results found in literature. As a further test,

individual exchanger dies were mounted vertically and partially immersed into a bath of working fluid. This allowed the working fluid to climb the vertical capillary channels and provided another measure of capillary effectiveness. In both cases photographs were taken with a Kodak®Super-Macro camera. Individual capillary rise heights were determined based on pixel count and conversion. The specific rise heights in pixels was converted to millimeters based on the photographed components of the MHE with known dimensions. Channel walls, for example, were known to have widths of 300 μm. Figure 6.6 shows a nickel MHE immersed in working fluid bath as described. This illustrates the capillary nature of the nickel channels, a proof that capillary pull effect exists within this unique construction. These direct capillary tests were conducted in open atmosphere at room temperature.

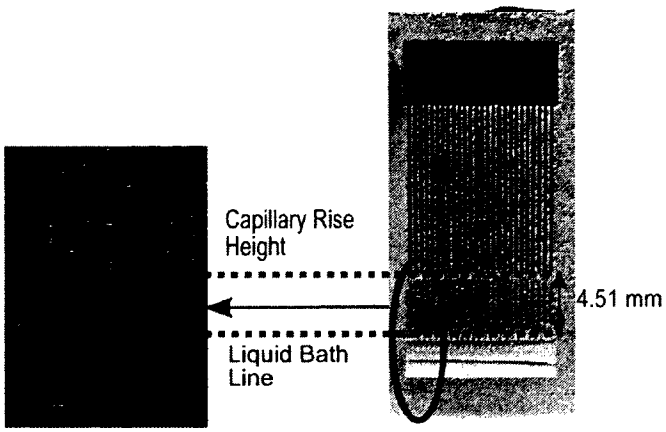

Figure 6.6: Capillary Rise Height Test for Nickel MHE

6.2.3 Experimental Error

The experimental uncertainty associated with this work is summarized in Table 6.2. The uncertainties of directly measured parameters depended on the errors of

instruments used while the uncertainties of calculated values were determined using Kline and McClintock [106] method of uncertainty analysis. In this method, let x_n be the independent or measured variables and let w_n represent the uncertainties of the independent variables. Then the errors associated with the calculated parameters were determined using Equation 6.4, where w_f is the associated error of function, f. Input voltage, current, temperature and mass were measured parameters and their uncertainties depended on the sensors used. Power input, power density, height and flow rate were calculated parameters and their uncertainties depended on the measured parameters.

$$w_f = \sqrt{\left(\frac{\partial f}{\partial x_1} w_1\right)^2 + \left(\frac{\partial f}{\partial x_2} w_2\right)^2 + \ldots + \left(\frac{\partial f}{\partial x_n} w_n\right)^2}. \tag{6.4}$$

Table 6.2: Measurement and Calculation Uncertainties

Measurement	Error	% of Typical Value
Temperature	± .50 °C	± .575
Power Input	± 15.59 mW	± .602
Mass of Working Fluid	± .0001 g	± .007
Time	± .001 sec	± .0002
Flow Rate of Working Fluid	± .0002 $\frac{mg}{s}$	± .007
Power Density	± .127 $\frac{W}{m^2}$	± .006

6.3 Results and Discussion

This section presents results of the MHE fabrication and testing. First, the most significant result is the ability to have fabricated the MHE devices on a copper substrate with a low cost process conducted outside the cleanroom environment. Since this technique does not require a cleanroom environment, capital cost or investment

on cleanroom equipment can be avoided. The Ordyl film may be laminated with hot roll laminator machines and exposed using any UV source like fluorescent lamps. Further, the low cost of the dry film resist itself (€15/m^2 or ~$20/$m^2$) [107] makes it an economical alternative to traditional negative resists such as SU-8. The processing time was significantly reduced by the use of this technique. Whereas work using SU-8 2100 had a processing time of several hours, largely due to the soft bake and post exposure bake times as recommended by MicroChem [108], the Ordyl P-50100 dry film resist could be processed in under 20 minutes. More so, the adhesive dry film resist readily adheres to multiple substrate types. As an additional benefit, this technique did not require a flat substrate surface for successful microfabrication process. Further, it allowed for fabrication on substrates of varying geometry. Traditional microfabrication technique has been limited to substrates with very flat surfaces, specific dimension and geometry.

The technique presented in this work has been successfully utilized to fabricate microchannels on both silicon and copper substrates. Prior model results predicted higher thermal performance for MHE on a copper substrate as a result of the high thermal conductivity of copper [75]. The challenge. however, has been the difficulty in using traditional microfabrication processes on copper (and indeed other metal) substrates. Initial fabrication on copper substrate has been successfully demonstrated in this work. Similar to traditional microfabrication, this technique is highly scalable and also allows for batch manufacturing.

Thermal characterization results presented in this chapter focused on silicon and copper substrate heat exchangers. Tests were conducted to characterize the operation

of these nickel-based MHE. These tests characterized the rate of mass transfer and power consumption of the MHE when working fluid and thermal energy were added to the devices. Tests produced a temperature plot similar to that shown in Figure 6.5 where the steady state testing section is noted. The device was operated below the melting or deforming temperature of the steam dome acrylic material. Hence, the dome piece was observed to be thermally stable throughout the duration of the experiment. Other materials/bonding techniques may be used in the future based on final applications and operating conditions.

Energy input to the exchanger was maintained at 2.57 W (or 3.98 $\frac{KW}{m^2}$ based on area of the heater) for the thermal-based testing. This resulted in operating temperatures near the working fluid boiling point. Mass transfer rate and energy consumption were measured for each type and construction of exchanger. The MHE devices included two Si-based designs with 300 μm width capillaries and depths of 115 and 142 μm. Also, three copper-based designs were studied with 300 μm width capillaries and 60, 70 and 90 μm depths. Figure 6.7 graphically shows the working fluid evaporation rates for each design. Specific numerical results for each exchanger design are shown in Table 6.3. Mass transfer via the 142 μm nickel MHE on silicon substrate was 3.04 $\frac{mg}{sec}$. On the other hand, mass transfer via the 90 μm nickel MHE on copper substrate was 3.20 $\frac{mg}{sec}$. This value was 5.26 % higher than the result for the silicon substrate, even with the silicon-based taller capillary channels. This shows that, even with a lower capillary height, the nickel based MHE on copper was able to outperform those on silicon substrate. This result agrees with previous model results

that predicted better performance based on the higher thermal conductivity of copper [75].

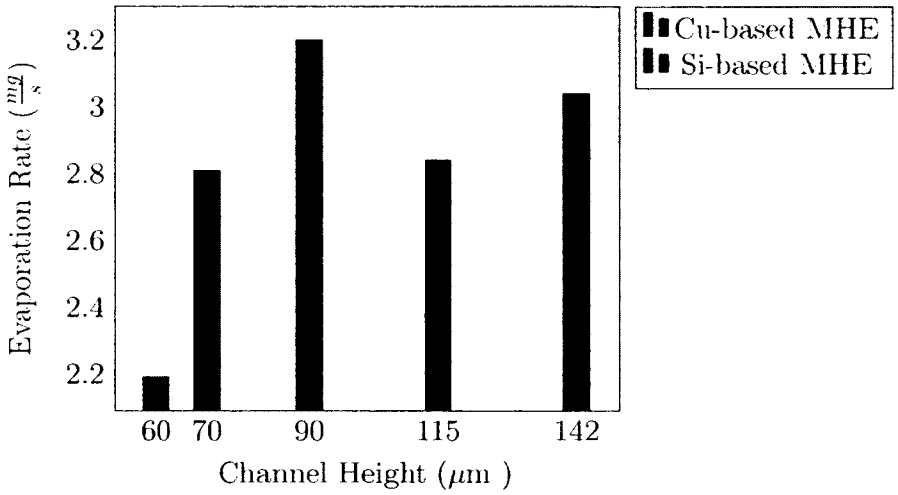

Figure 6.7: Evaporation Rates for Ni Heat Exchangers on Si and Cu Substrates

Table 6.3: Heat Exchanger Performance for 2.57 W Input

Substrate	**Height μm**	$\frac{mg}{sec}$	$\frac{kW}{m^2}$
Silicon	115	2.84	2.15
Silicon	142	3.02	2.31
Copper	60	2.19	1.66
Copper	70	2.81	2.13
Copper	90	3.20	2.42

Similarly, the power needed to drive phase change in the working fluid was recorded. This represented energy transfer from the resistance heater to the working fluid per unit time. In real world applications, this is equivalent to the amount of "waste" energy recaptured by the working fluid. This harvested energy may be utilized for other power applications. These results showed a general increasing trend as the channel height increased for the various device materials. As expected, the Cu-based

device showed the highest power absorption density of 2.42 $\frac{kW}{m^2}$ for the 90 μm height channel versus 2.31 $\frac{kW}{m^2}$ for the 142 μm height Si-based device. Again,these results agree with modeling and prior experimental results [75, 109].

Increased channel height represents more surface area for capillary force, hence increased capillary action. This resulted in increased mass transfer and power consumption. The effect of increasing open channel height on increasing capillary response has been established in both modeling exercises by Kim et al [85], as well as prior work evidenced in literature and by our group directly [75, 34].

It is worth noting the overall power consumption of the MHE versus known heat rejection values from various sources. In the field of thermal scavenging, for example, solar thermal energy has a power density of approximately 700 $\frac{W}{m^2}$ [97]. This is well within the capability of the characterized MHE. Other sources, like computer chips, have exhibited high thermal rejection rates on the order of 100 $\frac{W}{cm^2}$ [110]. The MHE may be well tailored to these sources through alternative working fluid selections that alter the boiling point and make it specifically well suited to high temperature operation.

Another significant finding uncovered was the direct material and working fluid interaction. The interaction of the HFE 7200 working fluid on electroplated nickel was studied both via droplet contact angle tests as well as direct capillary force observation. Previous research has indicated HFE 7200 has a contact angle of about 6 degrees with SU-8 surfaces [75]. This compared favorably to work in literature where water was studied in interaction with modified silicon and SU-8 surfaces, yielding contact angles on the order of 5 degrees [111, 112]. By contrast, in the present investigations, the

contact angle of the HFE 7200 working fluid with electroplated nickel surface showed no droplet formation on the surface itself. Instead, the electroplated nickel proved to be a porous material which readily absorbed the working fluid as it was applied. In this manner, the nickel represented a wettable surface, however, not in the traditional sense. Figure 6.8 shows the results of droplet deposition atop the surface.

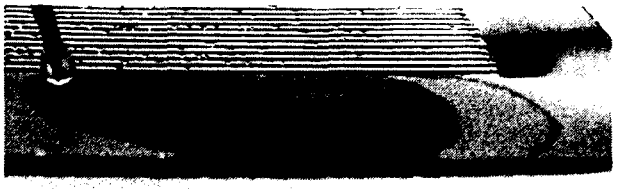

Figure 6.8: HFE 7200 Droplet on Electroplated Nickel

There is a possibility that higher temperature testing can further enhance the operation of the devices with porous nickel. In these devices, it has been shown that HFE 7200 is directly absorbed within the material itself. This porous structure represents increased overall surface area and direct contact area for the working fluid. As temperature increases, working fluid within the nickel structure itself will begin to phase change and boil at increasing rate. This should have the beneficial effect of increasing the overall mass transfer and heat exchanger area from simply within the capillary channels to across the entire structure itself

Direct capillary action was investigated for the 115 μm and 90 μm nickel MHE. The capillary channels were allowed to draw working fluid vertically from a bath as previously described and noted in Figure 6.6. The 115 μm capillaries were able to draw working fluid 4.51 mm above the fluid bath line, and the 90 μm capillaries were shown to draw fluid vertically 3.76 mm. This confirms the importance of capillary action in

wicking the working fluid, and also highlights the increased thermal conductivity as the reason for increased mass transfer and power consumption when thermal energy was applied.

6.4 Conclusions

The fabrication of low cost, metal-based micro-capillary channels for thermal scavenging and heat transfer application has been reported. Electrodeposition technique was utilized to form channel walls using photoresist film as the mold. The photoresist film (Ordyl P-50100) was laminated over the substrate and exposed with a UV lamp. Development of the exposed resist in a mildly alkaline solution produced the mold ready for electrodepostion. This technique did not require a flat substrate surface for successful microfabrication process. Traditional microfabrication technique has been limited to substrates with very flat surfaces, specific dimension and geometry. The technique presented in this work has been successfully utilized to fabricate microchannels on both silicon and copper substrates. The nickel microchannels electroplated on the substrate were applied as heat exchangers in this work for thermal scavenging applications.

Exchanger operation was based on capillary channels ability to wick HFE 7200 working fluid across a heated surface to drive mass transfer and thermal energy consumption from a heat source. Operation of the heat exchangers showed an overall power consumption of 1.66 $\frac{kW}{m^2}$, 2.13 $\frac{kW}{m^2}$ and 2.42 $\frac{kW}{m^2}$ for the 60 μm, 70 μm and 90 μm high nickel MHEs respectively on copper substrate. Also for the MHEs on silicon substrate, the overall heat energy consumption were 2.15 $\frac{kW}{m^2}$ and 2.31 $\frac{kW}{m^2}$ for the 115

μm and 142 μm high nickel MHEs respectively. These values represent the power harvested by the exchangers in addition to the cooling effect provided. Overall working fluid mass transfer rate was shown to be 2.19 $\frac{mg}{s}$, 2.81 $\frac{mg}{s}$, 3.20 $\frac{mg}{s}$, 2.84 $\frac{mg}{s}$ and 3.04 $\frac{mg}{s}$ for the 60 μm, 70 μm, 90 μm, 115 μm and 142 μm MHEs respectively.

Direct investigation of HFE 7200 working fluid with the capillary channels wall material was also reported. The electroplated nickel represented a porous structure, capable of absorbing working fluid. There may be advantages to the porous nature of the nickel material itself as it represents an increased overall surface area for mass transfer, and thus, heat exchange.

The microfabrication technique presented in this work is suitable for a wide range of substrates, at effective cost point. Future work will investigate the performance of higher aspect ratio channel devices as well as other metal substrates and channel walls. These unique MHEs have the potential to enhance the overall system performance of microelectronics through cooling effect provided, as well as the energy scavenging potential.

CHAPTER 7

CONCLUSIONS

The science of miniaturization has led to the production of many micro devices. Sustainable autonomous power supply for these devices, especially in remote locations, has been a challenge. The work presented in this study focused on the integration of microfabrication processes and solar thermal technology to generate power for micro-scale applications. Solar energy is a clean and sustainable energy source that has a potential for present and future world energy needs. Solar thermal systems convert the sun's energy into heat. The heat is thereafter utilized by a heat engine for useful power output. Specifically, the use of a thermoelectric generator as a heat engine for solar thermal harvesting application has been examined. Further, a thermal scavenging technique that relies on phase change within the working fluid in a micro capillary channel boiler plate has also been examined.

Irrespective of the heat engine applied, one critical parameter in the operation of these devices is the temperature gradient resulting between the heat source and sink. Higher temperature gradients typically lead to increased efficiency. Hence, a thermal analysis for a flat plate collector has been presented. It is shown that improving heat absorption on the absorber plate by maximizing absorption while reducing emittance, as well as improving the heat transfer efficiency between the absorber element and the

working fluid or heat engine will improve the overall collector efficiency. Also, limiting heat losses from the collector to the ambient enhances the overall system efficiency.

Initial fabrication and characterization steps performed in this study showed the potential and capability of a thin film Ni-Sn selective absorber coating for small-scale solar thermal energy harvesting. Thermal and heat flux absorption testing indicated that the coating significantly improved the ability of the collector to transform incident solar radiation into thermal energy. The integration of this small scale solar thermal collector with a TEG for useful power generation has also been demonstrated. The device utilized with selective absorber achieved 28.44 % of theoretical maximum.

The use of vacuum environment to limit the thermal losses from a solar collector plate has also been investigated. Tests were conducted to verify the operation temperature of collector plates when exposed to simulated solar radiation. Results showed an improvement in the stagnation temperature of the flat collector plate when operated in a partial vacuum environment (715 mTorr) compared to results obtained under atmospheric pressure (760 Torr). The temperature of the plate increased from 96 °C to 115 °C (an increase of 19 °C) by lowering the pressure of operation environment.

Thermal energy was also utilized to drive phase change in working fluid within micro heat exchangers. Exchanger operation was based on capillary channels ability to wick working fluid across a heated surface to drive mass transfer and thermal energy consumption from the heat source. Both Si-based and metal-based exchangers were examined. These devices utilizing the heat from the sun as input have the potential to provide autonomous power for micro electronics, and represent sustainable alternatives to battery-powered MEMS-based devices.

7.1 Recommendations for Future Work

Initial investigations into solar thermal harvesting for micro scale applications have been presented in this dissertation. This study is by no means exhaustive. Hence, to further develop the technology and processes presented in this work, the following recommendations for future work are suggested:

- Investigation of bonding techniques that will allow for the direct integration of collector plates and the heat engines.
- The design and fabrication of collector and heat engine on a single substrate should also be investigated. This way, the selective coating may be applied on one side of the substrate while a heat sink/exchanger may be constructed on the other side of the substrate using microfabrication processes.
- Further work to examine the temperature of the plate under higher vacuum conditions.
- The effect of other operation environments with low thermal conductivity gases like argon, xenon and krypton should also be investigated. This way, rather than maintaining a vacuum environment, other gases (with thermal conductivity lower than air) may be utilized to replace air molecules within the operation environment. It is anticipated that this would also limit thermal losses from the collector plate.
- Integration of the micro heat exchangers studied with other devices such as micro turbines and free piston expanders for useful work output.
- Investigation of the performance of higher aspect ratio channel devices as well as other substrates materials and channel walls for the micro heat exchangers.

APPENDIX A

VACUUM CHAMBER DRAWINGS

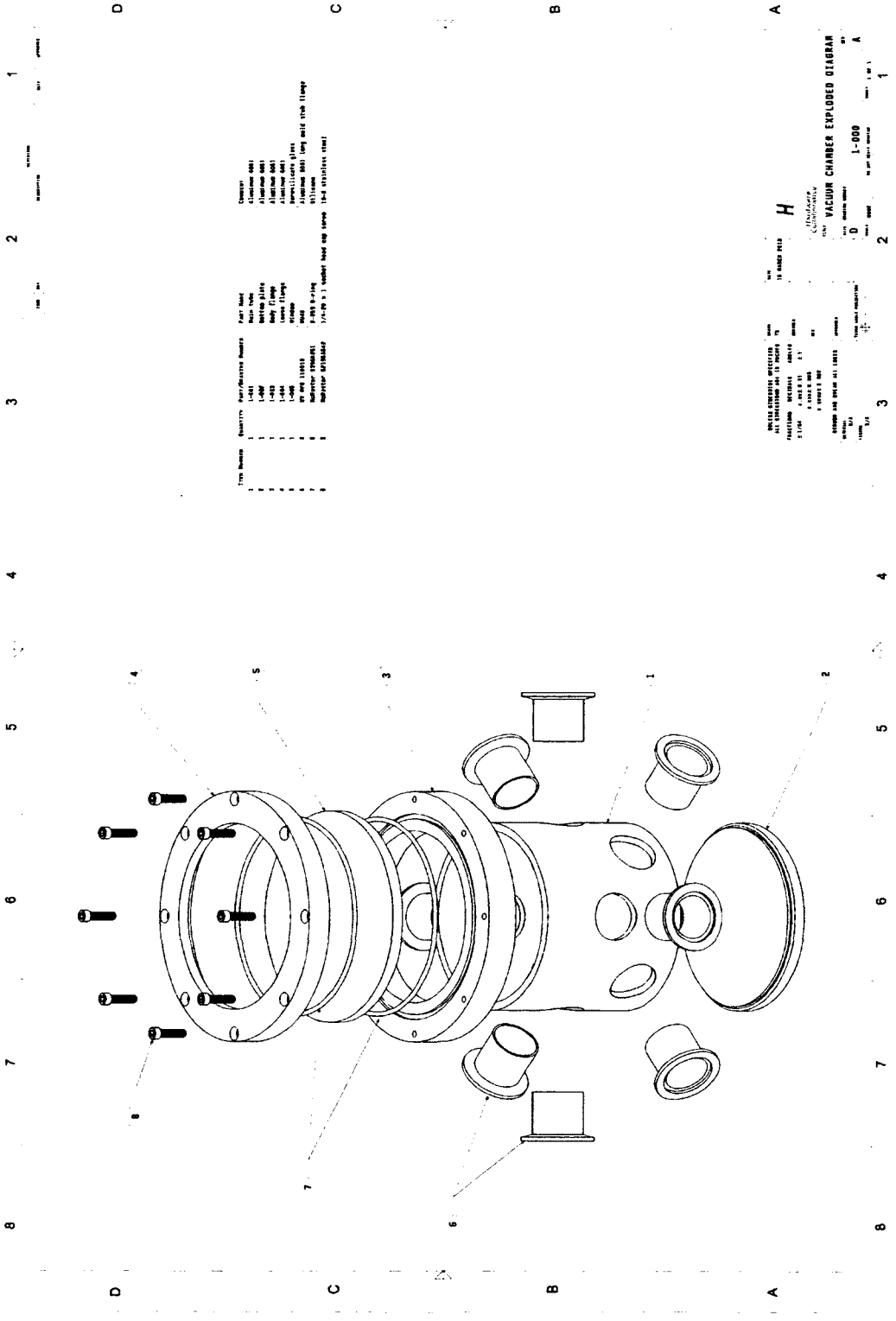
VACUUM CHAMBER EXPLODED DIAGRAM
1-000

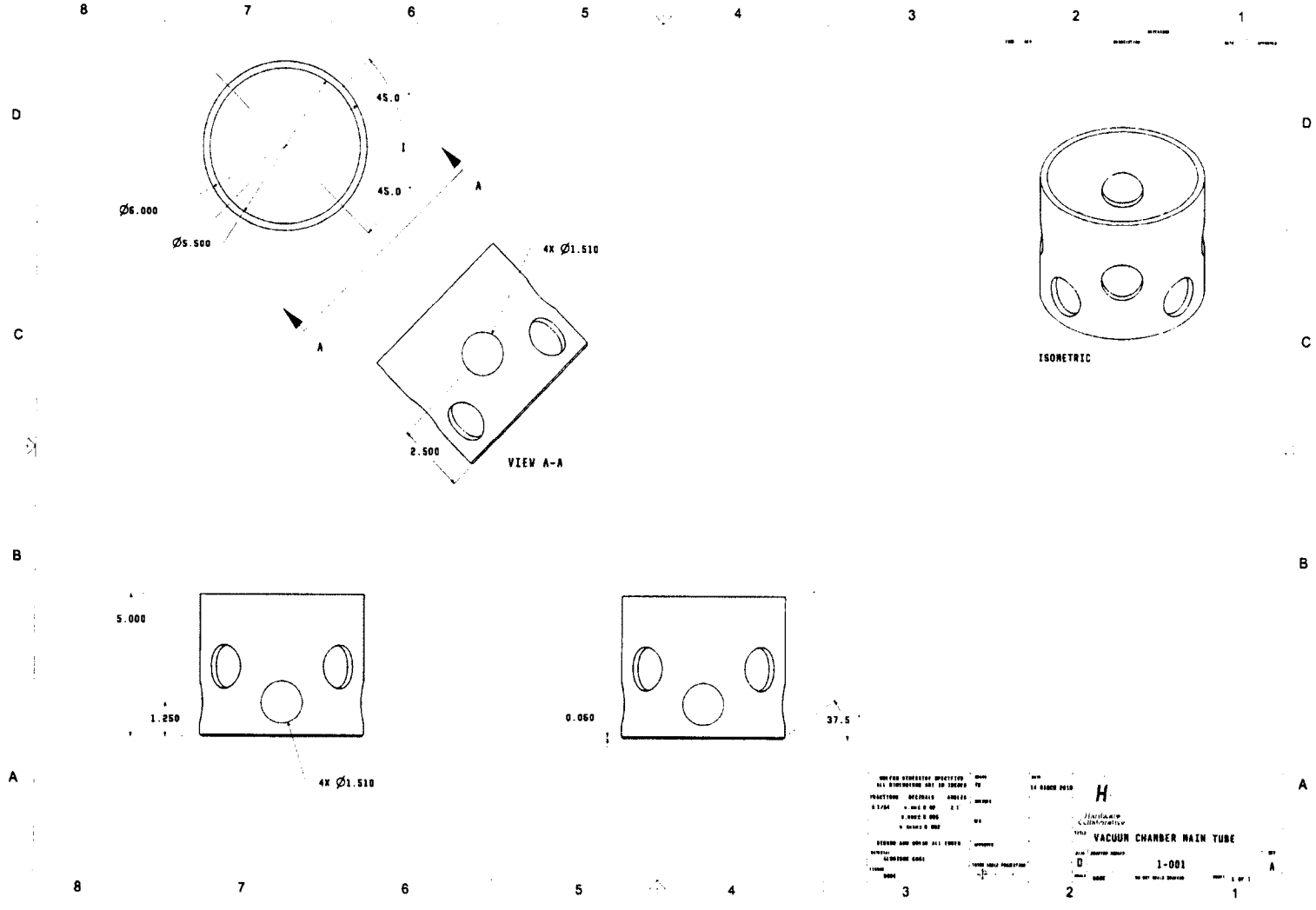
45.0
45.0
Ø6.000
Ø5.500
A
A
4X Ø1.510
2.500
VIEW A-A
ISOMETRIC
5.000
1.250
4X Ø1.510
0.060
37.5
VACUUM CHAMBER MAIN TUBE
1-001

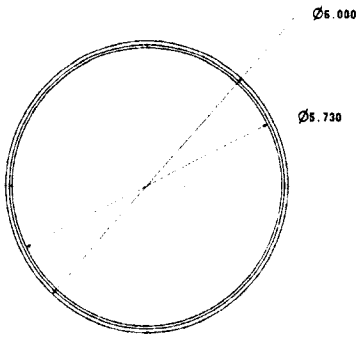

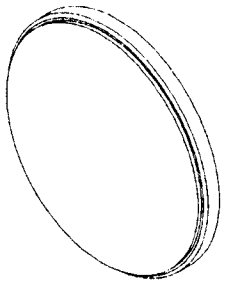

ISOMETRIC

VACUUM CHAMBER BOTTON PLATE

D 1-002 A

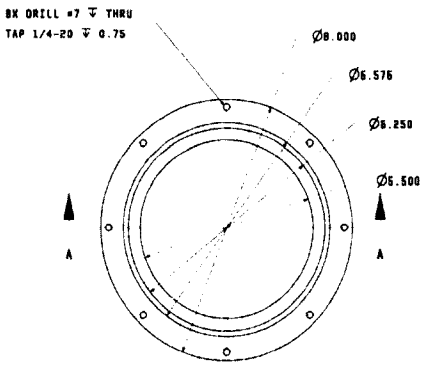
BK DRILL #7 ↧ THRU
TAP 1/4-20 ↧ 0.75
Ø8.000
Ø6.575
Ø6.250
Ø5.500
A
A

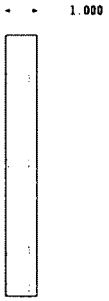
1.000

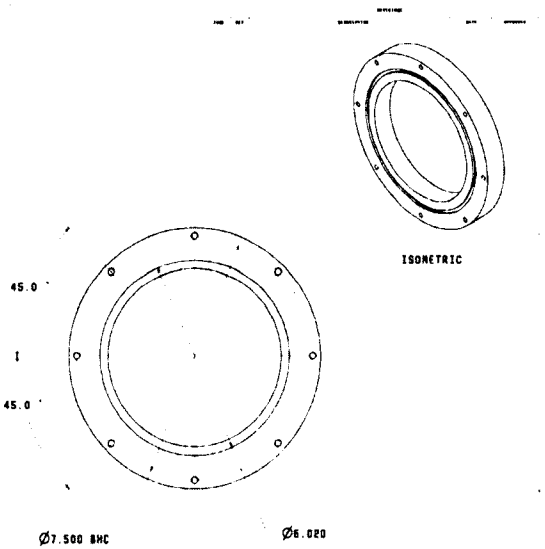
ISOMETRIC
45.0
45.0
Ø7.500 BHC
Ø6.020

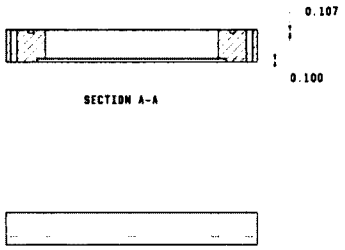
0.107
0.100
SECTION A-A

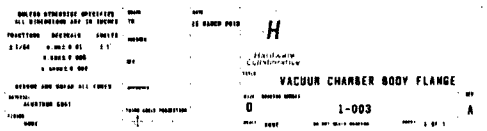
H
VACUUM CHAMBER BODY FLANGE
0
1-003
A

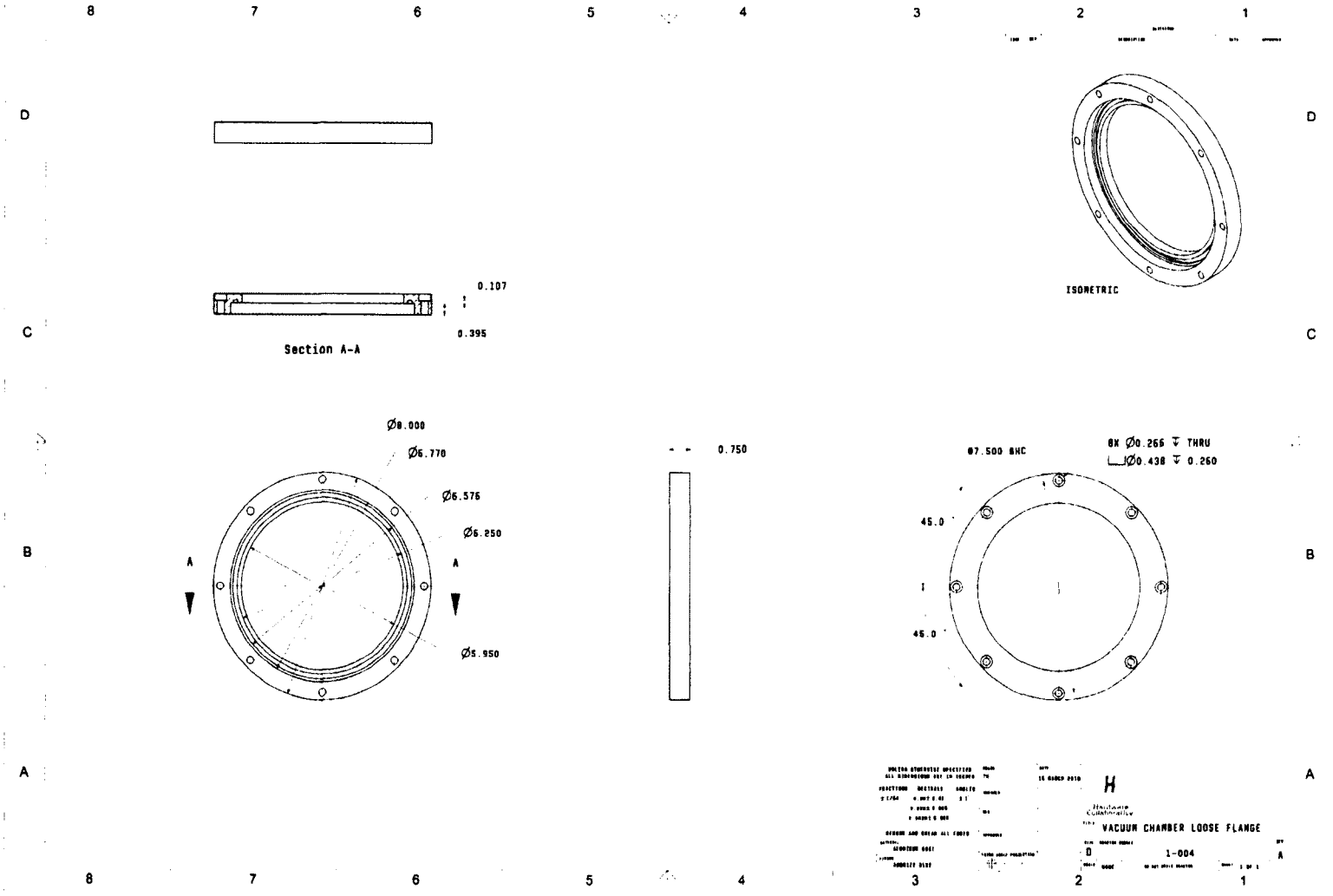
8
7
6
5
4
3
2
1
D
C
B
A
0.107
0.395
Section A-A
ISOMETRIC
Ø8.000
Ø6.770
Ø6.576
Ø6.250
Ø5.950
A
A
0.750
Ø7.500 BHC
8X Ø0.266 ↧ THRU
⌴Ø0.438 ↧ 0.260
45.0
45.0
H
VACUUM CHAMBER LOOSE FLANGE
D
1-004
A

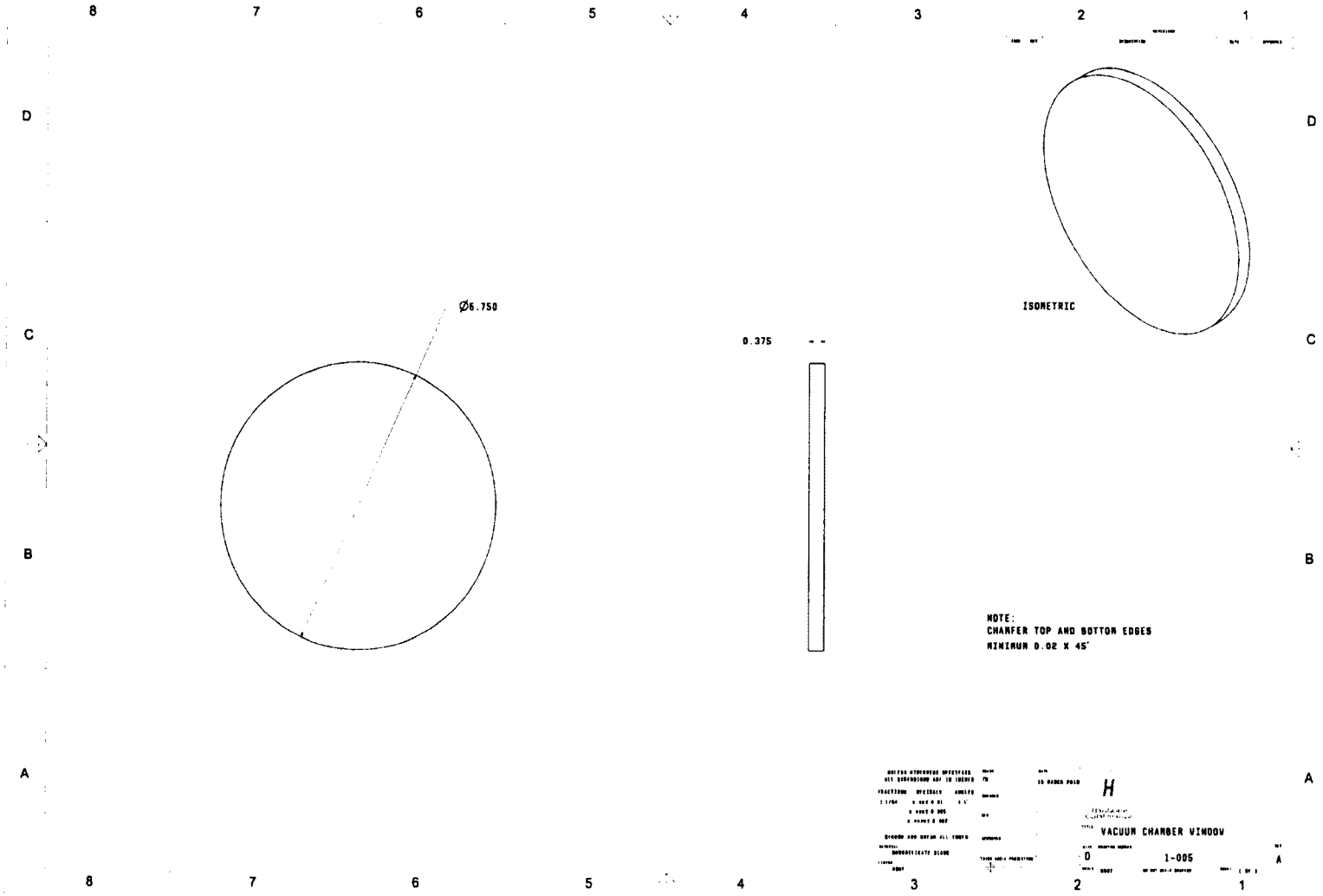
8
7
6
5
4
3
2
1
D
C
B
A
Ø6.750
0.375
ISOMETRIC
NOTE:
CHAMFER TOP AND BOTTOM EDGES
MINIMUM 0.02 X 45°
VACUUM CHAMBER WINDOW
1-005

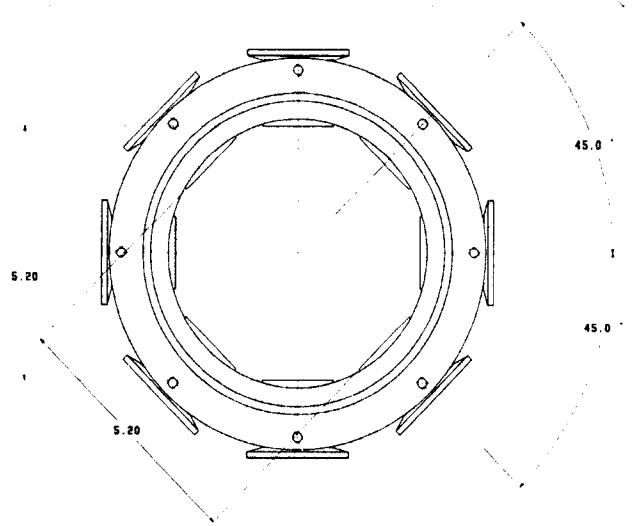

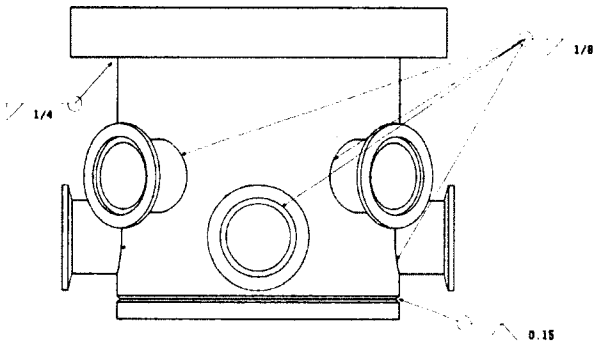

NOTES:
1. PART MUST BE GROUNDED BEFORE WELDING TO PREVENT ARCING AT ANY SEALING SURFACE

2. ALL WELDS MUST BE VACUUM QUALITY

VACUUM CHAMBER WELD DETAILS

D 1-006 A

APPENDIX B

LETTER OF COPYRIGHT PERMISSION

SPRINGER LICENSE
TERMS AND CONDITIONS

Jul 30, 2013

This is a License Agreement between Emmanuel Ogbonnaya ("You") and Springer ("Springer") provided by Copyright Clearance Center ("CCC"). The license consists of your order details, the terms and conditions provided by Springer, and the payment terms and conditions.

All payments must be made in full to CCC. For payment instructions, please see information listed at the bottom of this form.

License Number	3195580268472
License date	Jul 24, 2013
Licensed content publisher	Springer
Licensed content publication	Microsystem Technologies
Licensed content title	Micro solar energy harvesting using thin film selective absorber coating and thermoelectric generators
Licensed content author	Emmanuel Ogbonnaya
Licensed content date	Jan 1, 2012
Volume number	19
Issue number	7
Type of Use	Thesis/Dissertation
Portion	Full text
Number of copies	1
Author of this Springer article	Yes and you are the sole author of the new work
Order reference number	None
Title of your thesis / dissertation	Micro Solar Thermal Energy Development and Use for MEMS Power Applications
Expected completion date	Aug 2013
Estimated size(pages)	126
Total	**0.00 USD**
Terms and Conditions	

BIBLIOGRAPHY

[1] Kalogirou, S. A., 2004. "Solar thermal collectors and applications". *Progress in energy and combustion science*, **30**(3), pp. 231–295.

[2] Jha, A., 2009. *Solar cell technology and applications.* Auerbach Publications, Boca Raton, FL.

[3] Hamakawa, Y., 2002. "Solar pv energy conversion and the 21st century's civilization". *Solar energy materials and solar cells*, **74**(1), pp. 13–23.

[4] Barbose, G., Darghouth, N., and Wiser, R., 2012. Tracking the Sun IV: An Historical Summary of the Installed Cost of Photovoltaics in the United States from 1998 to 2010. Lawrence Berkeley National Laboratory. LBNL Paper LBNL-5047E. Retrieved from:http://escholarship.org/uc/item/3dp2p9xc Accessed: March 07, 2013.

[5] Solar PV Business News, 2013. Small chinese solar manufacturers decimated in 2012, January. http://www.enfsolar.com/news/Small-Chinese-Solar-Manufacturers-Decimated-in-2012 Accessed March 07, 2013.

[6] EPIA, 2012. Annual report 2011. Tech. rep., European Photovoltaic Industry Association, March. http://www.epia.org/uploads/tx_epiapublications/Annual_Report_2011.pdf Accessed March 8, 2013.

[7] Green, M. A., Emery, K., Hishikawa, Y., Warta, W., and Dunlop, E. D., 2012. "Solar cell efficiency tables (version 39)". *Progress in Photovoltaics: Research and Applications*, **20**(1), pp. 12–20.

[8] Duffie, J. A., and Beckman, W. A., 1991. *Solar Engineering of Thermal Processes*, 2 ed. Wiley Interscience, New York.

[9] Vullers, R. J. M., Van Schaijk, R., Doms, I., Van Hoof, C., and Mertens, R., 2009. "Micropower energy harvesting". *Solid-State Electronics*, **53**(7), pp. 684–693.

[10] Saadon, S., and Sidek, O., 2011. "A review of vibration-based mems piezoelectric energy harvesters". *Energy Conversion and Management*, **52**(1), pp. 500–504.

[11] Jacobson, S., and Epstein, A., 2003. "An informal survey of power mems". In The international symposium on micro-mechanical engineering, Vol. 12, pp. 513–519.

[12] Cook-Chennault, K., Thambi, N., and Sastry, A., 2008. "Powering mems portable devicesa review of non-regenerative and regenerative power supply systems with special emphasis on piezoelectric energy harvesting systems". *Smart Materials and Structures*, **17**(4), p. 043001.

[13] Vullers, R., Schaijk, R., Visser, H., Penders, J., and Hoof, C., 2010. "Energy harvesting for autonomous wireless sensor networks". *Solid-State Circuits Magazine, IEEE*, **2**(2), pp. 29–38.

[14] Harb, A., 2011. "Energy harvesting: State-of-the-art". *Renewable Energy*, **36**(10), pp. 2641–2654.

[15] Najafi, K., Galchev, T., Aktakka, E., Peterson, R., and McCullagh, J., 2011. "Microsystems for energy harvesting". In Solid-State Sensors, Actuators and Microsystems Conference (TRANSDUCERS), 2011 16th International, IEEE, pp. 1845–1850.

[16] Moghe, R., Yang, Y., Lambert, F., and Divan, D., 2009. "A scoping study of electric and magnetic field energy harvesting for wireless sensor networks in power system applications". In Energy Conversion Congress and Exposition, 2009. ECCE 2009. IEEE, IEEE, pp. 3550–3557.

[17] Zimmerman, R., Morrison, G., and Rosengarten, G., 2010. "A microsolar collector for hydrogen production by methanol reforming". *Journal of Solar Energy Engineering,* **132**, pp. 011005–1–5.

[18] Kamarudin, S., Daud, W., Ho, S., and Hasran, U., 2007. "Overview on the challenges and developments of micro-direct methanol fuel cells (dmfc)". *Journal of Power Sources,* **163**(2), pp. 743–754.

[19] Sukhatme, S. P., and Nayak, J. K., 2009. *Solar Energy: Principles of Thermal Collection and Storage*, 3rd ed. McGraw-Hill Education (India).

[20] Bogatu, C., Voinea, M., Anca, D., Pelin, I. M., and Chitanu, G. C., 2009. "The electrochemical deposition of cu/cuox solar selective coating with controlled morphology". *Revue Roumaine de Chimie,* **54**(3), pp. 235–241.

[21] Kennedy, C. E., 2002. Review of mid-to high-temperature solar selective absorber materials. Technical Report NREL/TP-520-31267, National Renewable Energy Laboratory, Golden, CO, July.

[22] Mahian, O., Kianifar, A., Kalogirou, S., Pop, I., and Wongwises, S., 2013. "A review of the applications of nanofluids in solar energy". *International Journal of Heat and Mass Transfer*, **57**(2), pp. 582–594.

[23] Otanicar, T., Taylor, R., Phelan, P., and Prasher, R., 2009. "Impact of size and scattering mode on the optimal solar absorbing nanofluid". In Proceedings of the ASME 3rd International Conference on Energy Sustainability, Vol. 1, pp. 791–796.

[24] Phelan, P., Bhattacharya, P., and Prasher, R., 2005. "Nanofluids for heat transfer applications". *Annual Reviews of Heat Transfer*, **14**(14), pp. 255–275.

[25] Minardi, J. E., and Chuang, H. N., 1975. "Performance of a'black'liquid flat-plate solar collector". *Solar Energy*, **17**(3), pp. 179–183.

[26] Otanicar, T., Phelan, P., Prasher, R., Rosengarten, G., and Taylor, R., 2010. "Nanofluid-based direct absorption solar collector". *Journal of Renewable and Sustainable Energy*, **2**, p. 033102.

[27] Holman, J. P., 2010. *Heat Transfer*, 10th ed. McGraw-Hill, New York.

[28] Chow, T., 2010. "A review on photovoltaic/thermal hybrid solar technology". *Applied Energy*, **87**(2), pp. 365–379.

[29] Ogbonnaya, E., Gunasekaran, A., and Weiss, L., 2013. "Micro solar energy harvesting using thin film selective absorber coating and thermoelectric generators". *Microsystem Technologies*, **19**(7), pp. 995–1004.

[30] Kraemer, D., Poudel, B., Feng, H., Caylor, J., Yu, B., Yan, X., Ma, Y., Wang, X., Wang, D., Muto, A., et al., 2011. "High-performance flat-panel solar thermoelectric generators with high thermal concentration". *Nature materials*, **10**(7), pp. 532–538.

[31] Agbossou, A., Zhang, Q., Sebald, G., and Guyomar, D., 2010. "Solar micro-energy harvesting based on thermoelectric and latent heat effects. Part I: Theoretical analysis". *Sensors and Actuators A: Physical*, **163**(1), pp. 277–283.

[32] Huesgen, T., and Woias, P., 2010. "A novel self-starting MEMS-heat engine for thermal energy harvesting". In Proceedings of the 2010 IEEE 23rd Interantional Conference on Micro Electro Mechanical Systems (MEMS), pp. 1179–1182.

[33] Hassan, I., 2006. "Thermal-fluid MEMS devices: a decade of progress and challenges ahead". *Journal of heat transfer*, **128**, pp. 1221–1233.

[34] Weiss, L. W., Richards, C. D., and Richards, R. F., 2011. "Power output force generation by a MEMS phase change actuator". *Journal of Microelectromechanical Systems*, **20**(6), Dec., pp. 1287–1297.

[35] Weiss, L., 2011. "Power production from phase change in MEMS and micro devices, a review". *International Journal of Thermal Sciences*, **50**(5), May, pp. 639–647.

[36] Zimmerman, R., Morrison, G., Rosengarten, G., et al., 2007. "A micro solar heater for portable energy generation". In Proceedings of SPIE, Vol. 6800.

[37] Kotipalli, V., Gong, Z., Pathak, P., Zhang, T., He, Y., Yadav, S., and Que, L., 2010. "Light and thermal energy cell based on carbon nanotube films". *Applied Physics Letters*, **97**(12), pp. 124102–124102.

[38] Jeong, J., Jiang, X., and Culler, D., 2008. "Design and analysis of micro-solar power systems for wireless sensor networks". In Proceedings of 5th International Conference on Networked Sensing Systems, pp. 181 –188.

[39] Taneja, J., Jeong, J., and Culler, D., 2008. "Design, modeling, and capacity planning for micro-solar power sensor networks". In Proceedings of the 7th international conference on Information processing in sensor networks, pp. 407–418.

[40] Gupta, V., Cruz-Campa, J., Okandan, M., and Nielson, G., 2010. "Microsystems-enabled photovoltaics, a path to the widespread harnessing of solar energy". *Future Photovolt*, **1**(1), pp. 28–36.

[41] Shao, H., Tsui, C., and Ki, W., 2009. "The design of a micro power management system for applications using photovoltaic cells with the maximum output power control". *IEEE Transactions on Very Large Scale Integration (VLSI) Systems*, **17**(8), Aug., pp. 1138–1142.

[42] Leonov, V., Fiorini, P., Sedky, S., Torfs, T., and Van Hoof, C., 2005. "Thermoelectric MEMS generators as a power supply for a body area network". In Proceedings of the 13th International Conference on Solid-State Sensor, Actuators and Microsystems, Vol. 1, pp. 291–294.

[43] Huesgen, T., Woias, P., and Kockmann, N., 2008. "Design and fabrication of MEMS thermoelectric generators with high temperature efficiency". *Sensors and Actuators A: Physical*, **145**, pp. 423–429.

[44] Strasser, M., Aigner, R., Lauterbach, C., Sturm, T. F., Franosch, M., and Wachutka, G., 2004. "Micromachined CMOS thermoelectric generators as on-chip power supply". *Sensors and Actuators A: Physical*, **114**(2-3), pp. 362–370.

[45] Norton, B., 2006. "Anatomy of a solar collector:: Developments in materials, components and efficiency improvements in solar thermal collector systems". *Refocus*, **7**(3), pp. 32–35.

[46] Kirilov, R., Stefchev, P., Alexieva, Z., and Dikov, H., 2010. "A high effective selective absorbing coating for solar thermal collectors". *Solid State Phenomena*, **159**, pp. 97–100.

[47] Shanmugam, N., Selvam, M., Srinivasan, K., John, S., and Shenoi, B., 1984. "Black nickel–tin selective coatings for solar thermal energy conversion". *Met. Finish.*, **82**(10), pp. 91–95.

[48] Sergeant, N., and Peumans, P., 2009. "High-performance absorbers for solar thermal applications". *SPIE Newsroom*, Nov. doi:10.1117/2.1200910.1835.

[49] Blum, W., 1949. *Principles of electroplating and electroforming:*, 3rd ed. McGraw-Hill.

[50] Murphy, M., ed., 1998. *METAL FINISHING: 66th Guidebook and Directory Issue, January 1998, Volume 95, Number 1.* Elsevier Science Inc.

[51] Muehlratzer, A., Goerler, G., Erben, E., and Zeilinger, H., 1981. "Selection of a black chrome bath for continuous tube-plating and the properties of the coatings deposited from it". *Solar Energy,* **27**(2), pp. 115–120.

[52] Alghoul, M., Sulaiman, M., Azmi, B., and Wahab, M., 2005. "Review of materials for solar thermal collectors". *Anti-Corrosion Methods and Materials,* **52**(4), pp. 199–206.

[53] Papadopoulos, A., 2005. "State of the art in thermal insulation materials and aims for future developments". *Energy and Buildings,* **37**(1), pp. 77–86.

[54] Jelle, B. P., Gustavsen, A., and Baetens, R., 2010. "The high performance thermal building insulation materials and solutions of tomorrow". In Proceedings of the Thermal Performance of the Exterior Envelopes of Whole Buildings XI International Conference (Buildings XI), Clearwater Beach, Florida, USA, pp. 5–9.

[55] Reim, M., Körner, W., Manara, J., Korder, S., Arduini-Schuster, M., Ebert, H.-P., and Fricke, J., 2005. "Silica aerogel granulate material for thermal insulation and daylighting". *Solar Energy,* **79**(2), pp. 131–139.

[56] Aerogels, Aspen, 2006. Spaceloft® 6250, Extreme protection for extreme environments. Data sheet. Retrieved from http://www.aerogel.com/products/pdf/Spaceloft_6250_DS.pdf Accessed June 4, 2013.

[57] Aerogels, Aspen, 2007. Spaceloft® 3251, 6251, 9251, Flexible insulation for industrial, commercial and residential applications. Data sheet. Retrieved from http://www.airtightdistribution.com/pdfs/Spaceloft_Data_Sheet.pdf Accessed June 4, 2013.

[58] Baetens, R., Jelle, B. P., Thue, J. V., Tenpierik, M. J., Grynning, S., Uvsløkk, S., and Gustavsen, A., 2010. "Vacuum insulation panels for building applications: A review and beyond". *Energy and Buildings*, **42**(2), pp. 147–172.

[59] Vestlund, J., Rönnelid, M., and Dalenbäck, J.-O., 2009. "Thermal performance of gas-filled flat plate solar collectors". *Solar Energy*, **83**(6), pp. 896–904.

[60] Lau, J. H., Lee, C. K., Premachandran, C., and Aibin, Y., 2010. *Advanced MEMS packaging*. McGraw-Hill.

[61] Chambers, A., Fitch, R., and Halliday, B., 1998. *Basic vacuum technology*. Taylor & Francis Group.

[62] Warner, C. Y., and Arpaci, V. S., 1968. "An experimental investigation of turbulent natural convection in air at low pressure along a vertical heated flat plate". *International Journal of Heat and Mass Transfer*, **11**(3), pp. 397–406.

[63] Churchill, S. W., and Chu, H. H., 1975. "Correlating equations for laminar and turbulent free convection from a vertical plate". *International Journal of Heat and Mass Transfer*, **18**(11), pp. 1323–1329.

[64] Chen, X., and Pfender, E., 1983. "Effect of the knudsen number on heat transfer to a particle immersed into a thermal plasma". *Plasma chemistry and plasma processing*, **3**(1), pp. 97–113.

[65] Kakac, S., Pramuanjaroenkij, A., and Liu, H., 2012. *Heat exchangers: selection, rating, and thermal design*. CRC press.

[66] Kaminski, D., 1980. *Fluid Flow Data Book*. General Electric Company.

[67] Howell, J. R., Bannerot, R. B., and Vliet, G. C., 1982. *Solar-thermal energy systems: analysis and design*. McGraw-Hill New York.

[68] Arana, L., Schaevitz, S., Franz, A., Schmidt, M., and Jensen, K., 2003. "A microfabricated suspended-tube chemical reactor for thermally efficient fuel processing". *Microelectromechanical Systems, Journal of*, **12**(5), pp. 600–612.

[69] Klein, S., 1975. "Calculation of flat-plate collector loss coefficients". *Solar Energy*, **17**, p. 79.

[70] Buchberg, H., Catton, I., and Edwards, D., 1976. "Natural convection in enclosed spaces: A review of application to solar energy collection". *J. Heat Transfer;(United States)*, **98**(2).

[71] Hollands, K., Unny, T., Raithby, G., and Konicek, L., 1976. "Free convective heat transfer across inclined air layers". *ASME J. Heat Transfer*, **98**(2), pp. 189–193.

[72] EIA, 2011. International energy outlook 2011. Technical Report DOE/EIA-0484(2011), U.S. Energy Information Administration, U.S. Department of Energy Washington, DC 20585. http://www.eia.gov/forecasts/archive/ieo11/pdf/0484(2011).pdf.

[73] EIA, 2012. Annual energy review 2011. Technical Report DOE/EIA-0384(2011), Energy Information Administration, Sept. http://www.eia.gov/totalenergy/data/annual/pdf/aer.pdf.

[74] Heywood, J., 1988. *Internal Combustion Engine Fundamentals*, first ed. McGraw-Hill, Inc, New York.

[75] Mathew, B., Jakub-Wood, B., Ogbonnaya, E., and Weiss, L., 2013. "Investigation of a mems-based capillary heat exchanger for thermal harvesting". *International Journal of Heat and Mass Transfer*, **58**(1), pp. 492–502.

[76] Weiss, L. W., 2010. "Study of a mems-based free piston expander for energy sustainability". *Journal of Mechanical Design,* **132**(9), pp. 091002–8.

[77] Crane, D. T., and Jackson, G. S., 2004. "Optimization of cross flow heat exchangers for thermoelectric waste heat recovery". *Energy Conversion and Management,* **45**(9-10), pp. 1565 – 1582.

[78] Saqr, K. M., Mansour, M. K., and Musa, M. N., 2008. "Thermal design of automobile exhaust based thermoelectric generators: Objectives and challenges". *International Journal of Automotive Technology,* **9**(2), April, pp. 155–160.

[79] Espinosa, N., Lazard, M., Aixala, L., and Scherrer, H., 2010. "Modeling a thermoelectric generator applied to diesel automotive heat recovery". *Journal of Electronic Materials,* **39**(9), Sept., pp. 1446–1455.

[80] Martínez, A., Vián, J., Astrain, D., Rodríguez, A., and Berrio, I., 2010. "Optimization of the heat exchangers of a thermoelectric generation system". *Journal of Electronic Materials,* **39**(9), Sept., pp. 1463–1468.

[81] Huang, I.-Y., Lin, J.-C., She, K.-D., Li, M.-C., Chen, J.-H., and Kuo, J.-S., 2008. "Development of low-cost micro-thermoelectric coolers utilizing mems technology". *Sensors and Actuators A: Physical,* **148**(1), pp. 176 – 185.

[82] Cheng, P., Wu, H.-Y., and Hong, F.-J., 2007. "Phase-change heat transfer in microsystems". *Journal of Heat Transfer,* **129**(2), pp. 101–108.

[83] Cheng, P., Wang, G., and Quan, X., 2009. "Recent work on boiling and condensation in microchannels". *Journal of Heat Transfer,* **131**(4), p. 043211.

[84] Tuckerman, D., and Pease, R., 1981. "High-performance heat sinking for vlsi". *Electron Device Letters, IEEE,* **2**(5), may, pp. 126 –129.

[85] Kim, D., Lee, K., Kwon, T., and Lee, S., 2002. "Micro-channel filling flow considering surface tension effect". *Journal of Micromechanics and Microengineering,* **12**, pp. 236–246.

[86] Wang, C.-T., Leu, T.-S., and Lai, T.-M., 2008. "Micro capillary pumped loop system for a cooling high power device". *Experimental Thermal and Fluid Science,* **32**(5), pp. 1090 – 1095.

[87] Cai, Q., Chen, C.-L., Xiong, G., and Ren, Z., 2008. "Explorations of carbon nanotube wick structure for high heat flux cooling". *ASME Conference Proceedings,* **2008**(48494), pp. 293–297.

[88] Launay, S., Sartre, V., and Bonjour, J., 2007. "Parametric analysis of loop heat pipe operation: a literature review". *International Journal of Thermal Sciences,* **46**(7), pp. 621–636.

[89] Rojas, M., and de Andres, M., 2006. "Theoretical and experimental study of two-phase flow in micro-channels grooved into horizontal pipes". *International Journal of Multiphase Flow,* **32**(4), pp. 517 – 526.

[90] Jung, J., Oh, H., Lee, D., Choi, K., Dong, S., and Kwak, H., 2008. "A capillary-pumped loop (cpl) with microcone-shaped capillary structure for cooling electronic devices". *Journal of Micromechanics and Microengineering,* **18**(1), January, pp. 1–7.

[91] Judy, J., 2001. "Microelectromechanical systems (mems): Fabrication, design, and applications". *Smart Materials and Structures,* **10**, pp. 1115–1134.

[92] Ogbonnaya, E., Jakub-Wood, B., Champagne, C., Chukwu, S., and Weiss, L., 2011. "Mems-based phase change for heat transfer with thermoelectric devices and energy harvesting". *Proceedings of the 2011 ASME IMECE, Denver CO*(IMECE2011-63562), November, pp. 1–7.

[93] MicroChem Corp. Microposit S1800 Series Photo Resist. Data sheet. Retrieved from http://www.microchem.com/PDFs_Dow/S1800.pdf. Accessed Jan 18. 2013.

[94] Lärmer, F., and Schilp, A., 1994. "Method of anisotropically etching silicon". *German Patent No DE4241045, United States Patent 5501893.*

[95] Tang, K., Liao, E., Ong, W., Wong, J., Agarwal, A., Nagarajan, R., and Yobas, L., 2006. "Evaluation of bonding between oxygen plasma treated polydimethyl siloxane and passivated silicon". In Journal of Physics: Conference Series, Vol. 34, IOP Publishing, pp. 155–161.

[96] Ahmad, M. J., and Tiwari, G., 2009. "Optimization of tilt angle for solar collector to receive maximum radiation". *Open Renewable Energy Journal,* **2**, pp. 19–24.

[97] Holman, J. P., 1997. *Heat Transfer*, 8^{th} ed. McGraw Hill, Inc.

[98] Lall, P., Pecht, M., and Hakim, E., 1997. *Influence of temperature on microelectronics and system reliability.* CRC.

[99] Mudawar, I., 2001. "Assessment of high-heat-flux thermal management schemes". *Components and Packaging Technologies, IEEE Transactions on,* **24**(2), jun, pp. 122 –141.

[100] Mathew, B., John, T., Ogbonnaya, E., Champagne, C., Weiss, L., and Hegab, H., 2011. "Solid state refrigerator for microchips". *Science of Advanced Materials,* **3**(4), pp. 672–681.

[101] Mei, F., Parida, P., Jiang, J., Meng, W., and Ekkad, S., 2008. "Fabrication, assembly, and testing of cu-and al-based microchannel heat exchangers". *Microelectromechanical Systems, Journal of,* **17**(4), pp. 869–881.

[102] Madou, M., 2002. *Fundamentals of microfabrication: the science of miniaturization.* CRC.

[103] Ashman, S., and Kandlikar, S., 2006. "A review of manufacturing processes for microchannel heat exchanger fabrication". In Proc. Fourth International Conference on Nanochannels, Microchannels and Minichannels, pp. 19–21.

[104] Ali, M. Y., 2009. "Fabrication of microfluidic channel using micro end milling and micro electrical discharge milling". *International Journal of Mechanical and Materials Engineering (IJMME),* **4**(1), pp. 93–97.

[105] Mei, F., Jiang, J., and Meng, W., 2007. "Eutectic bonding of al-based high aspect ratio microscale structures". *Microsystem technologies,* **13**(7), pp. 723–730.

[106] Kline, S., and McClintock, F., 1953. "Describing uncertainties in single-sample experiments". *Mechanical Engineering,* **75**(1), January, pp. 3–8.

[107] Gemignani, S., August 16, 2012. "re: Dry film samples". Email correspondence to the author.

[108] MicroChem Corp. Permanent epoxy negative photoresist processing guidelines for SU-8 2100 and SU-8 2150. Data sheet. Retrieved from http://www.microchem.com/pdf/SU-82000DataSheet2100and2150Ver5.pdf Accessed March 18, 2011.

[109] Ogbonnaya, E., and Weiss, L., 2012. "Fabrication and characterization of a metal-based micro-heat exchanger by electrodeposition technique". *Proceedings of the 2012 ASME IMECE, Houston TX*(IMECE2012-85900), November, pp. 1–8.

[110] Faghri, A., Zhang, Y., and Howell, J., 2010. *Advanced Heat and Mass Transfer*. Global Digital Press.

[111] Nordstrom, M., Marie, R., Calleja, M., and Boisen, A., 2004. "Rendering su-8 hydrophilic to facilitate use in micro channel fabrication". *Journal of Micromechanics and Microengineering*, **14**(12), p. 1614.

[112] Walther, F., Davydovskaya, P., Zürcher, S., Kaiser, M., Herberg, H., Gigler, A. M., and Stark, R. W., 2007. "Stability of the hydrophilic behavior of oxygen plasma activated su-8". *Journal of Micromechanics and Microengineering*, **17**(3), p. 524.